Time-Resolved Heat Flux Measurements of the Turbulent Junction Vortex System

by

Stacey Elaine Swisher

Thesis submitted to the Faculty of the

Virginia Polytechnic Institute and State University

in partial fulfillment of the requirements for the degree

Master of Science

in

Mechanical Engineering

APPROVED

T. E. Diller, Chairman

B. Vick

A. L. Wicks

May, 1991

Blacksburg, Virginia

Time-Resolved Heat Flux Measurements of the Turbulent Junction Vortex System

by

Stacey Elaine Swisher

T. E. Diller, Chairman

Mechanical Engineering

(ABSTRACT)

A rapid-response thin-film heat flux sensor was used to measure time-resolved unsteady heat flux in a complex junction vortex flow. This sensor, called the Heat Flux Microsensor, was used with a hot-wire anemometer to make simultaneous measurements of velocity and surface heat flux. The results were used to detect the relationship between the surface heat flux and the velocity unsteadiness. The study of this three-dimensional vortex system through time-resolved heat flux measurements is unique; as far as the author is aware, no previously published work has demonstrated the correlation between flow unsteadiness and its effects on the heat transfer for this phenomenon. The heat flux unsteadiness indicative of this vortex flow is discussed as turbulence coefficients and is calculated from both time-resolved and frequency measurements. Turbulence levels as high as 30% were recorded from the time-resolved data and were substantiated by the averaged power spectrum data. The development of the vortex system itself causes three times the heat transfer of the undisturbed boundary layer.

Acknowledgments

First and foremost, I would like to express my sincere gratitude to Dr. T. E. Diller. His guidance and insight during this process has truly been invaluable.

I would also like to thank my committee members, Dr. A. L. Wicks and Dr. B. Vick for their contributions toward the development of this work. Thanks, Dr. Wicks, for making signal processing a little more user-friendly.

The Heat Flux Microsensor was produced by the Vatell Corporation; thanks to Jon Hager and Jim Terrell for their interest and input on this research.

Thanks to my wise young roommate and good friend Val Gaddis for being a stable influence in stressful times and for giving me a broader view of the world.

If it had not been for the treasured friendship of Carol Wynn, I would not have had a life outside of Randolph Hall.

Thanks to Miguel Rivera for his eternal optimism and his willingness to listen.

Most importantly, thanks to my parents, Dr. George and Linda Swisher for their constant help, inspiration, and encouragement.

Table of Contents

List of Figures

List of Tables

Nomenclature

bl	boundary layer
c_p	specific heat at constant pressure $(J/(kg \cdot K))$
h	convection coefficient $(W/(m^2 \cdot K))$
L	characteristic length (m)
Nu	Nusselt number
Pr	Prandlt number
P1	position one, vortex center
P2	position two, separation point
P3	position three, attachment region
q"	heat flux (W/m^2)
Re	Reynold's number, $Re = V_\infty \cdot L/\nu$
RTS	Resistance Temperature Sensor
St	Stanton number, $St = h/(\rho \cdot V_\infty \cdot c_p) = Nu_L/(Re_L \cdot Pr)$
Tu	turbulence coefficient
v	voltage (volts)

V	velocity (m/s)
V_∞	mainstream velocity (m/s)

Greek Letters

ν	kinematic viscosity (m^2/s)
ρ	mass density (kg/m^3)

Subscripts

hf	heat flux
hw	hot-wire
x	local value
L	based on length

Superscripts

'	fluctuating quantity
-	overbar-average; time mean

Chapter One

Introduction

When a crossflow of air encounters the blunt nose of an airfoil shaped body, the mainstream boundary layer creates a complex three-dimensional flow occurring in the endwall region near the base of the body. This complex flow is a vortex system that causes very large variations in heat transfer and velocity in this region. Although conflicting opinions exist on the total number of vortices present in the system, there is overwhelming agreement that a dominant junction vortex, or the horseshoe vortex, does exist and is easily detected by flow visualizations.

The horseshoe vortex forms when the mainstream boundary layer produces a pressure gradient along the body stagnation region forcing the flow down toward the endwall. The flow then rolls up into a horseshoe vortex, and the boundary layer separates in front of the body. A schematic illustration of the horseshoe vortex system is given in Fig. 1. Because of the complexity and the unsteadiness of the flow in this region--including flow reversals-- analysis of the flow and heat transfer is difficult.

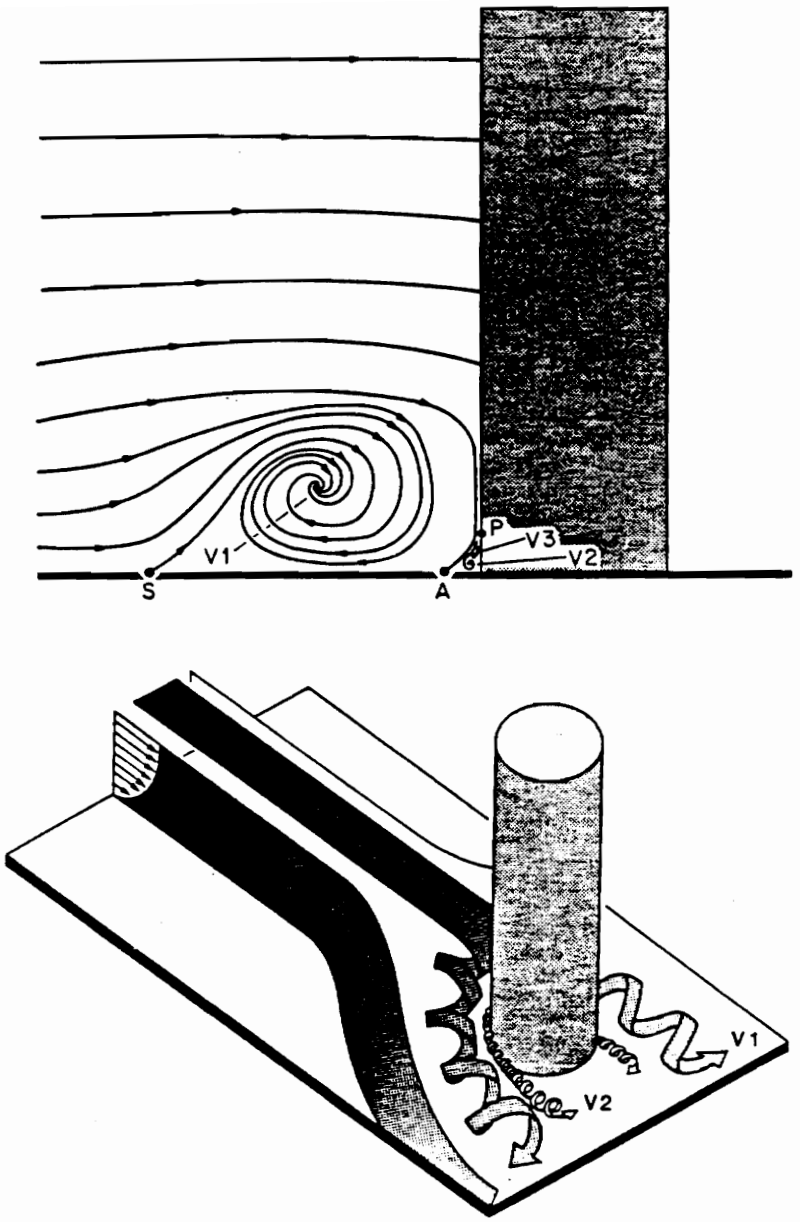

Fig. 1. The Horseshoe Vortex System [7]

This turbulent flow pattern is of particular interest in many engineering situations, such as turbomachinery blades and endwall flows, aircraft wing and other junction flows, and ship and submarine appendage flows. A fundamental understanding of this phemomenon will not only enable engineers to predict the heat transfer, but also enable them to control the phemomenon.

In an effort to accomplish this objective, the Heat Flux Microsensor is used to measure time-resolved local heat flux and characteristic frequencies at various positions in the turbulent vortex system. Simultaneous measurements of heat flux and velocity are recorded by the microsensor and a hot-wire anemometer, respectively. Their correlation is measured by the coherence function. The effects of turbulence are accounted for at specific frequencies and are discussed as turbulent coefficients. The purpose of this research is to demonstrate that the microsensor is a viable measurement technique for this flow situation because of its high frequency response, fast time response, and its non-disruptive nature. The Heat Flux Microsensor gives new information about the heat flux that exists in the vortex system, which should lead to an increased understanding of how the system's vortex structure affects the heat transfer.

Chapter Two

Literature Review

There are three major aspects of this review to consider: the horseshoe vortex system, heat flux measurement, and the Heat Flux Microsensor. In the first section, the behavior of the flow of the system and its heat transfer characteristics will be reviewed. Different techniques for heat flux measurement and their usefulness for unsteady flow will be mentioned in the second section. Finally, the third section will briefly discuss the fabrication, specifications, and advantages of the Heat Flux Microsensor.

2.1 The Turbulent Vortex System

As previously mentioned, little agreement exists on the details of the structure of the junction vortex system. According to Pierce and Tree [1], the flow system is composed of a large, well-defined vortex on the symmetry plane and a strong, but small

counter-rotating vortex located in the corner of the floor and the leading edge of the body. Their experiment used a two-channel laser Doppler velocimeter (LDV) system to acquire mean velocity measurements and real-time smoke visualizations to confirm the vortex structure. Abid and Schmitt [2] also recorded a similar model with laser data, although the work was not as detailed. Eckerle and Langston [3] reported five-hole probe measurements that showed the same two vortex model. Devenport and Simpson [4] used a laser anemometer and a hot-wire probe to further investigate the turbulence near the wing-body junction. Their results revealed data on the time-dependent and time-averaged turbulence structure of the flow. Hunt, Abell, Peterka, and Woo [5] applied topology to interpret surface flow visualization and proposed the four vortex model shown in Fig. 2. This was confirmed experimentally by Baker [6] from an oil-flow visualization. Using a naphthalene sublimation technique to determine variations of mass transfer, a three vortex model was suggested by Karni and Goldstein [7]. The flow visualization and structure results used in this research were the detailed data of Pierce and Tree [1]. The current experiment is comprised of the same wind tunnel and airfoil shaped body as was used to collect the detailed laser and surface data [1]. Fig. 3 shows the results of the smoke visualizations while Figs. 4 and 5 show LDV results.

Characteristic frequencies given off by the vortex system have rarely been examined. Devenport and Simpson [4] stated that the large turbulent stresses of the system were associated with bimodal (double-peaked) histograms of velocity fluctuations produced by a velocity variation that is bistable. They also hypothesized that the

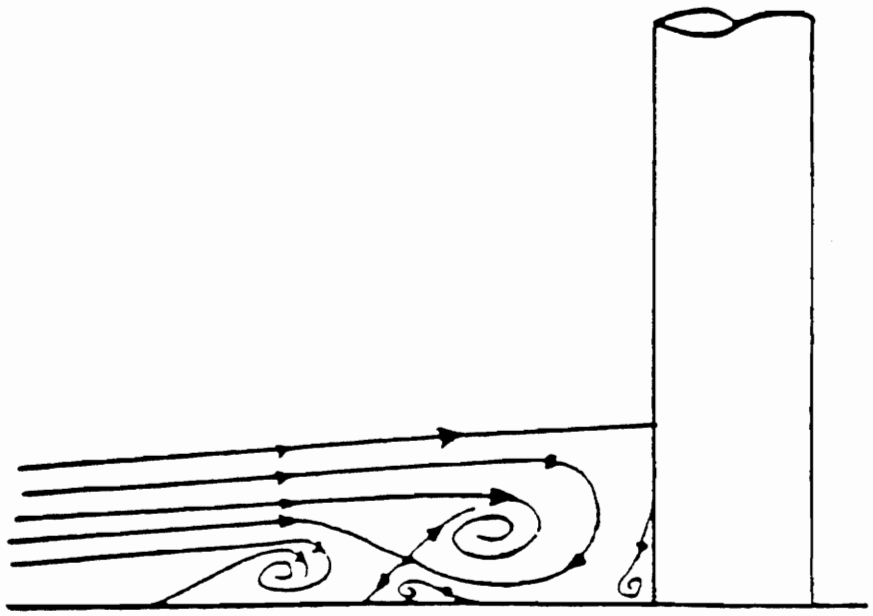

Fig. 2. Proposed Four Vortex Model [6]

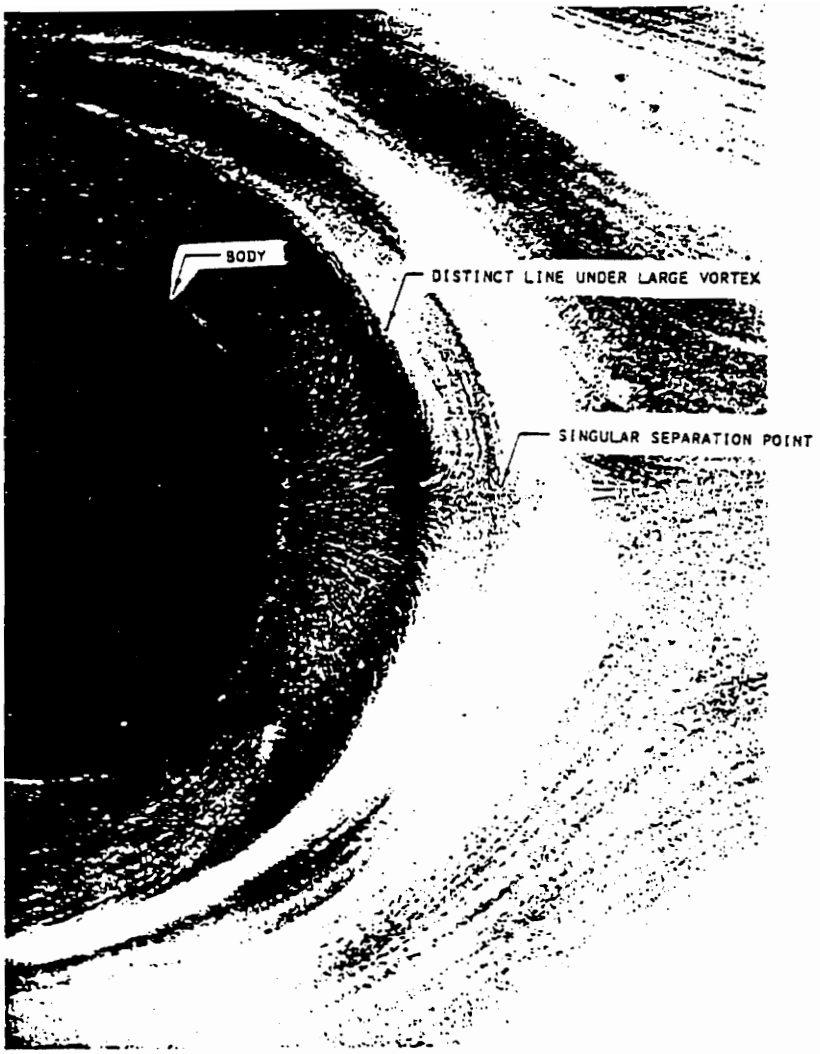

Fig. 3. Smoke Visualization of Vortex System [1]

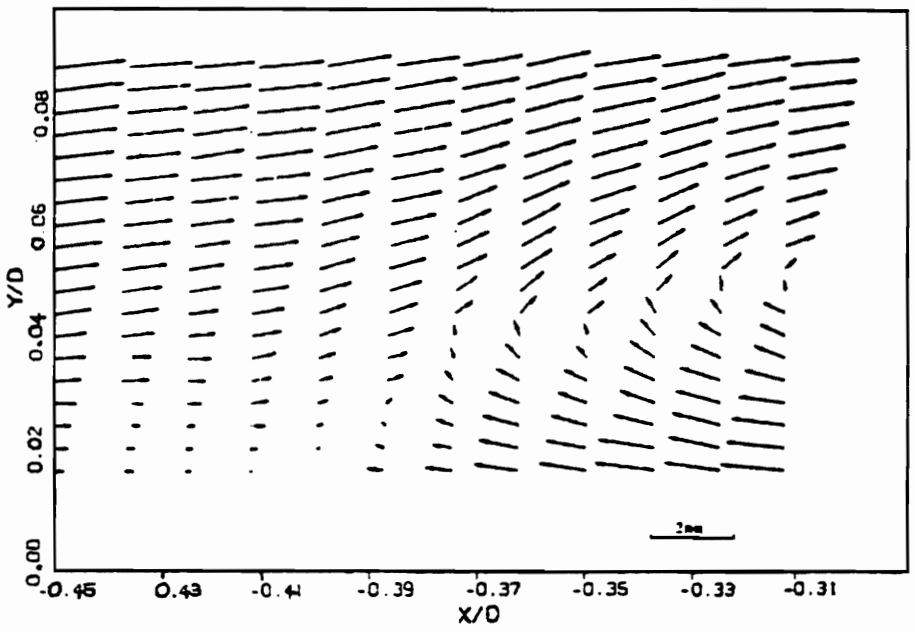

Fig. 4. LDV Velocity Field Near Separation Point [1]

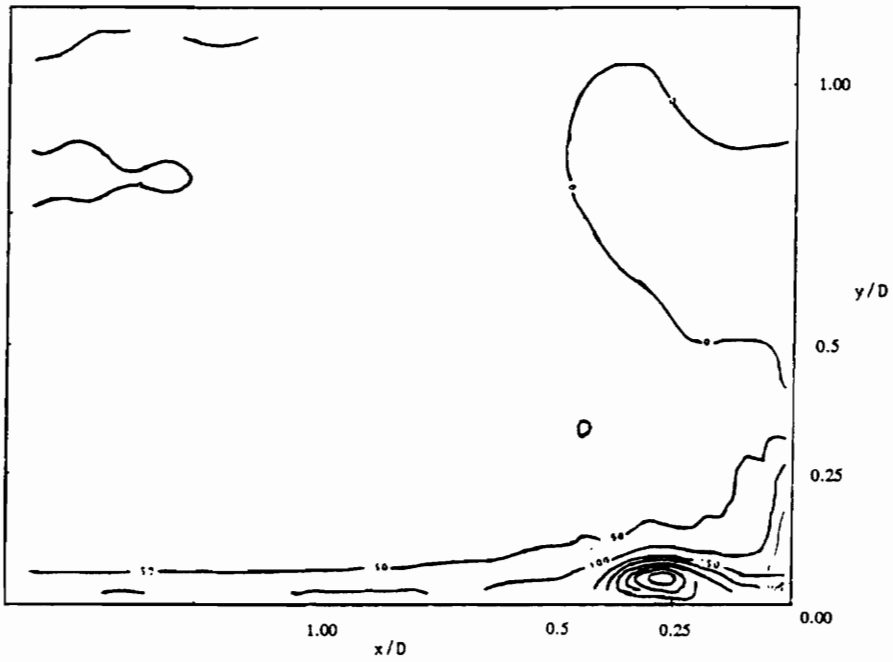

Fig. 5. Vorticity Field Computed From LDV Velocity Field [1]

unsteadiness is produced by fluctuations in the momentum and vorticity of fluid from the outer part of the boundary layer, recirculating as it impinged on the leading edge of the body. Frequencies of the large-scale unsteadiness were substantially lower than the passage frequency of the coherent structures in the boundary layer. Tree [8] presented time-averaged spectra taken with a laser anemometer in the region also showing a bimodal trend.

The heat transfer behavior of the vortex system was explored by examining other geometry-related situations. For example, Simmons, Hager, and Diller [9] used two rapid-response thin-film heat flux gages to measure time-resolved unsteady heat transfer signals at a stagnation point. The Heat Flux Microsensor was one of those gages and was used in this research as well to measure the stagnation point of the horseshoe flow. The results indicated a direct correlation between the turbulent velocity fluctuations and heat flux variation. An experimental study was made by Mori, Koizumi, and Nogo [10] to clarify the heat transfer performance near the separation point of a forward facing step. They concluded that, for turbulent boundary layers, the position of the separation point was very close to the step and fluctuated with amplitudes about twice as large as the height of the step. They also noted that the Reynold's analogy did not hold at the stagnation point, meaning that the heat fluxes at that point did not go to zero as the wall shear stress did.

Perhaps the most useful application of this research deals with gas-turbine technology. Improving efficiency of these turbines requires detailed local heat transfer

and velocity measurements. Graziani, Blair, Taylor, and Mayle [11] studied the endwall and blade surface heat transfer in a large scale cascade of blades and observed that the vortex system greatly influenced the heat transfer in the region of the blade's endwall surface. Measurements were made using uniform heat flux models consisting of heated blade and endwall assemblies. It was also noted that the size of the inlet boundary layer on the endwall has a significant effect on endwall heat transfer, yet the Stanton number does not change significantly with thin or thick boundary layers. This was explained as an indication of scouring of the endwall by the vortex.

A comparison of visualized turbine endwall flow patterns and measured Stanton number distributions was made by Gaugler and Russell [12]. Flows were traced by neutrally bouyant helium-filled soap bubbles, by smoke from oil soaked cigars, and by permanent marker pen ink dots and synthetic wintergreen oil. These three techniques were then compared to Stanton number contours reported by Hylton, Mihelc, Turner, and York [13]. From this investigation it was concluded that the only obvious correlation between the horseshoe vortex and the endwall heat transfer is near the leading edge of the blade, where a local peak in heat transfer occurs and the vortex starts to roll up.

Stanton number was again used as a nondimensionalized local heat transfer coefficient in the turbine passage studies of Hippensteele and Russell [14]. By using a liquid-crystal, heater-element composite sheet on the endwall surface, Stanton number was experimentally mapped on that surface over a range of Reynolds numbers. Figs. 6 and 7 show these heat transfer coefficient maps. For all inlet Reynolds numbers tested,

CONTOUR	STANTON NUMBER
A	0.00355
B	0.00398
C	0.00436
D	0.00508
E	0.00553
F	0.00609
G	0.00664
H	0.01070

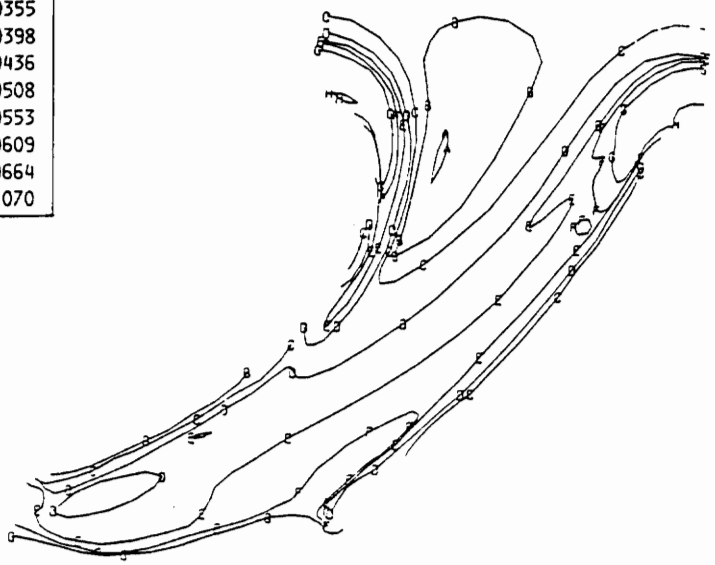

Fig. 6. Heat Transfer Coefficient Map, Re = 83,000 [14]

CONTOUR	STANTON NUMBER
A	0.00331
B	0.00350
C	0.00396
D	0.00437
E	0.00474
F	0.00578
G	0.00714

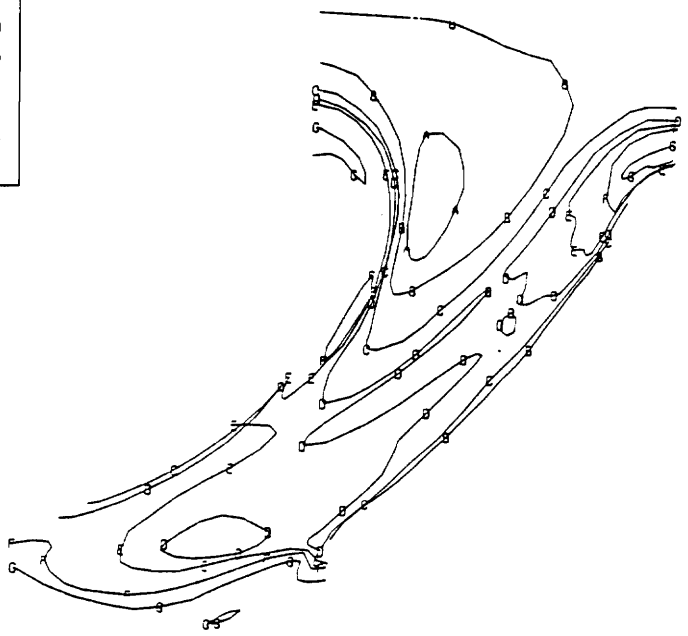

Fig. 7. Heat Transfer Coefficient Map, Re = 146,000 [14]

83,000 to 397,000, the maximum Stanton numbers occurred at the leading edge region. The horseshoe vortex could be seen at all Reynolds numbers. Lastly, their data did agree with Gaugler and Russell [12] that the separation line of the endwall did not correlate with the endwall heat transfer.

Goldstein and Spores [15] used the heat-mass transfer analogy to study the complex flow in the endwall region. This was accomplished by casting naphthalene onto a removable endwall plate in a turbine blade cascade. A detailed contour plot of the local convection coefficient is obtained by sublimation of the naphthalene. They concluded that the secondary flow between turbine blades can have a localized effect of up to five times the increased convection on the passage endwall. They also confirmed the existence of the corner vortex at the leading edge with this experiment.

Accurate knowledge of separating and recirculating flows is also valuable from the biomedical point of view. Thum and Diller [16] studied the mass transfer of oxygen in saline and blood on the downstream side of a backward-facing step with laminar flow inside a tube. This study was used as an experimental model for the separating and recirculating flows in the arterial system. Their results showed high heat transfer rates in this downstream region, especially at the point of reattachment.

To understand the basic phenomena of this convective heat transfer, one must know how the unsteady fluid flow affects the surface heat transfer. Although information in steady and time-average quantities are numerous, time-resolved measurements have only recently been used to capture the unsteady characteristics of the flow. Development

in the experimental domain has made possible the recording of high-speed response of the unsteady phenomena. A review of unsteady heat transfer measurement techniques developed in the past decade has been published by Diller and Telionis [17].

2.2 Heat Flux Measurement

Most heat flux gages for measuring heat transfer between a flowing fluid and a solid surface can be categorized into three groups: (1) the measurement of electric power dissipated in a heater at steady state, (2) the measurement of the temperature difference across a known thermal resistance in the surface, and (3) the measurement of the time rate of change of thermal energy at the surface [17]. Gages from each of the categories have been used to take limited unsteady measurements.

Monitoring the electric power necessary to maintain a heated surface temperature as a means of convective heat transfer measurements yields accurate results for large surface areas [18]. Unfortunately, this method falls short in terms of spatial resolution for smaller surface areas. The time constants needed to reach thermal equilibrium for these gages are typically minutes long; this time increment is much too slow to measure the effects of the unsteady flow. Even when these gages are made with thin-film resistance layers, they must be driven with a feedback control system [19]. Because the method is no longer passive, it can only measure heat flux from the surface; heat flux

to the surface cannot be measured. This method would be especially disappointing in the complex flow system currently under study.

The second and most popular category operates by measuring a temperature difference across a known thermal resistance. This is usually accomplished by forming a thermopile by placing thermocouples in series across the thermal resistance. The thickness of the sensor is dictated by the physical placement of the thermocouple junctions. Because of this thickness, a major problem for these gages is their physically and thermally disruptive nature when placed in the measured flow field. Fig. 8 shows a schematic diagram of a gage as an additional layer on the measured surface. T_1 is the surface temperature of the gage and T_3 is the surface temperature of the material being measured. If T_1 is used to calculate the heat transfer coefficient, h, instead of T_3, a sizeable error could occur. This difference in temperatures could also cause a change in the thermal boundary condition, causing the heat transfer in the surface material to be nonuniform.

Measurements of the third type involve using the thermal capacitance of the gage and/ or model material with surface temperature measurements to infer the heat transfer from the time-temperature histories [17]. This type of measurement is often used in transient flows. An analytical model is used to determine what heat transfer coefficient history is necessary to produce the observed temperature history. The resulting data analysis is very complicated.

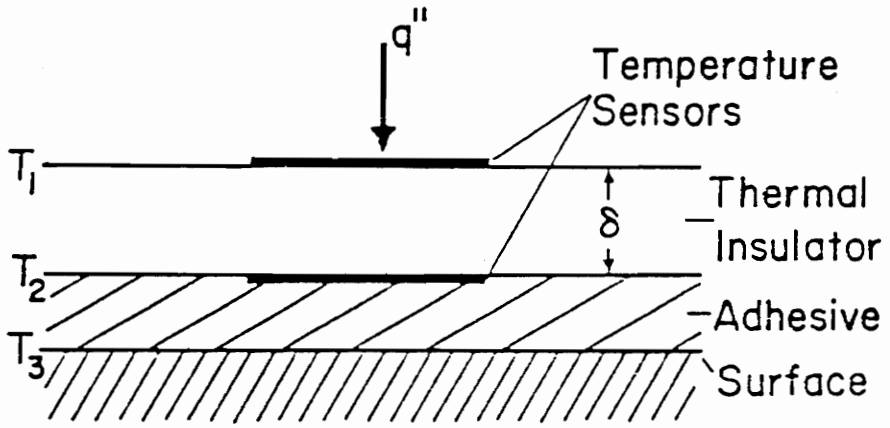

Fig. 8. Schematic Cross Section of a Layered Heat Flux Gage [17]

2.3 The Heat Flux Microsensor

The Heat Flux Microsensor belongs in the second group of heat flux measurement devices. Made using microfabrication techniques [20], the sensor is a thin-film gage with several thin-film layers forming a differential thermopile across a thermal resistance layer. The thermopile is formed by metal strips of nichrome and platinum overlapping above and below the silicon monoxide resistance layer to form series thermocouple junctions, as illustrated in Fig. 9. The output voltage from the thermocouples is directly proportional to the heat flux. This signal is much preferred to the complicated analysis needed for category three gages.

Since the gage is sputter coated directly onto the measurement surface, the total thickness is less than 2 μm. Unlike other gages that must include the thickness of the adhesive to the overall thickness of the sensor, the Heat Flux Microsensor requires no adhesive. Fig. 10 shows the schematic of the layered heat flux gage. Ridding the gage of this layer also improves the heat flux reading. Because the gage is so thin, it contributes negligible disturbance to the flow or the thermal boundary layer and has a high frequency response. When compared to Fig. 8, it is obviously a better design when flow disturbance is a problem. The gage only covers a surface area of 3 mm by 4 mm--small enough to measure local values of heat flux. The Heat Flux Microsensor is

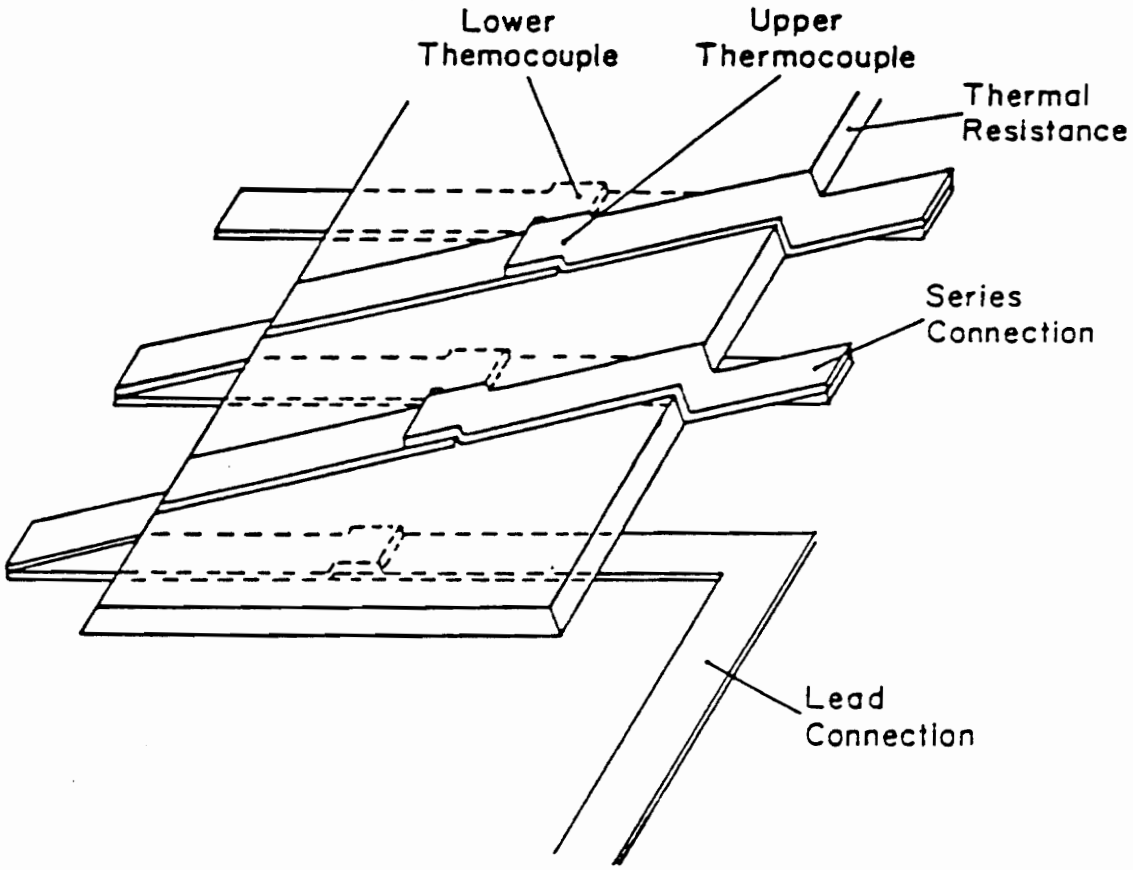

Fig. 9. Isometric View of Thermocouple Junctions

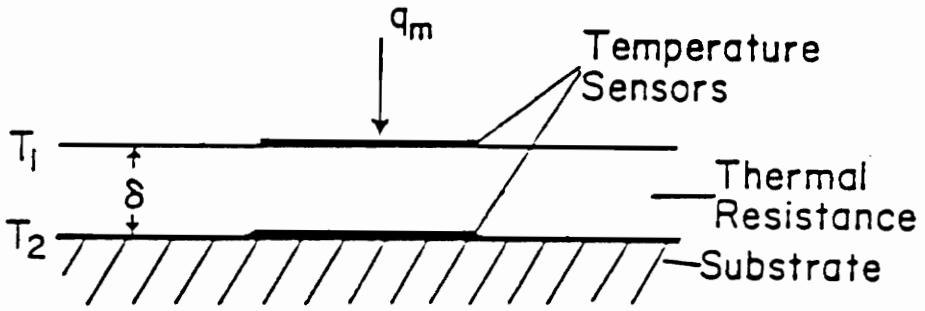

Fig. 10. Schematic Cross Section of the Heat Flux Gage

excellent for measuring complex unsteady flow characteristics: its response time is approximately 20 μsec [21] and its passive nature enables heat flux to be measured to and from a surface. Fig. 11 displays a top view of the Heat Flux Microsensor.

Many improvements have been made since the microsensor's inception. Feed-through leads are now used to bring the signal through the substrate to measurement instrumentation. This innovation is especially important to aerodynamic testing by preventing additional surface disruption. Secondly, a new temperature sensor called the resistance temperature sensor, or RTS, was developed to improve high-temperature measurement performance. Two high-temperature flame tests were used to determine the failure temperature of the RTS. Its calibration is discussed in Appendix C.

The Heat Flux Microsensor has proven to be valuable in a number of different situations. Its response to an instantaneous heat source is recorded in Fig. 12. The microsensor was also tested in an industrial drying simulation consisting of arrays of impinging jets and measured the transient cooling process of the system (see Appendix A). Mounted in the wall of a supersonic wind tunnel, the microsensor captured the effects of a shock passage on the heat transfer at the wall. Fig. 13 and Fig. 14 show typical results from these supersonic tests. The gage was additionally used to perform conduction tests on living tissue. The goal was to determine the effect of blood flow on the transient conduction heat transfer between the previously cooled probe containing the microsensor and the tissue [22].

In light of the research being presented, perhaps the most informative test

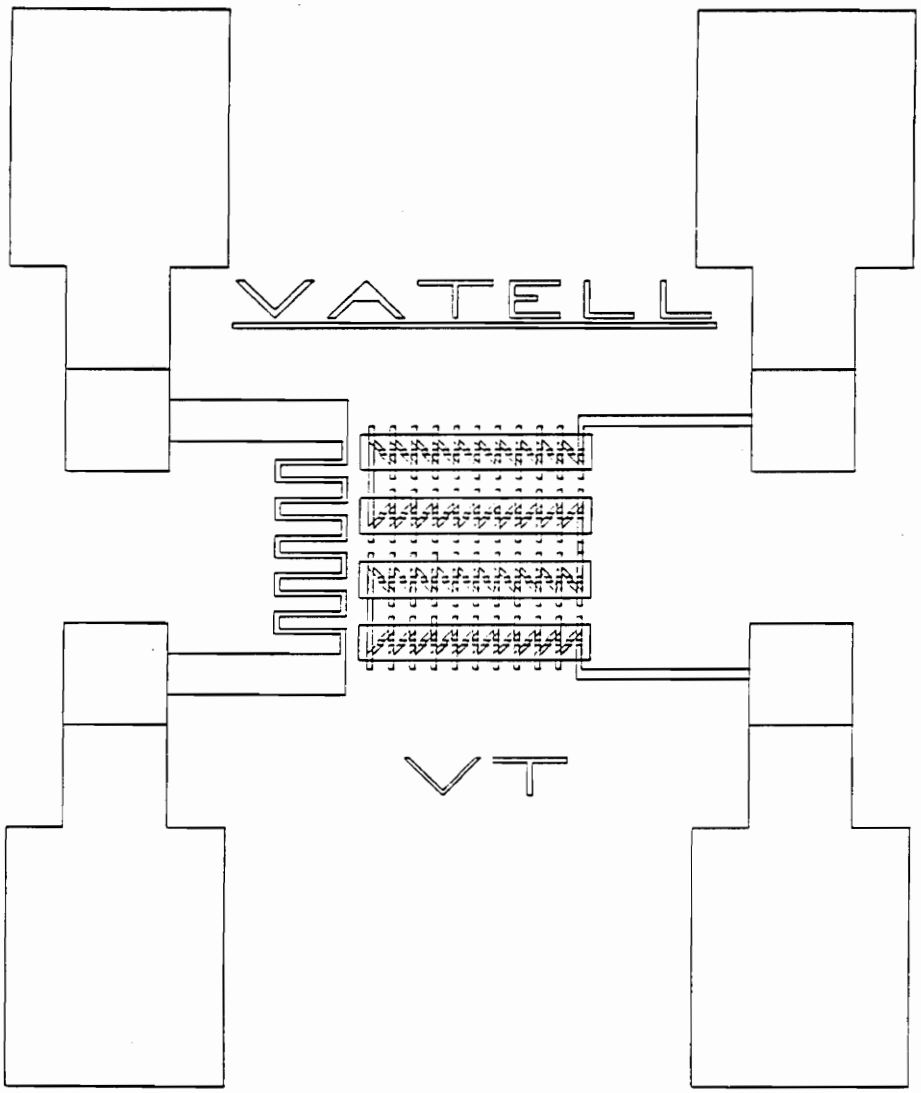

Fig. 11. Heat Flux Microsensor Pattern

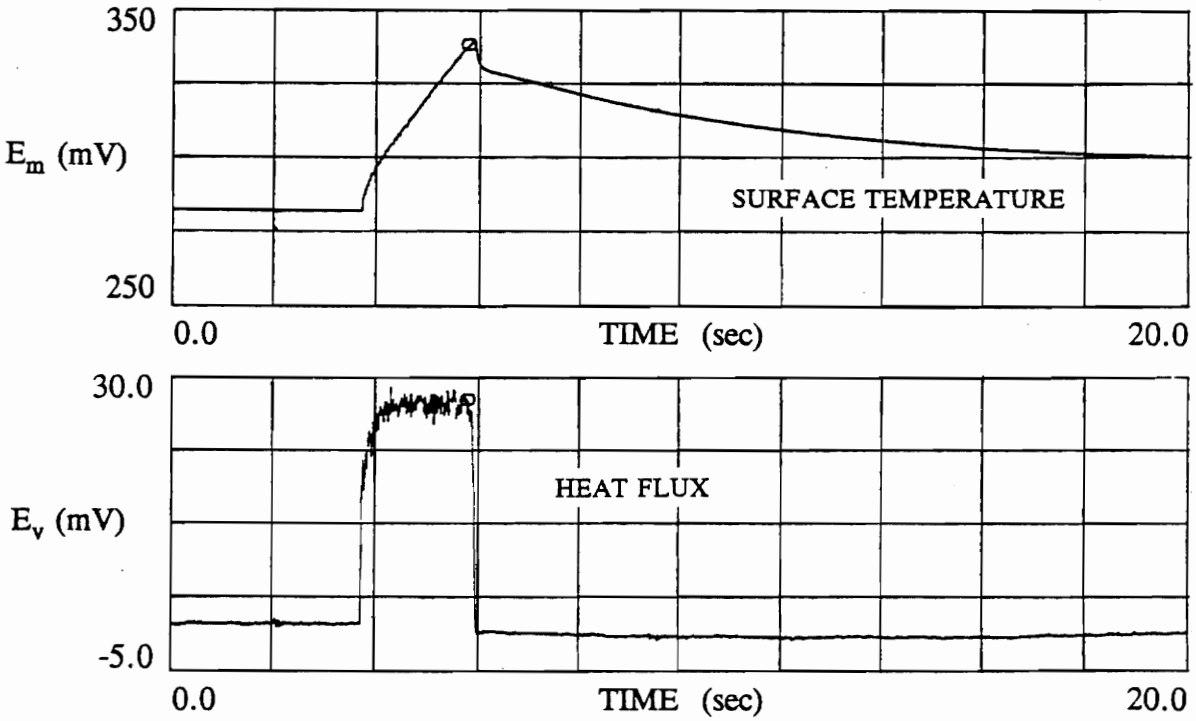

Fig. 12. Microsensor's Response to Instantaneous Heat

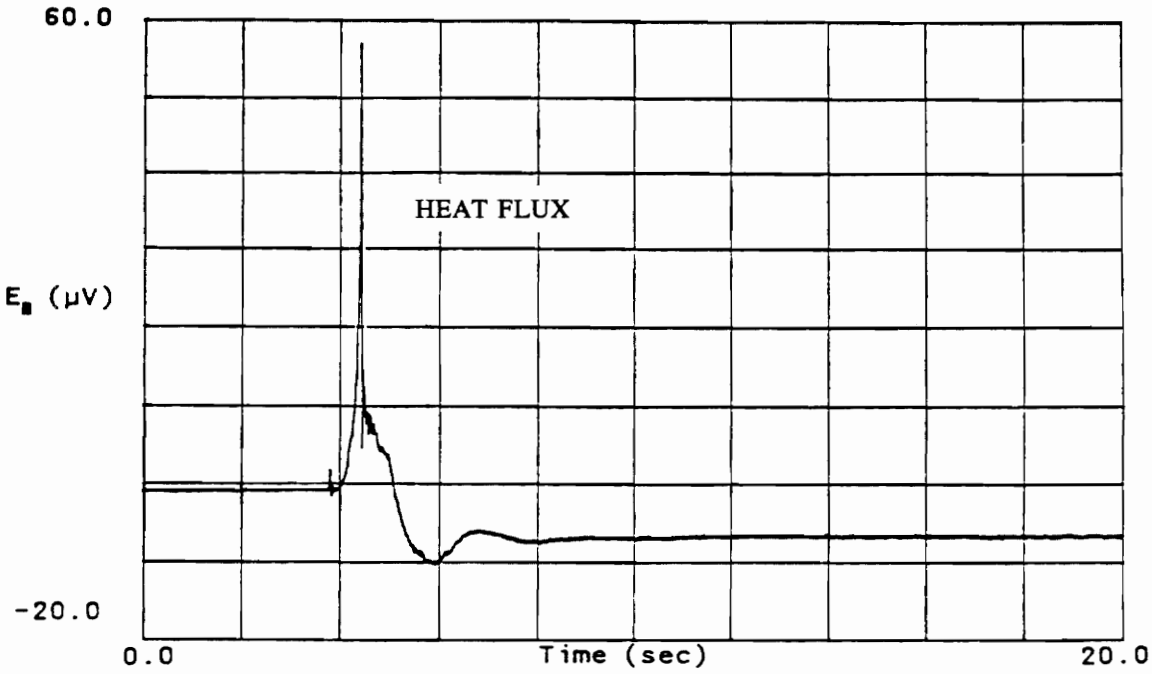

Fig. 13. Microsensor Time Record in Supersonic Flow

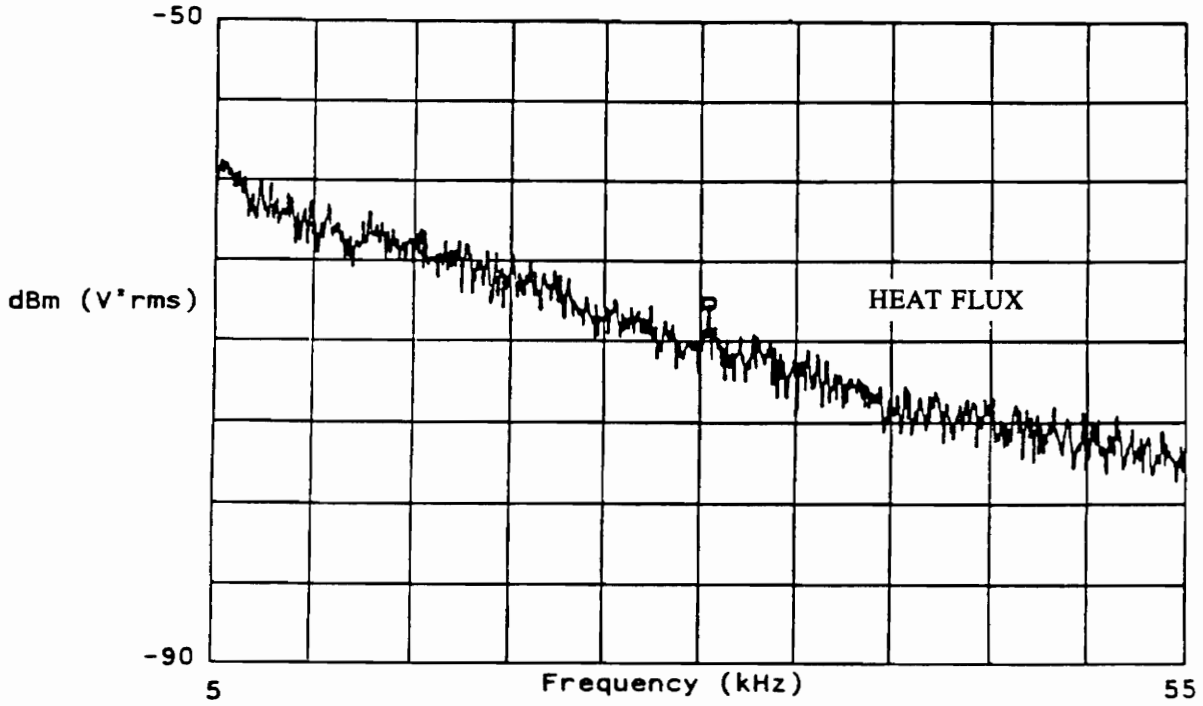

Fig. 14. Microsensor Frequency Spectra in Supersonic Flow

situation for the microsensor was the monitoring of time-resolved heat flux and freestream turbulence at a stagnation point [9]. By simultaneously monitoring each of the signals, the effects of freestream turbulence on boundary layer heat transfer were documented. Test results representing heat flux and flow velocity are shown in Figures 15 and 16. An obvious correlation existed between the heat flux and the velocity unsteadiness. The experimental results showed a phase lag of 60, 70, and 90 degrees on pulses of 590, 960, and 1250 Hz, respectively. These results may have included a phase shift of 180° due to the nondirectional nature of the velocity probe used. Fig. 17 displays the coherence function for the local values of the heat flux and velocity measurements. This coherence level was somewhat low, attributed to the random frequency content of the input signals due to the turbulent unsteadiness. The present research hopes to take these results farther, performing these simultaneous measurements on the complex turbulent vortex system.

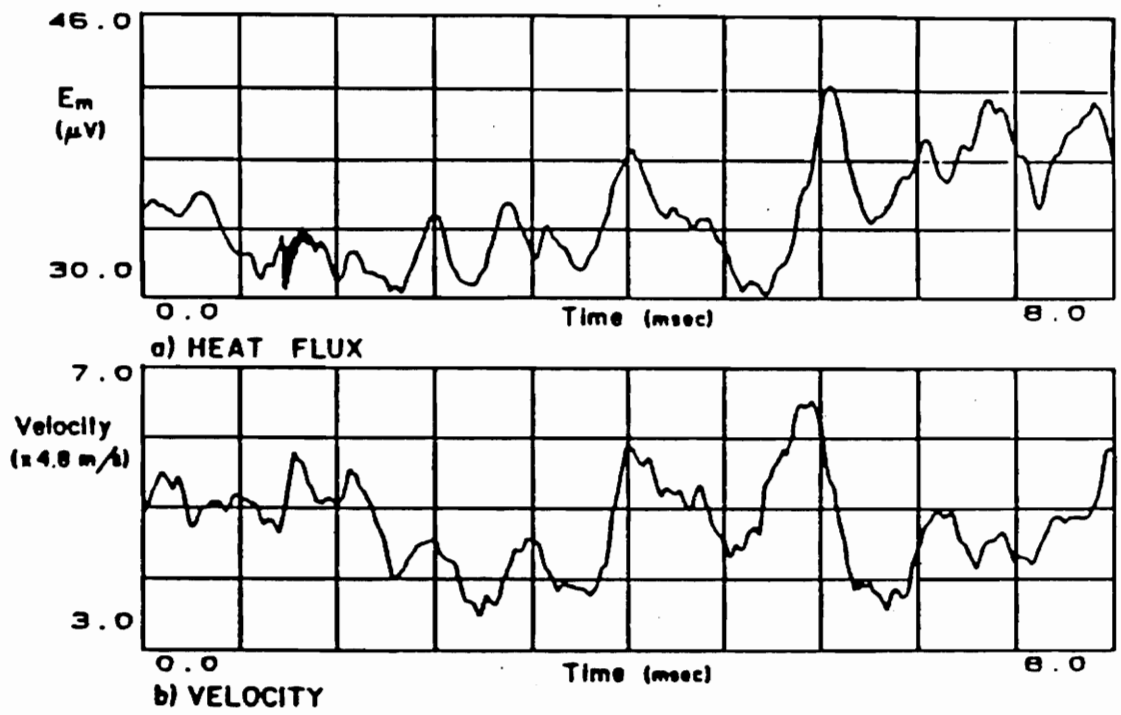

Fig. 15. Simultaneous Heat Flux and Velocity Signals at Stagnation [9]

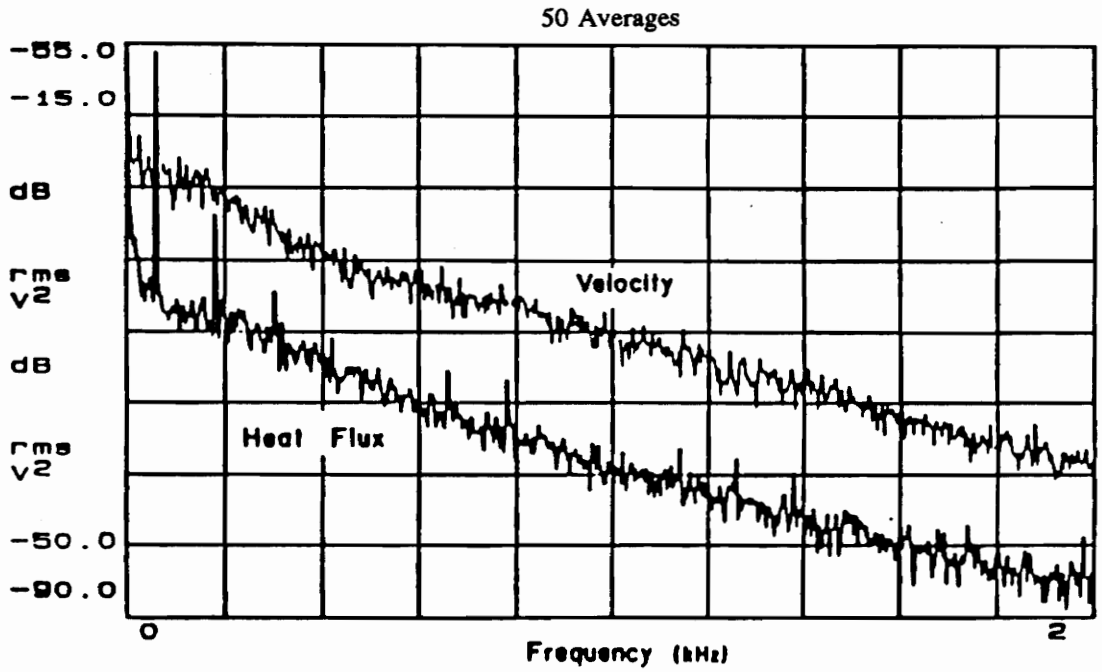

Fig. 16. Heat Flux and Velocity Power Spectra at Stagnation [9]

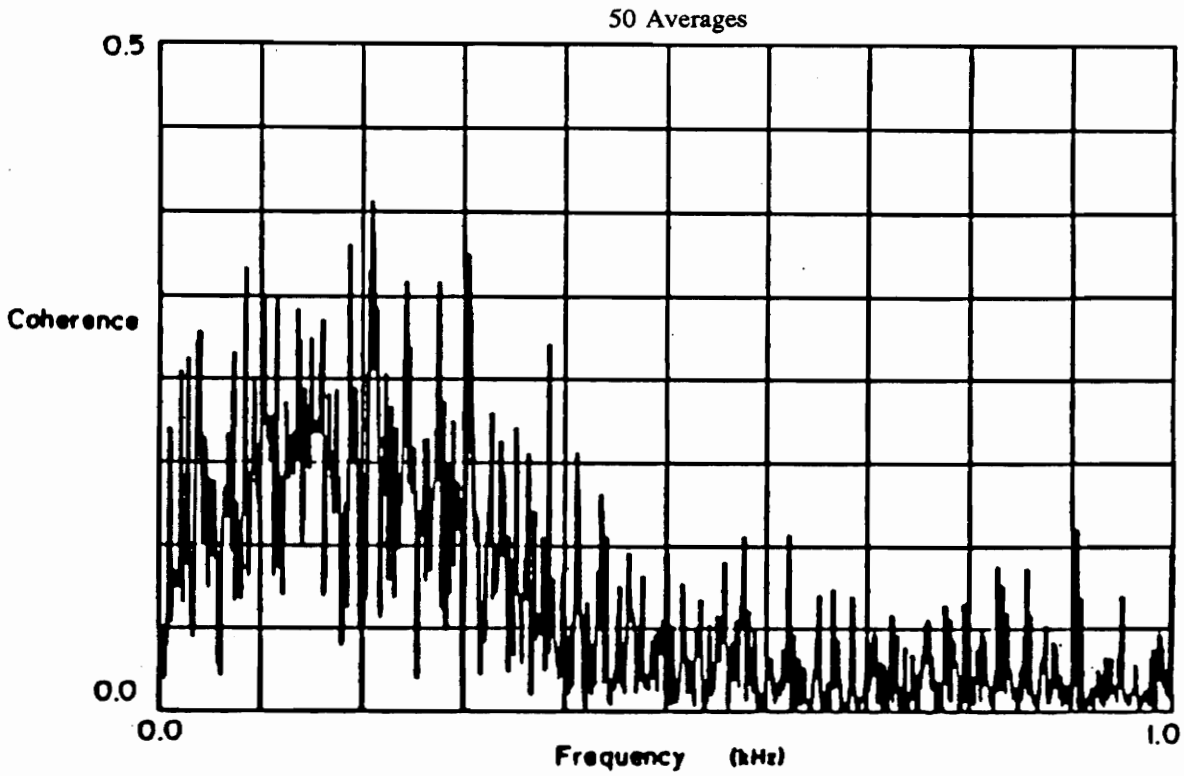

Fig. 17. Coherence of Heat Flux and Velocity at Stagnation [9]

Chapter Three

Experimental Design and Procedure

The turbulent junction vortex system was measured using the Heat Flux Microsensor and a hot-wire anemometer. An airfoil shaped body mounted in a low-speed wind tunnel created the system. This chapter elaborates on the design of the tunnel test section and describes the testing procedures used.

3.1 Experimental Apparatus

The tunnel test section consists of a segmented aluminum plate completing the bottom of the tunnel and a circular cam system that fits flush into the center of the plate. The Heat Flux Microsensor then fits into the cam system for ease of positioning. The segmented plate is comprised of three rectangular pieces, stepped to fit together to form a level test section which will not trip the flow in the tunnel. Modeling clay was used to fill the small cracks between the plate and the tunnel floor. To provide insulation between

the pieces and also to provide some additional stability to the configuration, RTV blue silicone gasket maker was applied to the step edges. Because of the insulation between the pieces of the plate, only the center piece containing the cam system must be heated before testing. Dimensions for the plate are given in Fig. 18. A hole is drilled in the center section to position the airfoil shaped body in the flow path. The wooden body dimensions are shown in Fig. 19. It is bolted to the bottom of the tunnel through the hole in the center piece. In the two outside pieces holes are drilled from the bottom of the plate to attach metal bars. These bars are tightened against the bottom of the tunnel by screws to prevent movement of the segmented pieces from heat, settling, or a vacuum created by the flow.

The cam system allows the Heat Flux Microsensor to be easily positioned along the symmetric axis of the flow field [23]. It is made of two aluminum discs, 1.27 cm (0.5 in) thick, the smaller fitting into the larger with an offset from the center of 2.22 cm (0.875 in). By rotating one or both of the pieces the microsensor is incrementally "walked" along the symmetric line. Dimensions of the system are given in Fig. 20. A steel collar is mounted to the smaller disc to hold the probe body containing the microsensor in place.

Velocity measurements are taken with a single-wire hot-wire anemometer placed directly above the Heat Flux Microsensor. It is positioned from one side of the tunnel by a small aluminum holder attached to the tunnel floor with cyanoacrilate. The distance between the two instruments is 1.905 cm (0.75 in).

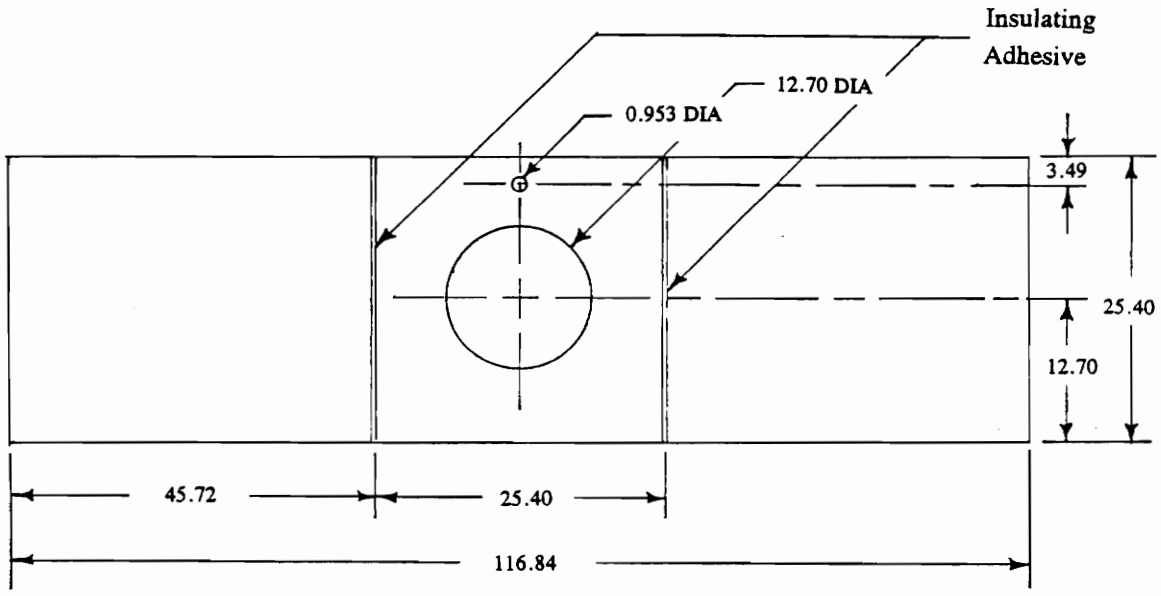

(all units in cm)

Fig. 18. Segmented Plate of Tunnel Test Section

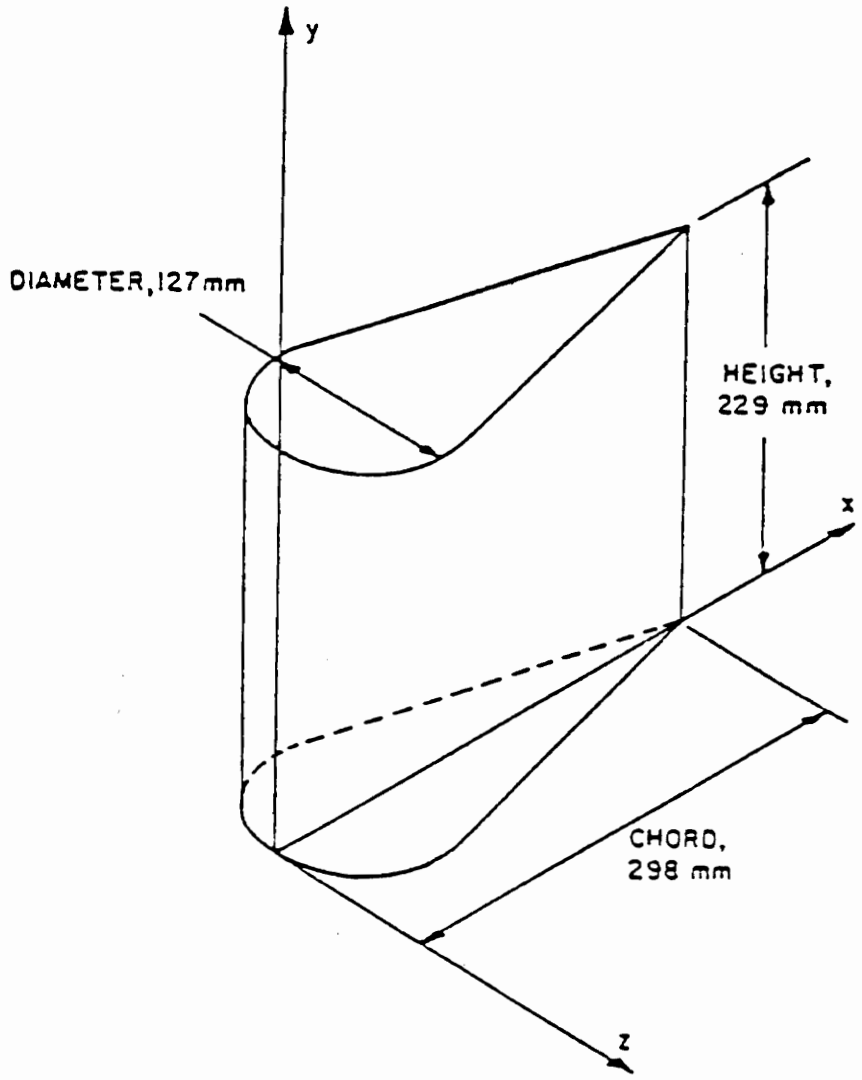

Fig. 19. Streamline Cylindrical Body and Coordinate System

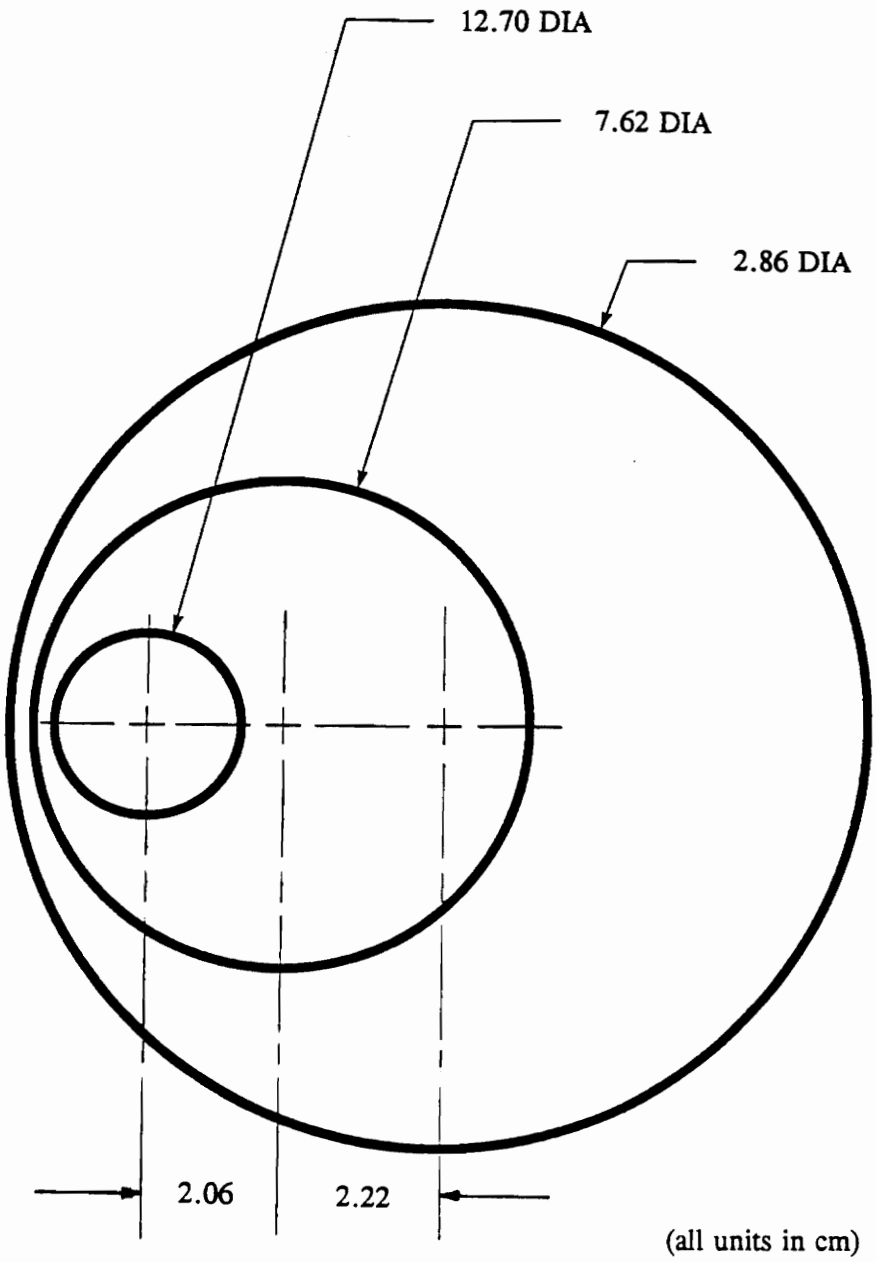

Fig. 20. Rotating Cam System of Tunnel Test Section

The wind tunnel itself is a suction-type tunnel that creates a low-speed turbulent vortex system when the body is positioned in the flow. A two-dimensional turbulent boundary layer, nominally 90 mm (3.54 in) thick, develops over the five meter (16.4 ft) long floor upstream of the test section. The Reynold's number based on length is 5,740,000. The rectangular cross section of the wind tunnel test section is 0.91 m (3.0 ft) wide by 0.61 m (2.0 ft) high. The typical freestream velocity is approximately 24.0 m/s (78.7 ft/s), fixing the Reynold's number based on the diameter of the body to 183,000. The upstream momentum Reynold's number is 12,500 [1].

To heat the center piece of the segmented plate to a constant and uniform temperature, four silicone wire resistance heaters are mounted flush against the bottom side of that piece. These flexible rubber covered heaters are used to cover the area of the plate while still allowing for the probe body to protrude from the plate. Type-T thermocouples are placed between the plate and the heaters to provide feedback to control the temperature. Both the thermocouples and the heaters are held in place by fiberboard screwed into the plate which also served to inhibit dissipation of heat. The heaters are individually controlled by Eurotherm 810 automatic temperature controllers and Eurotherm 831 power supplies. The probe body encasing the Heat Flux Microsensor is also heated from the bottom of the tunnel using a 150 W band heater and a variac.

3.2 Experimental Procedure

In preparation for testing, the cam system is carefully positioned. Test sites along the symmetric axis are chosen by studying LDV measurements of the horseshoe vortex reported by Pierce and Tree [1]. The Heat Flux Microsensor is then leveled and secured in the collar. Lead wires connect the microsensor to a portable amplifier which is monitored by a Hewlett-Packard 3562A dynamic signal analyzer. The resistance temperature sensor (RTS) which measures the surface temperature of the microsensor is connected by lead wires to the portable amplifier and then monitored on a Hewlett-Packard 3468A digital multimeter. The body is then placed in the tunnel and clear silicone sealant is applied around the bottom; this is to ensure that the flow is directed only around the body and is not trapped under it. After these instruments are in place, the hot-wire anemometer is positioned over the sensor and the anemometer holder is mounted to the tunnel floor. The hot-wire is connected to a TSI IFA-100 constant temperature anemometer which, in turn, is connected to the HP signal analyzer.

After the zero values of both the Heat Flux Microsensor and the RTS are recorded, the Eurotherm heaters and the band heater on the probe body are allowed to stabilize at approximately 80°C. This is accomplished by monitoring the RTS surface temperature reading with the HP multimeter as well as monitoring the Eurotherm controller digital displays. Noise distorting the signals is lowered by momentarily shutting down the heaters during the data collecting stages. If the duration of a test is more than

roughly a minute, the RTS temperature is allowed to rise above 80° before data collection in an attempt to compensate for the decrease in temperature.

After this preparation, the tunnel velocity is adjusted to a test section freestream value of approximately 24.0 m/s (78.7 ft/s). The velocity is measured with a pitot tube inserted through the top of the test section approximately 25.4 cm (10.0 in) above the airfoil shaped body.

3.2.1 Heat Flux and Temperature Measurement

As discussed in the experimental apparatus section, the Heat Flux Microsensor has leads from the heat flux gage for the heat flux signal and from the RTS for the surface temperature. These leads are connected to a portable differential amplifier.

The heat flux leads are connected to a dc amplifier detailed in Fig. 21. This portable amplifier box is designed and constructed by Vatell. The leakage resistance, specifically R4 and R5, takes the noise out of the circuit as well as out of the bias amplifier which is referenced to ground. The gain applied to the signal through this circuit is 1000. The signal is then run into the HP signal analyzer to record data.

The RTS leads are also connected to the portable battery-operated amplifier with a circuit as shown in Fig. 22. The calibration switch, along with a null adjustment, forces the amplifier to be zero so that there is a zero reference prior to every measurement. When switched to the run mode, the output of the voltage divider is

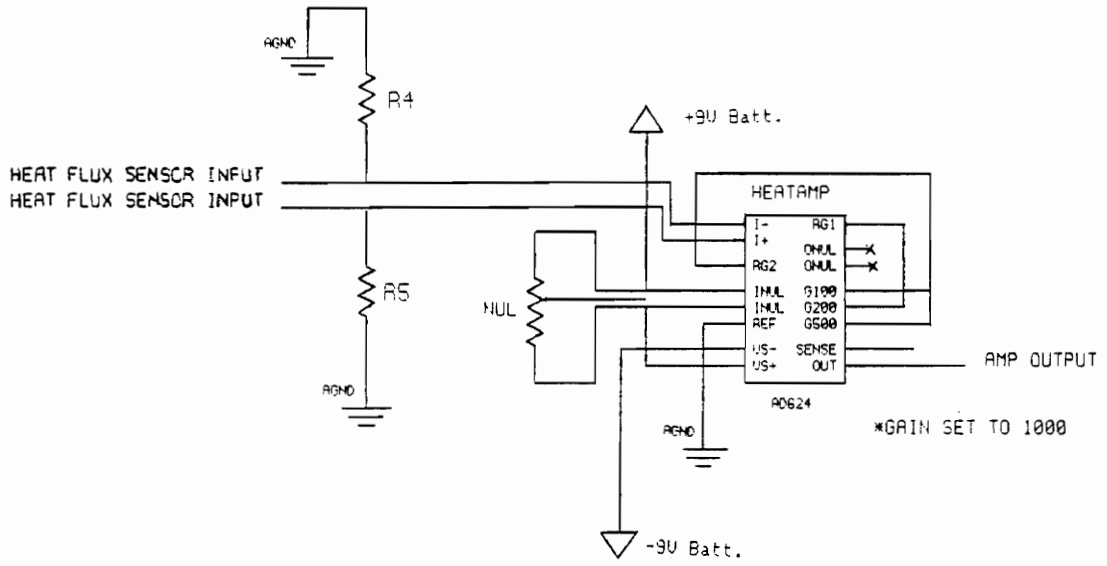

Fig. 21. Heat Flux Circuit and Amplifier

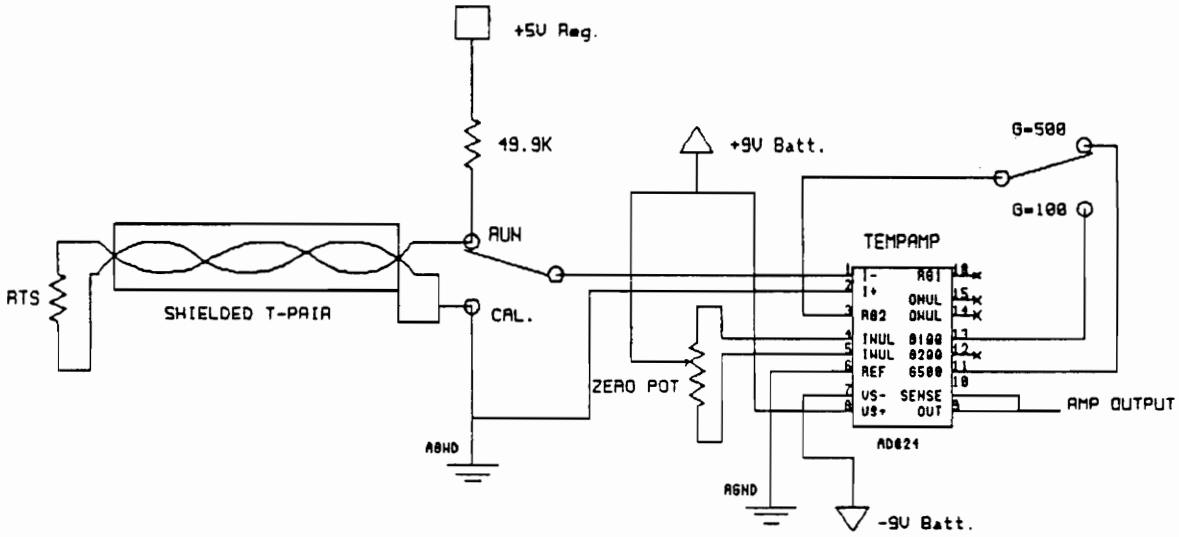

Fig. 22. RTS Circuit and Amplifier

approximately proportional to the RTS resistance. The noise level is reduced by using shielded, twisted pair connections from the RTS to the amplifier and by the common-mode rejection of the differential amplifier itself. The RTS signal is amplified by 500 and run into the HP multimeter to monitor this data.

3.2.2 Velocity Measurement

The hot-wire anemometer is used to measure information about the velocity characteristics of the flow at the same x-coordinate position as the Heat Flux Microsensor. Because the single-wire anemometer cannot account for direction in the flow, the sensor is tested in a parallel position as well as a perpendicular position to give more information about the flow field. The unlinearized signal from the IFA-100 flow analyzer is directed into the signal analyzer. Tests were also run with the anemometer probe at several positions in the boundary layer for comparison purposes. The calibration for the hot-wire is discussed in Appendix B.

3.2.3 Time-Resolved Testing

Time records were taken and filtered with a low-pass filter for valid frequencies. The plots themselves show heat flux in voltage versus time and velocity in voltage versus time. From these tests, average heat flux and velocity values can be determined. Average

turbulence correlations were also calculated from the fluctuation values of the signals.

3.2.4 Power Spectra Testing

Power spectrum measurements were taken showing the output heat flux and velocity signals in the frequency domain. The HP signal analyzer calculated the power spectrum by multiplying the FFT of the signal by its complex conjugate. Stable mean averaging, weighting old and new data records equally to yield the arithmetic mean, was used. The number of averages taken was 100. From these tests, turbulence correlations for a specific frequency were calculated. The two measurements were also compared in coherence plots. The coherence function is an indication of the statistical valid correlation of the frequency response measurement. Coherence is measured from zero to one, where one indicates perfect coherence.

An ICP 302A accelerometer was attached to the Heat Flux Microsensor to determine which frequencies in the response, if any, were due to vibrations of the experimental set-up or the wind tunnel itself. These results are shown in Appendix D.

Chapter Four

Results

Time-resolved heat flux and velocity measurements were taken at three positions in the turbulent junction vortex system: position one, at the dominant vortex center; position two, the separation point behind the dominant vortex; and position three, near the attachment region between the vortex and the airfoil. The surface heat flux was simultaneously monitored with the velocity at that position to observe the effects of fluid unsteadiness. Measurements in the same region without the airfoil, or the classic boundary layer case, were also recorded for comparison purposes.

The time-resolved heat flux and corresponding velocity signals for each of these positions are shown in Figs. 23, 27, 31, and 35. The mean heat flux, the mean convection coefficient, and the fluctuating turbulence values were calculated from the Heat Flux Microsensor's signal. Similarly, the mean velocity and velocity fluctuations were calculated from the hot-wire signal. These results are presented in Table 1.

The frequency spectrum of the heat flux and velocity signals are shown in Figs.

24, 28, 32, and 36. Since stable averaging was performed in this frequency domain, the coherence function was used to identify correlation between the heat flux and the velocity. Coherence plots are displayed in Figs. 25, 29, 33, and 37. The turbulence level at individual frequencies was examined and graphed in Figs. 26, 30, 34, and 38. Unlike other spectrum plots, these turbulence plots give meaningful statistics at each spectral line instead of simply showing trends. Average turbulent coefficients were calculated from both the time-resolved and power spectra data and are presented in Table 2. For comparison, the coherence was plotted with the hot-wire out of the boundary layer. This plot is displayed in Fig. 39.

Initially, the frequency span was varied to pinpoint the activity of the vortex system. From this study, it was discovered that the majority of the flow unsteadiness occurred in the first 100 Hz. The span's starting frequency was 5 Hz; by cutting out the dc component of the signal, resolution was improved. The bandwidth of the span was 0.125 Hz. The number of averages was also varied to investigate the effects of spurious data, or singular occurrences in the data not indicative of the flow. After comparison of initial tests, data taken with more than 100 averages was redundant. All of the results presented in this section were repeatable by duplication of the experiment.

Table 1. Time-resolved Data for the Junction Vortex System

Time-resolved Data	P1 vortex ctr	P2 separation	P3 attachment	classic bl
$\overline{q''}$ (W/m^2)	-8568.5	-12422.9	-9927.8	-4462.2
$\bar{h}$ $(W/m^2 * K)$	214.2	225.9	183.8	81.1
$\bar{v}$ (m/s)	11.79	12.85	7.80	20.17
$\overline{Tu_{hf}}$	0.302	0.186	0.211	0.211
$\overline{Tu_{hw}}$	0.155	0.130	0.220	0.220
St	0.0076	0.0081	0.0066	0.0029

Table 2. Turbulence Data for the Junction Vortex System *

Turbulence coefficients	P1 vortex ctr	P2 separation	P3 attachment	classic bl
$\overline{Tu_{hf}}$ *(time)*	0.302±0.116	0.186±0.104	0.211±0.094	0.211±0.056
$\overline{Tu_{hw}}$ *(time)*	0.155±0.112	0.130±0.103	0.220±0.106	0.220±0.104
$\overline{Tu_{hf}}$ *(power)*	0.238±0.048	0.166±0.033	0.206±0.041	0.100±0.020

* **Time-resolved results are ± a 95% confidence interval.**

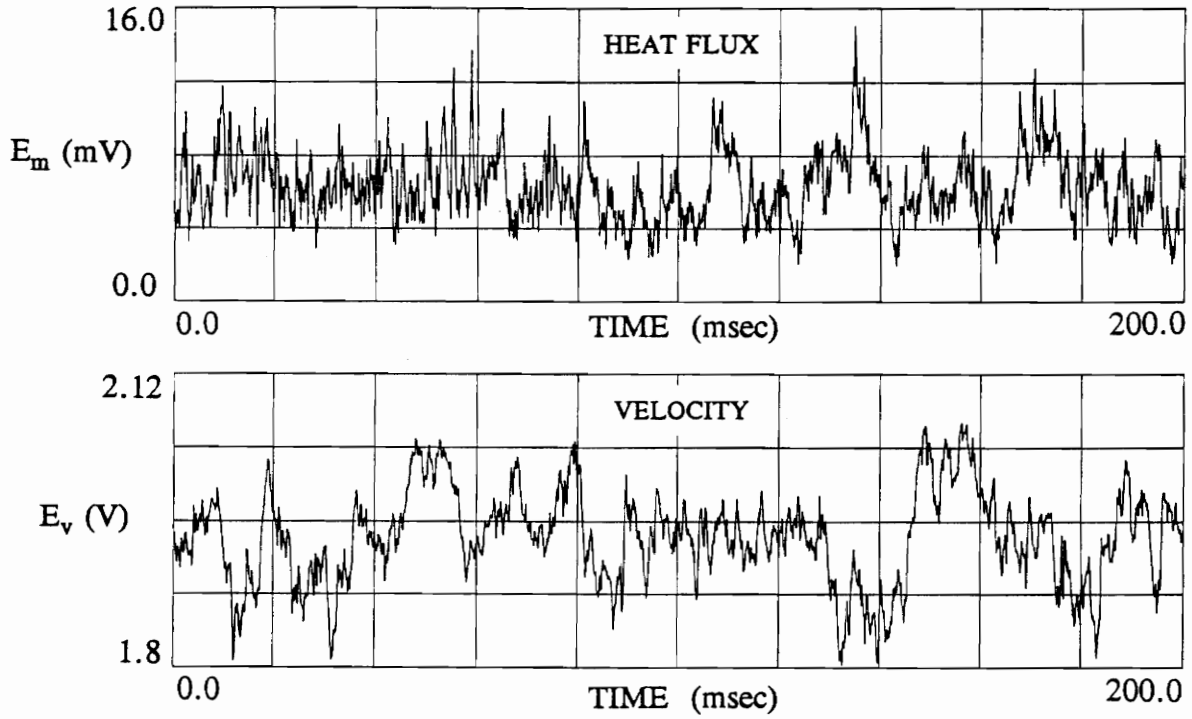

Fig. 23. Time-resolved Heat Flux and Velocity at Vortex Center

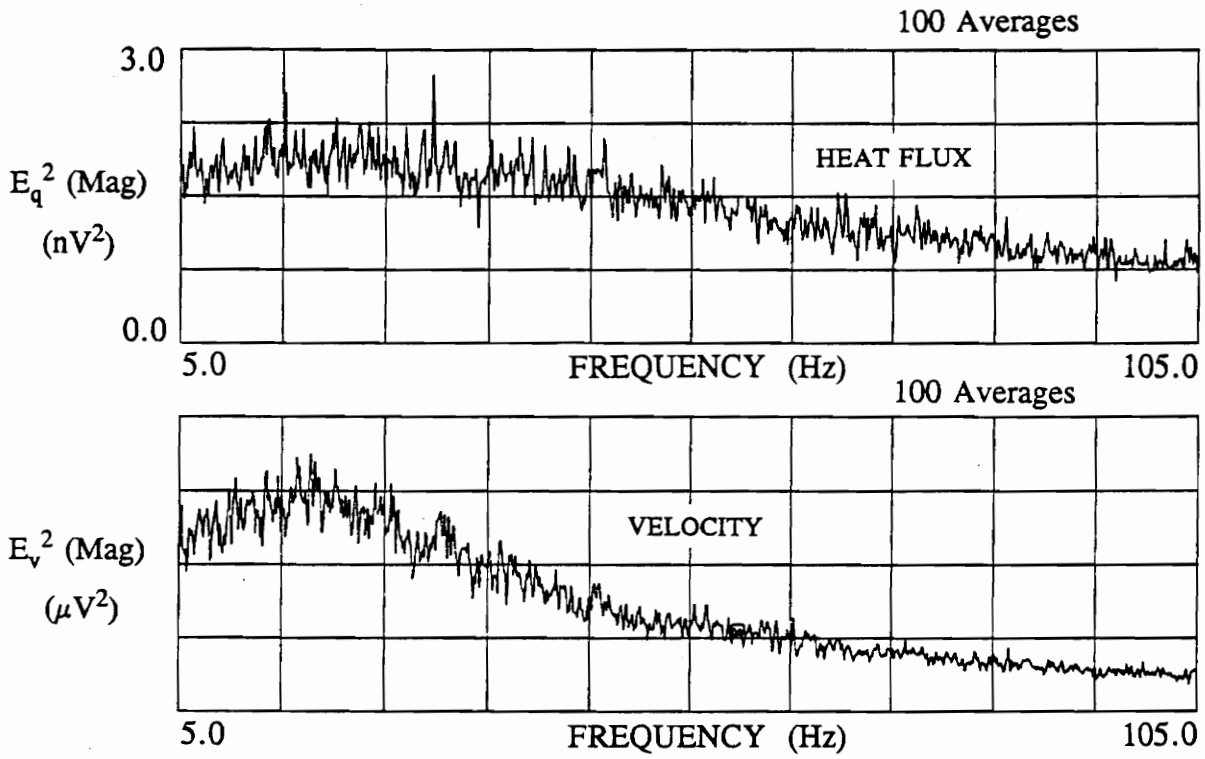

Fig. 24. Power Spectra of Heat Flux and Velocity at Vortex Center

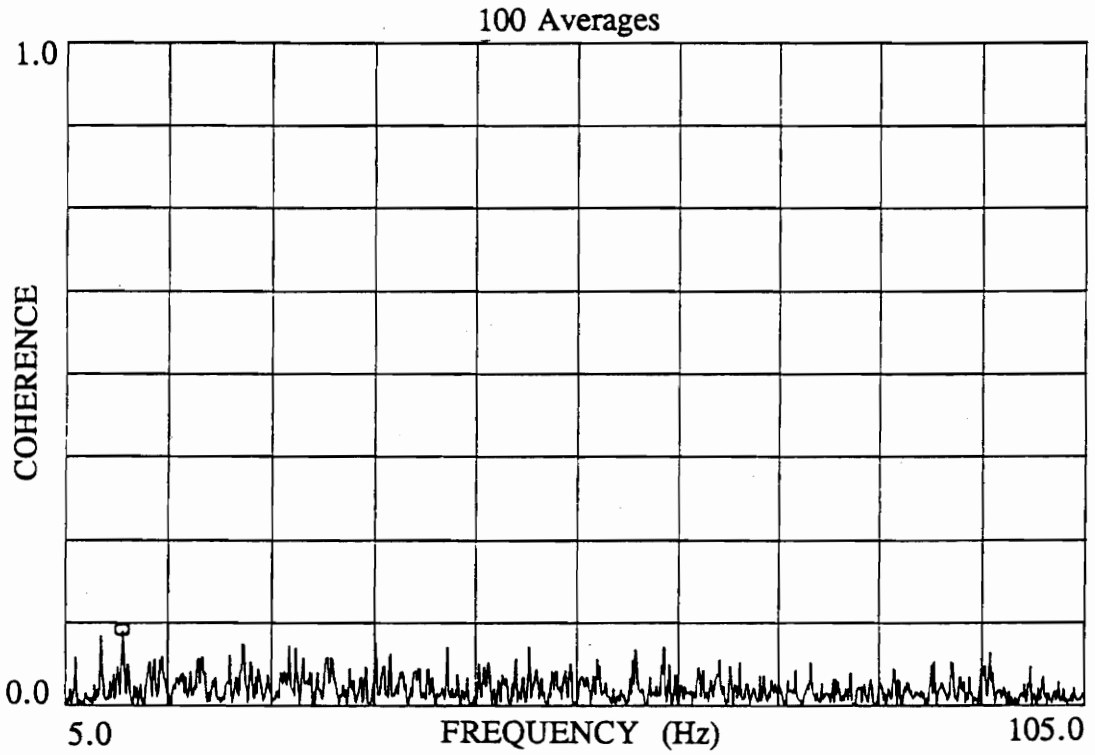

Fig. 25. Coherence Between Heat Flux and Velocity at Vortex Center

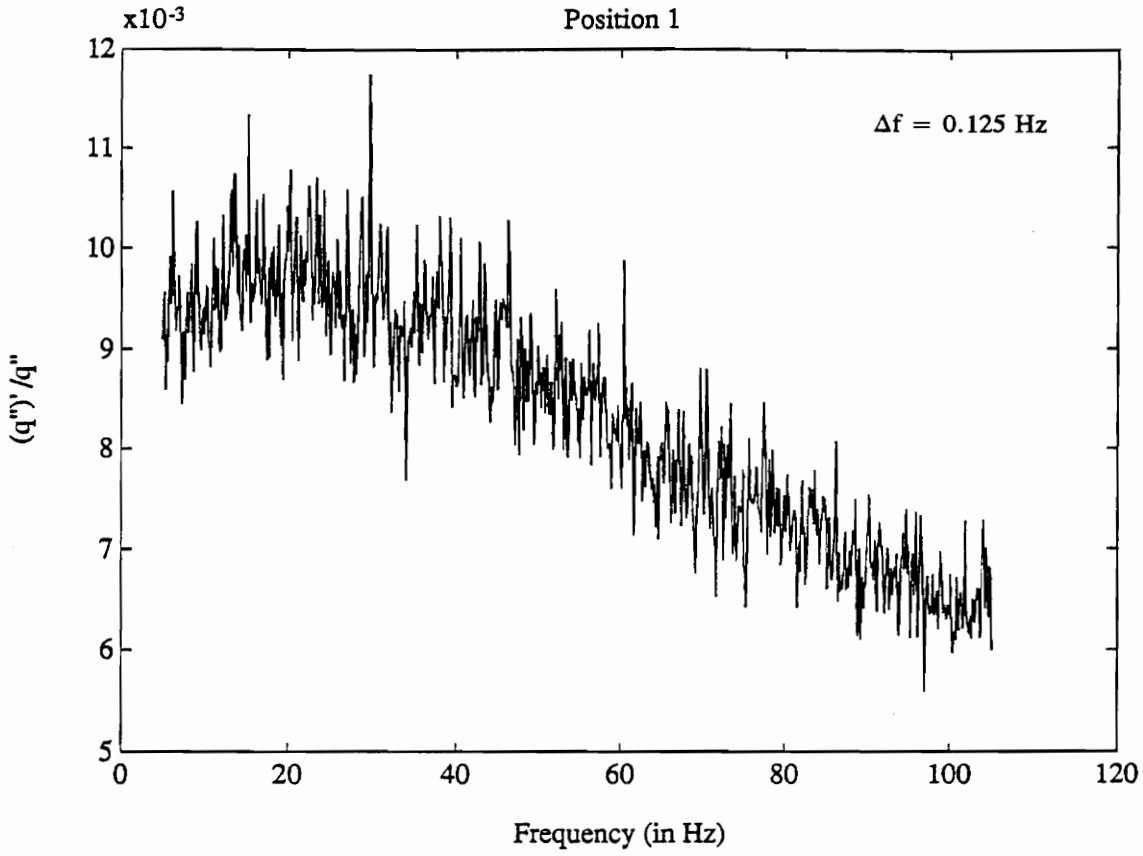

Fig. 26. Turbulence Levels of Heat Flux at Vortex Center

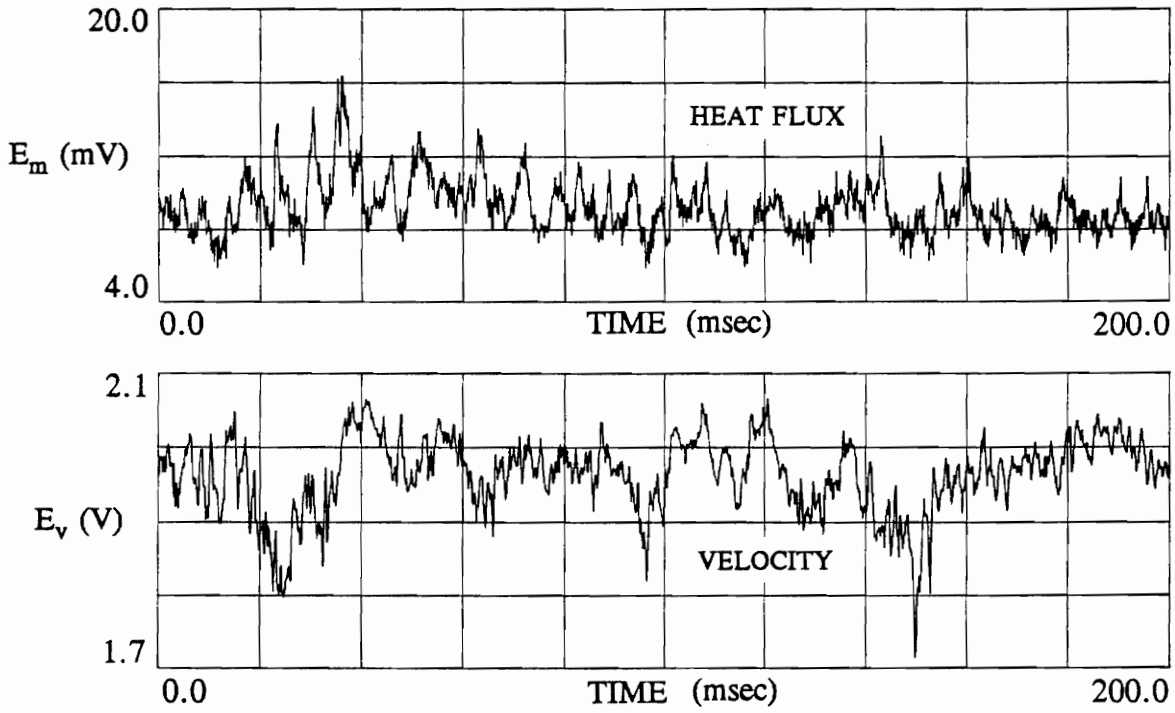

Fig. 27. Time-resolved Heat Flux and Velocity at Separation Point

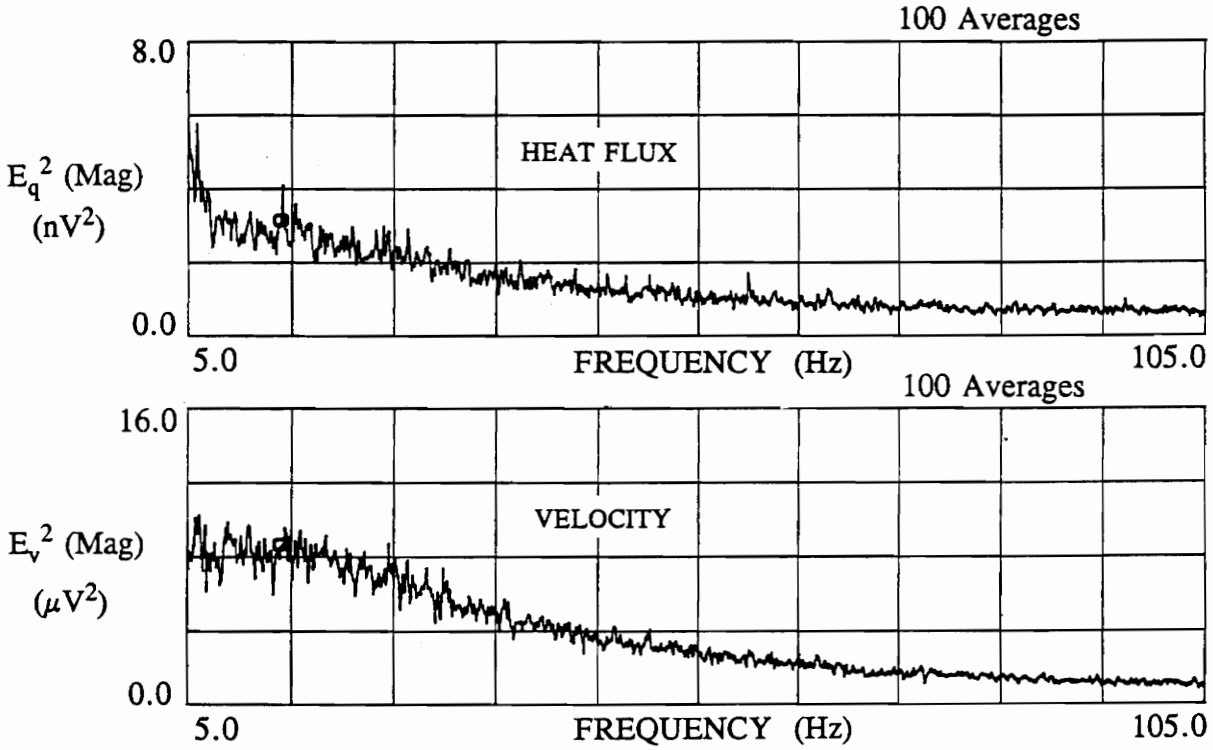

Fig. 28. Power Spectra of Heat Flux and Velocity at Separation Point

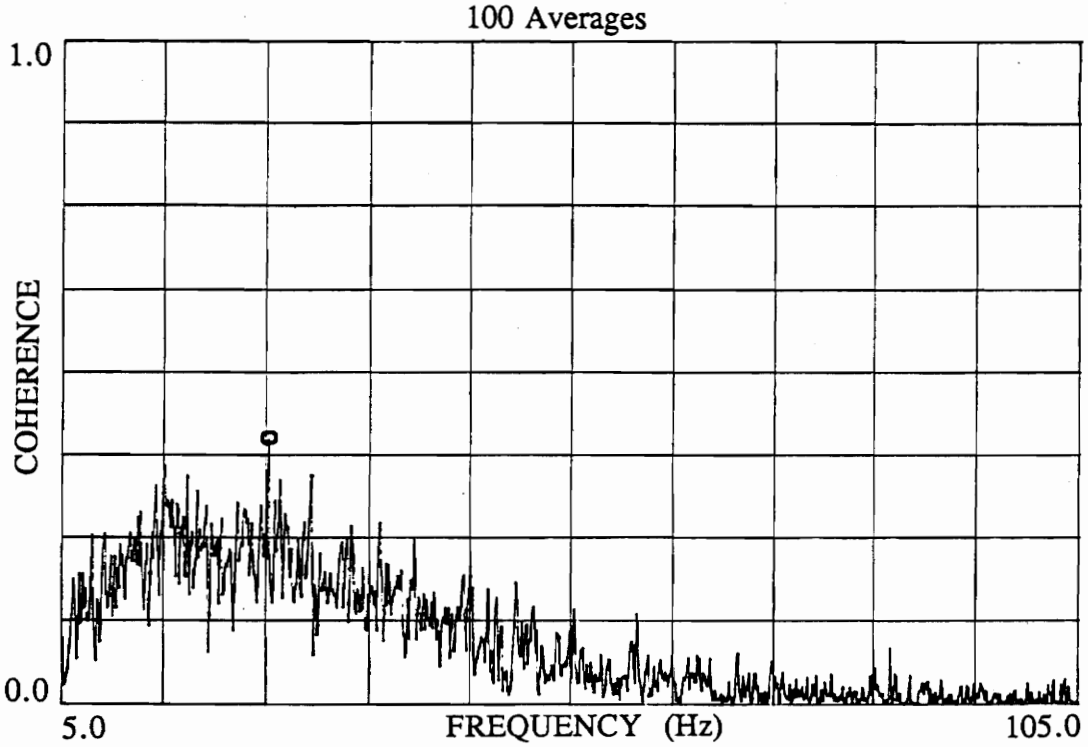

Fig. 29. Coherence Between Heat Flux and Velocity at Separation Point

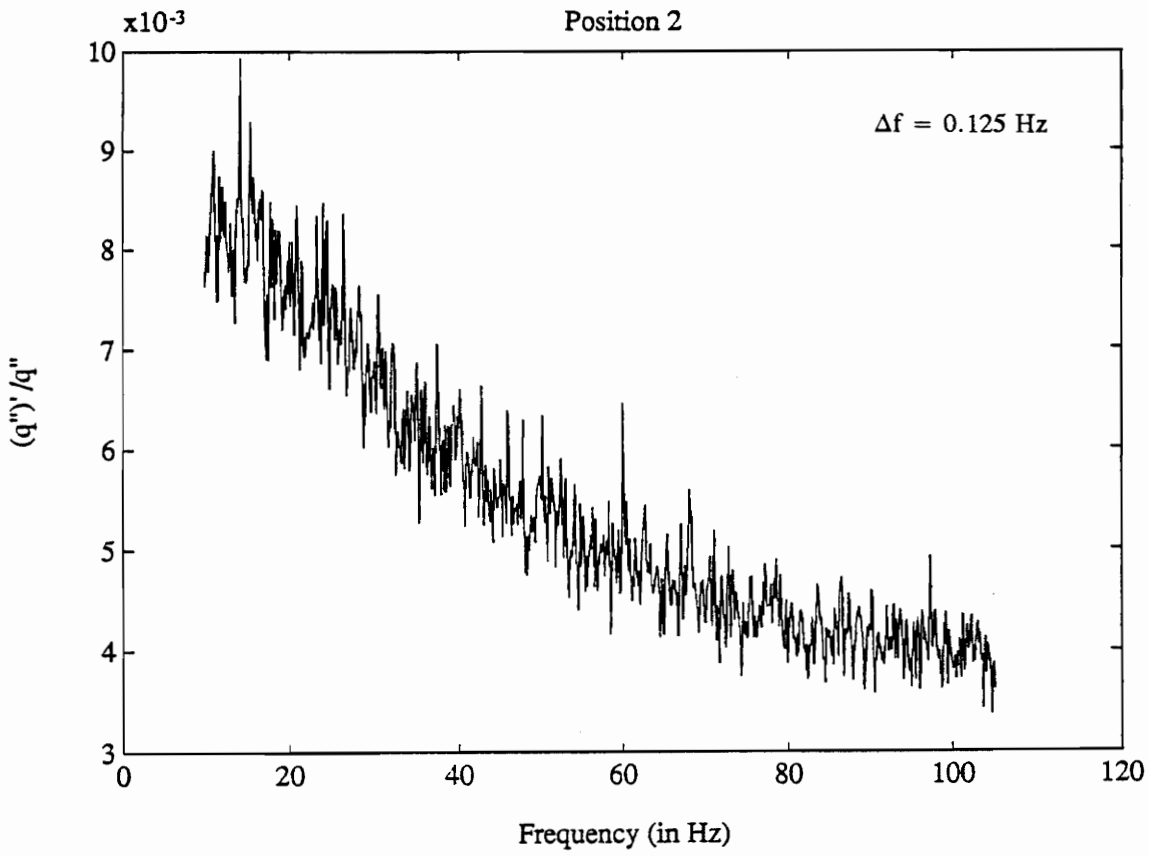

Fig. 30. Turbulence Levels of Heat Flux at Separation Point

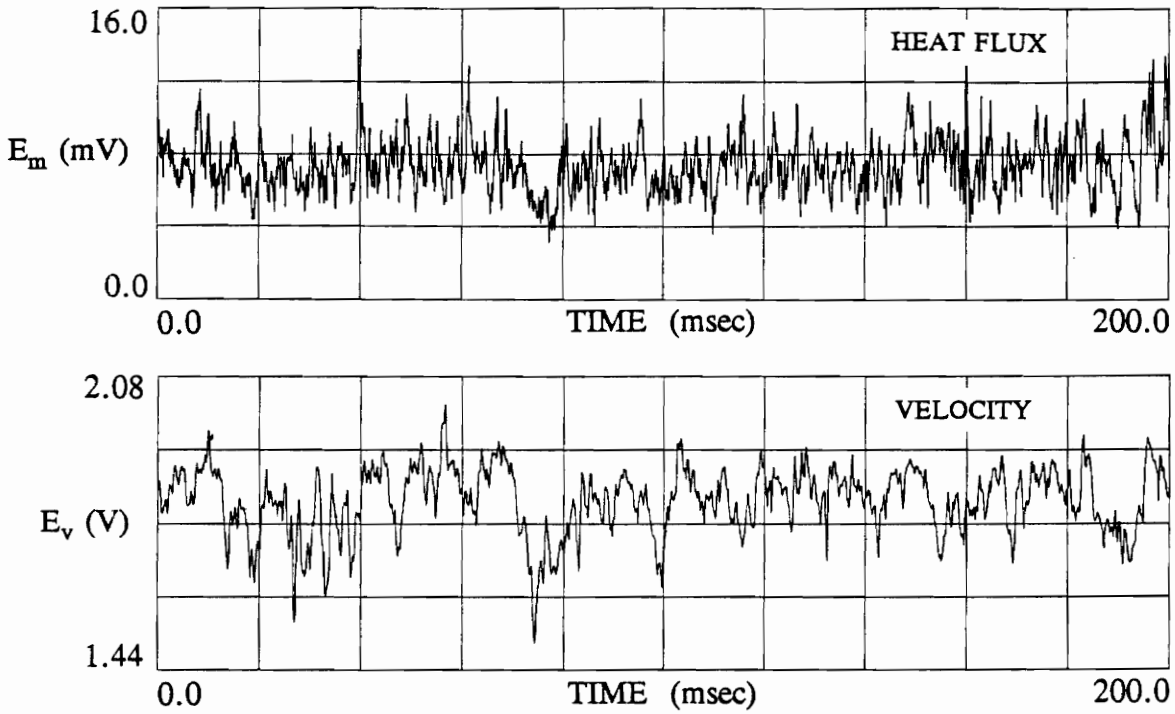

Fig. 31. Time-resolved Heat Flux and Velocity in Attachment Region

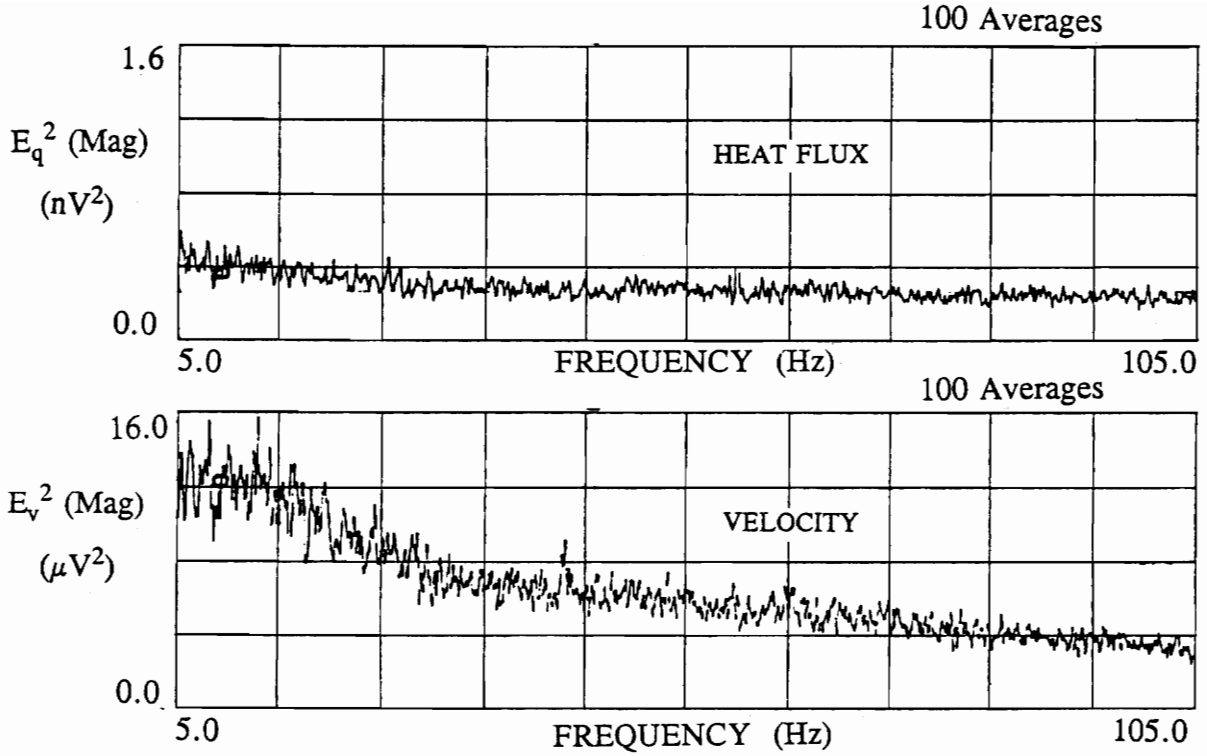

Fig. 32. Power Spectra of Heat Flux and Velocity in Attachment Region

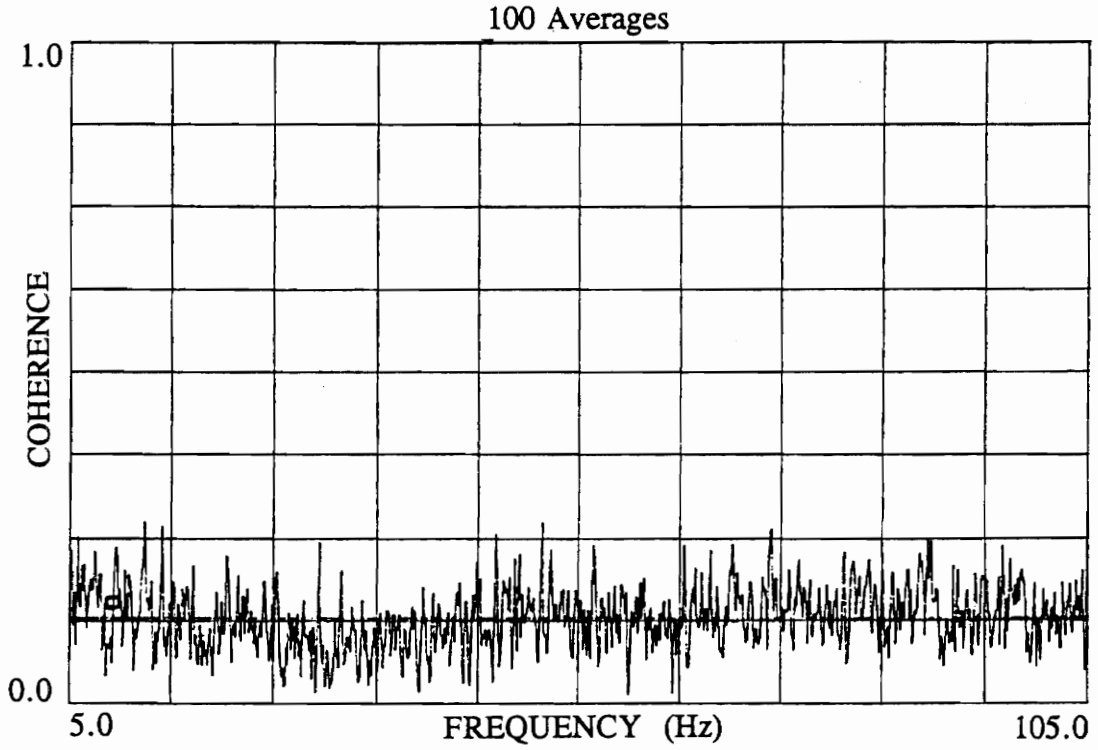

Fig. 33. Coherence Between Heat Flux and Velocity in Attachment Region

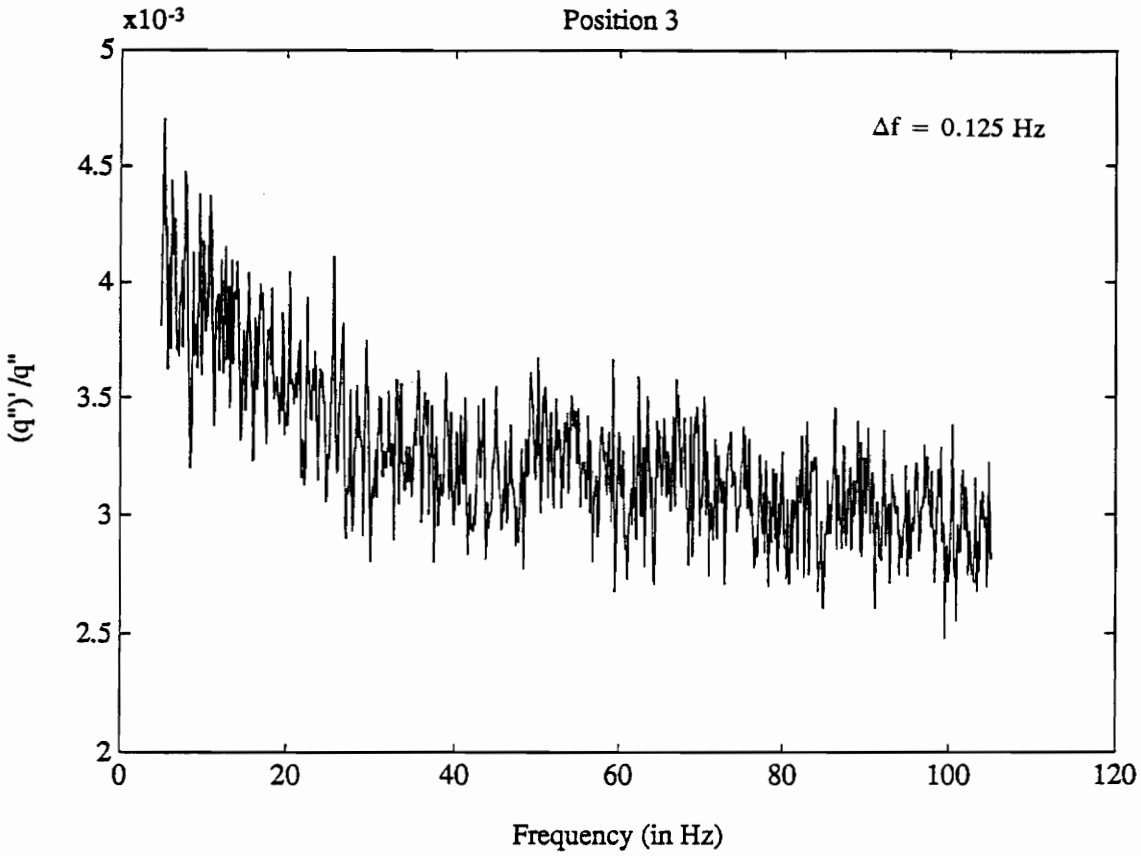

Fig. 34. Turbulence Levels of Heat Flux in Attachment Region

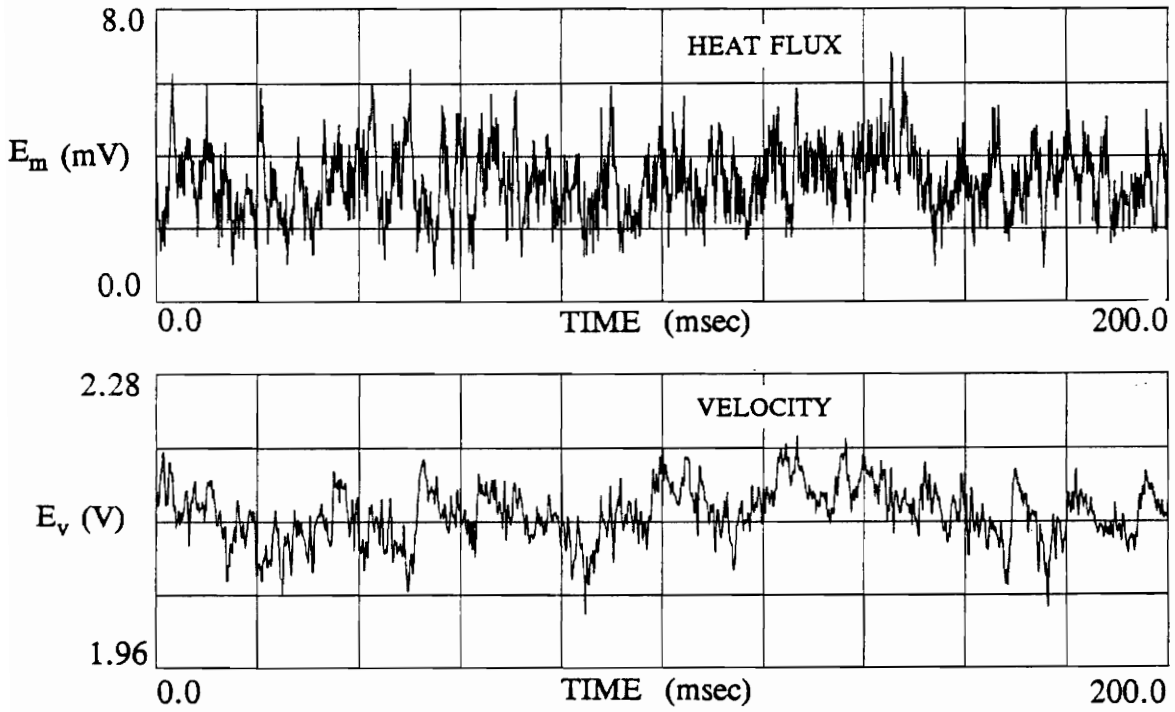

Fig. 35. Time-resolved Heat Flux and Velocity in Classic Boundary Layer

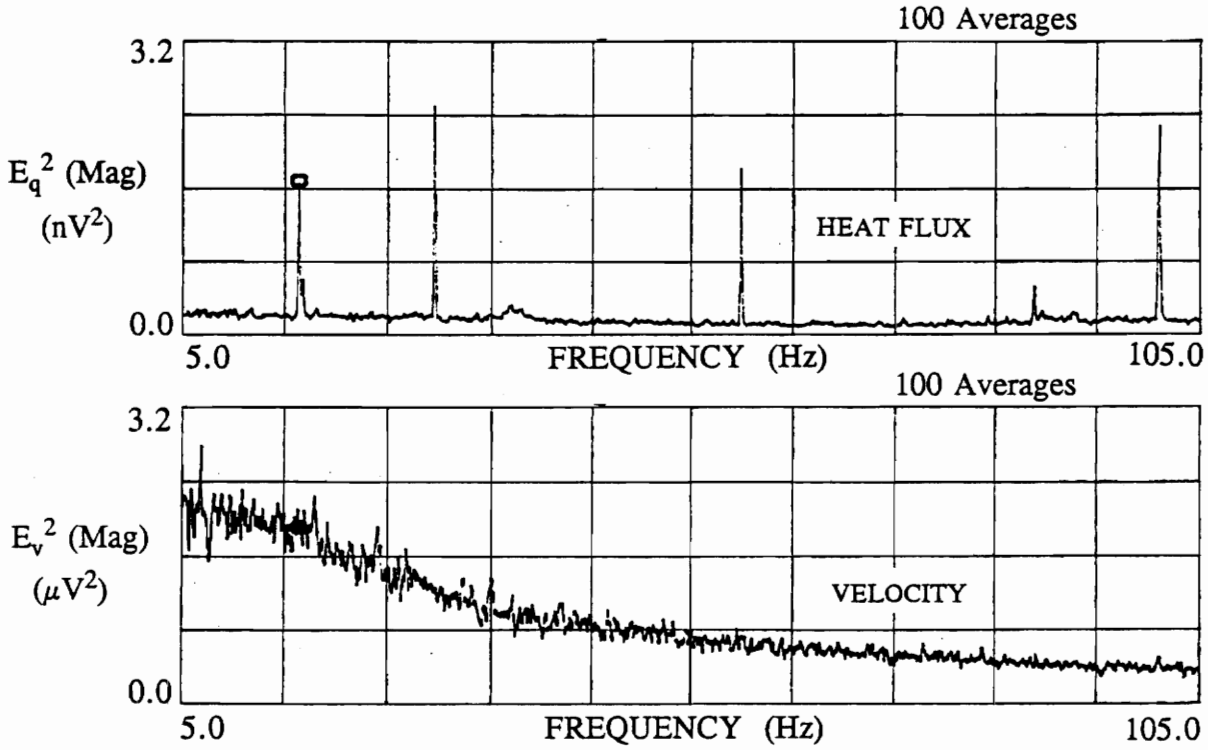

Fig. 36. Power Spectra of Heat Flux and Velocity in Classic Boundary Layer

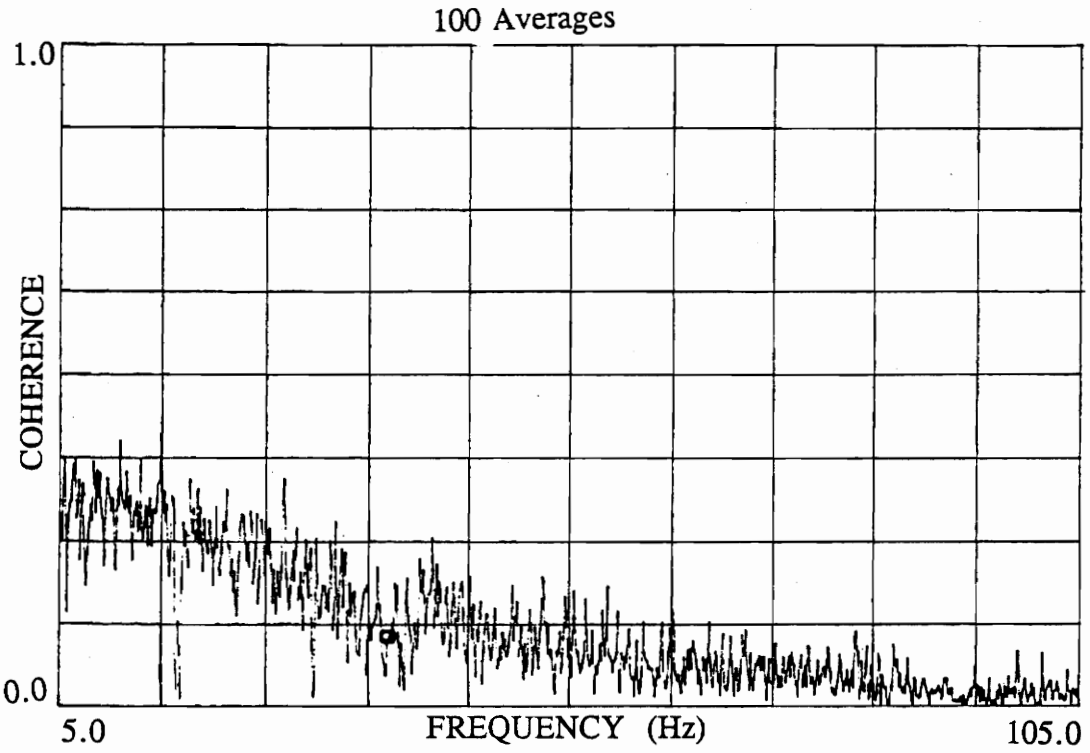

Fig. 37. Coherence Between Heat Flux and Velocity in Classic Boundary Layer

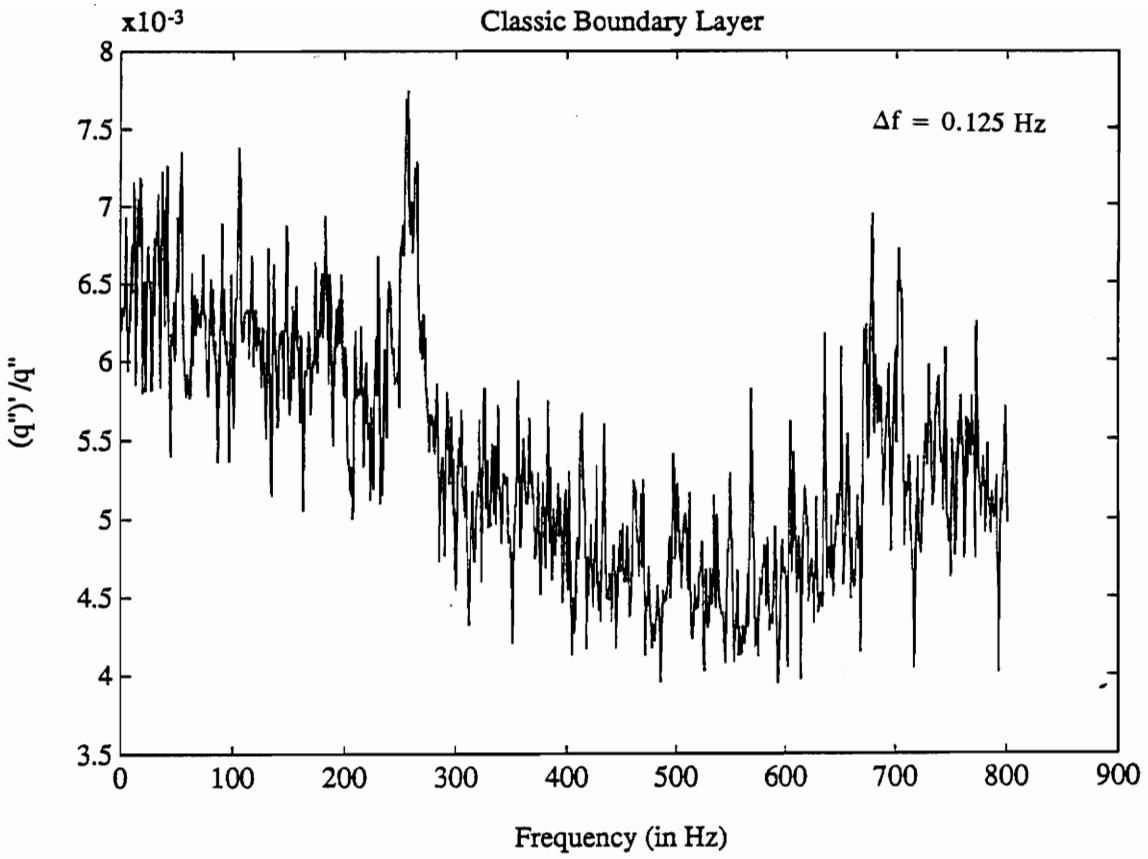

Fig. 38. Turbulence Levels of Heat Flux in Classic Boundary Layer

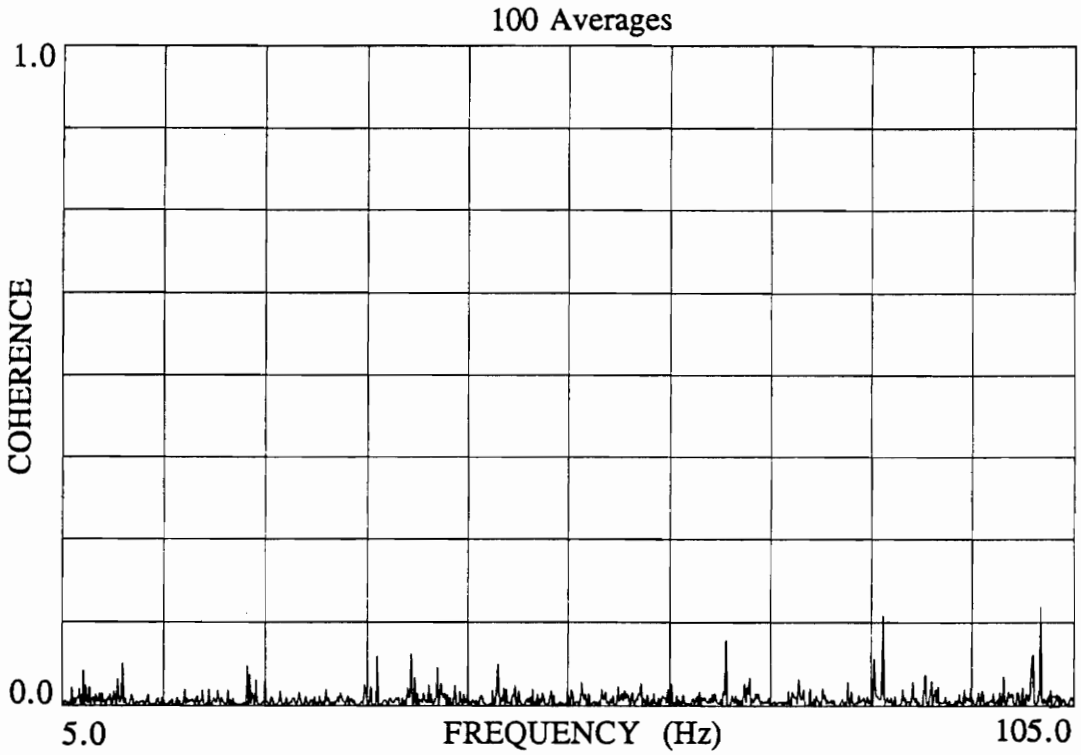

Fig. 39 Coherence with Anemometer Out of Boundary Layer

Chapter Five

Discussion of Results

Measurements concentrated on the junction vortex because of its dominance and importance to the flow region at the leading edge of the airfoil. The junction vortex significantly enhances the turbulent structure which greatly complicates the flow. Since the turbulent junction vortex system is a complex three-dimensional flow, results obtained from its study must be carefully interpreted. Measurements were taken in both the time and frequency domains.

5.1 Time-Resolved Measurements

Because of the turbulent activity of this region, the time-resolved signals shown in Figs. 23, 27, 31, and 35 are mostly random; turbulent flows are characteristically random. Although the heat flux gage and hot-wire signals are similar, there is no obvious

correlation of heat flux and velocity unsteadiness visible from these plots. However, similarities are evident for calculated turbulent coefficients for each of the signals showing an equivalent turbulence magnitude (see Table 2). This agreement increases the confidence of using the Heat Flux Microsensor as a turbulence-measuring device.

Because of the difficulty in making time-resolved heat flux measurements, the results of the Heat Flux Microsensor are essential to providing a basic understanding of the heat flux in the vortex system. The highest heat flux was discovered at position three, the separation point. With the vortex moving back and forth at this point, the level of activity is expected to be quite high, thus resulting in an area of high heat flux. In comparison, the low heat flux of the classic boundary layer case, only 36% of the heat flux at separation, shows how significantly the dominant vortex affects the heat transfer. For this research, heat flux was defined as positive from the surface and negative to the surface. Clearly, the heat flux values should be and are positive because heat is being convected away from the surface. To further validate the microsensor as a time-resolved heat flux device, Stanton numbers, or nondimensionalized heat transfer coefficients based on inlet conditions, were calculated for each of the positions. These numbers were comparable to the results of Hippensteele and Russell [14] shown in Figs. 6 and 7. For the classic boundary layer case, an empirical value of the Nusselt number considering the unheated starting length was calculated by the formulas [24]:

$$Nu_x = \frac{[Nu_x]_{\xi=0}}{[1-(\xi/x)^{9/10}]^{1/9}}$$

and

$$[Nu_x]_{\xi=0} = 0.0296 Re_x^{4/5} Pr^{1/3}$$

where x was measured from the leading edge of the unheated starting length, and ξ was measured from the beginning of the thermal boundary layer development. The values of x, ξ, and Re_x were 5.127 m, 5.0 m, and 5,740,000, respectively.

The Stanton number was then calculated from the definition:

$$St = \frac{Nu_L}{Re_L Pr}$$

The empirical Stanton number was 0.0025, a 16.0% difference. If the unheated starting length is not considered, the empirical Stanton number is 0.0017, a factor of 1.5 lower. Examination of the frequency data taken by the Heat Flux Microsensor will continue to show the gage's capacity to measure the flow unsteadiness and its effects on the heat transfer.

5.2 Frequency Measurements

The power spectra of the heat flux and velocity signals are shown in Figs. 24, 28,

32, and 36. For positions one and two, heat flux and velocity have similar frequency content. This is indicated by the shape of the power spectra and implies that both devices are measuring the same flow pattern. Position three and the classic boundary layer case do not follow this trend. These differences may be attributed to the placement of the hot-wire anemometer in the flow. Because the hot-wire is mounted at a distance above the microsensor, at that particular point, the two devices might not be measuring the same phenomena. While discrepancies in the frequency content are often related to propagation errors, this type of error is unlikely in the vortex system flow because the dominant vortex is not propagated downstream.

Additional information can be inferred from calculating the coherence of heat flux and velocity. The coherence function indicates how well the two signals correlate, or rather, if there is a linear relationship between them. Figs. 25, 29, 33, and 37 show coherence functions for the four regions. While positions one and three exhibit little or no coherence, position two and the two-dimensional case have coherence levels up to 0.4. Although this measure of correlation may seem low, the unsteadiness of the flow creates random frequency content in each of the input signals. Lack of coherence in positions one and three is, again, probably a function of velocity probe placement. Another explanation for little or no coherence is random phase. If the magnitudes of the signals are the same but the phases are not, the coherence function will not indicate any correlation. From these observations, it is reasoned that position two documents the movement of the large horseshoe vortex because of its similar frequency content and

reasonable level of coherence. Power spectrum measurements made with the hot-wire positioned both in and out of the boundary layer show that correlation between the two devices exists only, as expected, in the boundary layer (see Fig. 39). This result is in agreement with Simmons, Hager, and Diller [9] who state that the interaction of the turbulence with the boundary layer appears to be crucial to the resulting effect on the surface transfer.

Unsteadiness of the junction vortex system is examined using both the time-resolved and the power spectrum measurements. For the time-resolved data, the following standard turbulence definitions were used to quantify the unsteadiness:

$$\overline{Tu_{hf}} = \frac{\sqrt{\overline{((q'')')^2}}}{\overline{q''}}$$

for the heat flux, and

$$\overline{Tu_{hw}} = \frac{\sqrt{\overline{(v')^2}}}{\bar{v}}$$

for the velocity.

The time-resolved data are useful to calculate an average turbulence value, but also include error resulting from spurious data. This matter can be rectified by obtaining turbulence values from the averaged power spectrum measurements by the formula:

$$\overline{Tu} = \frac{\sqrt{power\ data}}{time\ data}$$

This equation also follows the standard definition of turbulence. The average of the data for this coefficient must be extracted from the time data; an average of the power data does not include the dc component of the signal. This component was taken from the power data to improve resolution. By calculating these coefficients, how each frequency band contributes to the overall turbulence can be discerned. Another problem arises in the calculations due to the phenomena called leakage. Because the data is in discrete form, frequency content is only recorded at the spectral lines. Since there is also content between these lines, frequency components of this neglected content is distributed throughout some to all of the recorded spectral values. To further complicate the process, destructive interference occurs in the Fast Fourier Transform (FFT) of the signal analyzer resulting from the effects of the data window. For this analysis, a $\cos^2$ Hanning window was used and was compensated for in Figs. 26, 30, 34, and 38. Since some frequencies have been discarded from the study, namely frequencies below 5 Hz and above 105 Hz, some of the power of the signal has also been discarded. Thus, the calculated total power of the spectrum is diminished. Consequently, turbulence coefficients calculated from the frequency measurements will be slightly lower than coefficients calculated using the time-resolved data. These discrepancies are shown in Table 2. The best agreement in the unsteadiness measurements is in the attachment

region. The time-resolved microsensor and hot-wire data agrees within 4%, and the microsensor's time-resolved and power spectrum data agrees within 2%. Since the flow is curling downward in this region, the placement of the hot-wire anemometer was probably not as critical to the accuracy of the measurements. Although agreement between the microsensor and anemometer results could not be analytically predicted, they did show correlation at certain positions, and therefore, were compared linearly.

Chapter Six

Conclusions and Recommendations

The present investigation provides results which can be used in an effort to gain a fundamental understanding of the flow unsteadiness and its effect on the heat transfer of the turbulent junction vortex system. Additionally, this work provides the first measured data of the time-resolved surface heat flux of the vortex system.

The following conclusions are made based on the results of this research:

- Time-resolved local heat flux is correlated with flow unsteadiness in some positions of a junction vortex flow.
- The development of the junction vortex system causes three times as much heat transfer to occur in the boundary layer.
- The Heat Flux Microsensor is a reliable source of information about the surface heat flux of the junction flow.
- The turbulence or unsteadiness levels for the vortex system were

as high as 0.3 or 30%. These levels were much higher than expected.

- Some correlation also exists between the local heat flux and the flow unsteadiness in the classic boundary layer case.

The following recommendations are made for future work in the study of the junction vortex system:

- At each position of the heat flux gage, the hot-wire anemometer should be moved vertically to pinpoint the region of the most correlation.
- To avoid problems with the single wire anemometer, such as its uni-directional qualities and its potential for flow disturbance, more precise velocity data could be acquired by a laser Doppler velocimeter.
- To further test the significance of the results obtained using the Heat Flux Microsensor to identify a correlation between heat flux and flow unsteadiness, simpler turbulent flow situations with analytical solutions should be measured with the same technique.

List of References

1. Pierce, F.J., and Tree, I.K., " The Mean Flow Structure on the Symmetry Plane of a Turbulent Junction Vortex," Transactions of the ASME, Vol. 112, 1990, pp. 16-22.

2. Abid, R., and Schmitt, R., " Experimental Study of a Turbulent Horseshoe Vortex Using a Three-Component Laser Velocimeter," AIAA Paper 86-1069, May 1986.

3. Eckerle, W.A., and Langston, L.S., " Horseshoe Vortex Formation Around a Cylinder," ASME Journal of Turbomachinery, Vol. 109, April 1987, pp. 278-285.

4. Devenport, W.J., and Simpson, R.L., " Time-dependent and Time-averaged Turbulence Structure Near the Nose of a Wing-Body Junction," Journal of Fluid Mechanics, Vol. 210, 1990, pp. 23-55.

5. Hunt, J.C., Abell, C.J., Peterka, J.A., and Woo, H., " Kinematical Studies of the Flows Around Free and Surface-Mounted Obstacles; Applying Topology to Flow Visualization," Journal of Fluid Mechanics, Vol. 86, Part 1, 1978, pp. 179-200.

6. Baker, C.J., " The Turbulent Horseshoe Vortex," Journal of Wind Engineering and Industrial Aerodynamics, Vol. 6, No. 1-2, July 1980, pp. 9-23.

7. Karni, J., and Goldstein, R.J., " Endwall Effects on Local Mass Transfer from a Cylinder in Crossflow," Turbulence and Flow Modeling, Eds. C.J. Chen etal., Hemisphere Publishing Corp., New York, 1986, pp. 3-35.

8. Tree, I., " Laser-Doppler Velocimeter Measurements in a Turbulent Junction Vortex," Ph.D. dissertation, Virginia Polytechnic Institute and State University, 1986.

9. Simmons, S.G., Hager, J.M., and Diller, T.E., " Simultaneous Measurements of Time-Resolved Surface Heat Flux and Freestream Turbulence at a Stagnation Point," Heat Transfer 1990, Vol. 2, Hemisphere Publishing Corp., New York, 1990, pp. 375-380.

10. Mori, Y., Koizumi, H., and Nogo, Y., " A Study of the Time and Spatial Micro-Structure of Heat Transfer Performance Near the Separation Point Upstream of a Forward Facing Step," Japanese Research- Heat Transfer, Vol. 18, 1989, pp. 91-103.

11. Graziani, R.A., Blair, M.F., Taylor, J.R., and Mayle, R.E., " An Experimental Study of Endwall and Airfoil Surface Heat Transfer in a Large Scale Turbine Blade Cascade," Journal of Engineering for Power, Vol. 102, 1980, pp. 257-267.

12. Gaugler, R.E., and Russell, L.M., " Comparison of Visualized Turbine Endwall Secondary Flows and Measured Heat Transfer Patterns," Transactions of the ASME, Vol. 106, 1984, pp. 168-172.

13. Hylton, L.D., Mihelc, M.S., Turner, E.R., and York, R.E., " Experimental Investigation of Turbine Endwall Heat Transfer," AFWAL-TR-81-2077, 3 volumes, 1981.

14. Hippensteele, S.A., and Russell, L.M., " High-Resolution Liquid-Crystal Heat-Transfer Measurements on the End Wall of a Turbine Passage With Variations in Reynolds Number," NASA Technical Memorandum 100827, 1988.

15. Goldstein, R.J., and Spores, R.A., " Turbulent Transport on the Endwall in the Region Between Adjacent Turbine Blades," Heat Transfer in Gas Turbine Engines, Ed. D.E. Metzger, ASME, New York, 1987, pp. 75-83.

16. Thum, T.F., and Diller, T.E., " Mass Transfer in Recirculating Blood Flow," Chemical Engineering Community, Vol. 47, Gordon and Breach Science Publishers S.A., 1986, pp. 93-112.

17. Diller, T.E., and Telionis, D.P., " Time-Resolved Heat Transfer and Skin Friction Measurements in Unsteady Flow," Advances in Fluid Mechanics Measurements, Lecture Notes in Engineering, Ed. M. Gadel-Hak, Springer-Verlag, Berlin, 1989, pp. 323-355.

18. Shirtliffe, C.J., and Tye, R.P., Eds., Guarded Hot Plate and Heat Flow Meter Methodology, ASTM, Vol. 879, 1985.

19. Campbell, D.S., Gundappa, M., and Diller, T.E., " Design and Calibration of a Local Heat Flux Measurement System for Unsteady Flows," Fundamentals of Forced and Mixed Convection, Eds. F.A. Kulacki and R.D. Boyd, ASME, 1985, pp. 73-80.

20. Hager, J.M., Onishi, S., Langley, L.W., and Diller, T.E., " High Temperature Heat Flux Measurements," AIAA Paper No. 91-0165, 1991.

21. Hager, J.M., Simmons, S., Smith, D., Onishi, S., Langley, L.W., and Diller, T.E., " Experimental Performance of a Heat Flux Microsensor," ASME Paper No. 90-GT-256, 1990.

22. Hager, J.M., Terrell, J.P., Langley, L.W., Onishi, S., and Diller, T.E., " Measurements with the Heat Flux Microsensor," Accepted for the 37th International Instrumentation Symposium of the Instrument Society of America, San Diego, May 1991.

23. Pierce, F.J., personal conversation, 1990.

24. Incropera, F.P., and DeWitt, D.P., Fundamentals of Heat and Mass Transfer, second edition, Wiley and Sons, Inc., New York, 1985, pp. 319-322.

25. Gundappa, M., Hudson, J.F., and Diller, T.E., " Jet Impingement Heat Transfer from Jet Tubes and Orifices," Heat Transfer in Convective Flows, Ed. R.K. Shah, ASME, New York, 1989, pp. 43-50.

26. Myers, Raymond H., Classical and Modern Regression with Applications, second edition, PWS-Kent Publishing Co., Boston, 1990.

Appendix A

Jet Impingement Experiment

This appendix describes the testing of the Heat Flux Microsensor and its precursors in an array of impinging air jets. These arrays are widely used for heating, cooling, and drying of substrates including heat treating glass, internal cooling of gas turbine blades, and industrial drying of paper, coatings, and textiles. A detailed understanding of the air flow and heat transfer of the jets is essential to make these processes more efficient. The Heat Flux Microsensor was tested in an industrial drying simulation to further study this phenomena.

A.1 Experimental Apparatus and Procedure

The Heat Flux Microsensor was mounted in a square aluminum plate, flush with the surface, and perpendicular to the flow from a jet tube plate. The jet tube plate

consisted of eleven circular tubes, each with a diameter of 1.59 cm (0.625 in) and a length of 15.2 cm (6.0 in). The tube plate was mounted at the exit of the plenum of a high-pressure blower pictured in Fig. 39. The plenum pressure was a constant 4.5 inches of water and was measured by a static pressure tap mounted in the wall of the plenum. A type-T thermocouple was embedded in the aluminum plate containing the sensor, also flush with the surface, to measure the temperature of the plate near the heat flux gage. Both the microsensor and the thermocouple data were recorded simultaneously by the HP dynamic signal analyzer. The microsensor signal was amplified by 1000.

Initially, the plate was preheated to approximately 80°C. After the blower was allowed to reach steady state, the flow from the jets was released onto the heated plate. The resulting cooling process is shown in Fig. 40. The top graph depicts the temperature decay of the thermocouple, and the bottom graph shows the simultaneous heat flux response.

Many other heat flux gages, precursors to the Heat Flux Microsensor, were tested by the aforementioned impingement procedure. These devices did not have feed-through leads making an ohmic connection; instead, they relied on metal clips, tightened to make contact with metal lead pads on the surface on the gage. The gage design is shown in Fig. 41. Because of the impinging nature of the testing, reliable contact of the clips was impossible. Initially, a tantalum-nichrome gage gave a very poor heat flux response. Next, a nickel-nichrome gage responded correctly but was not reliable because of the erratic contact of the clips. The connection problem has been solved by inserting conical

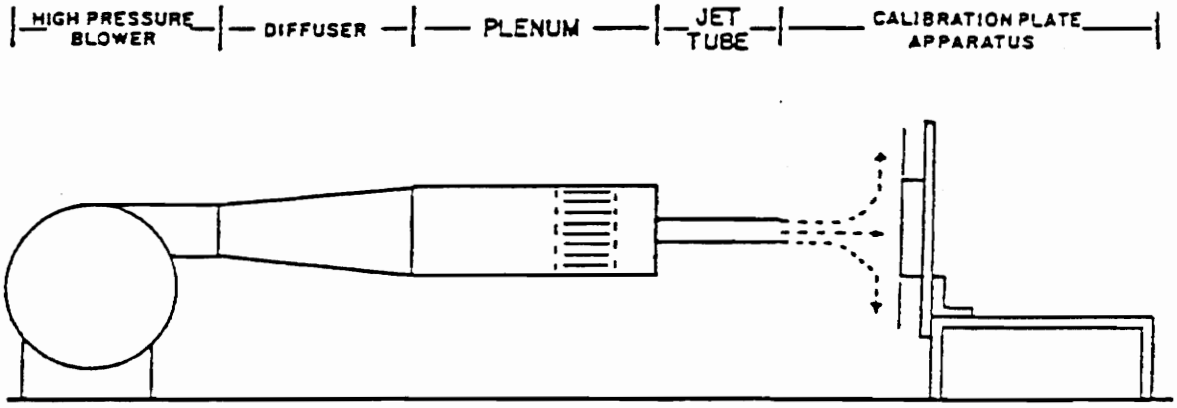

Fig. 40. High-pressure Blower for Jet Impingement Experiment

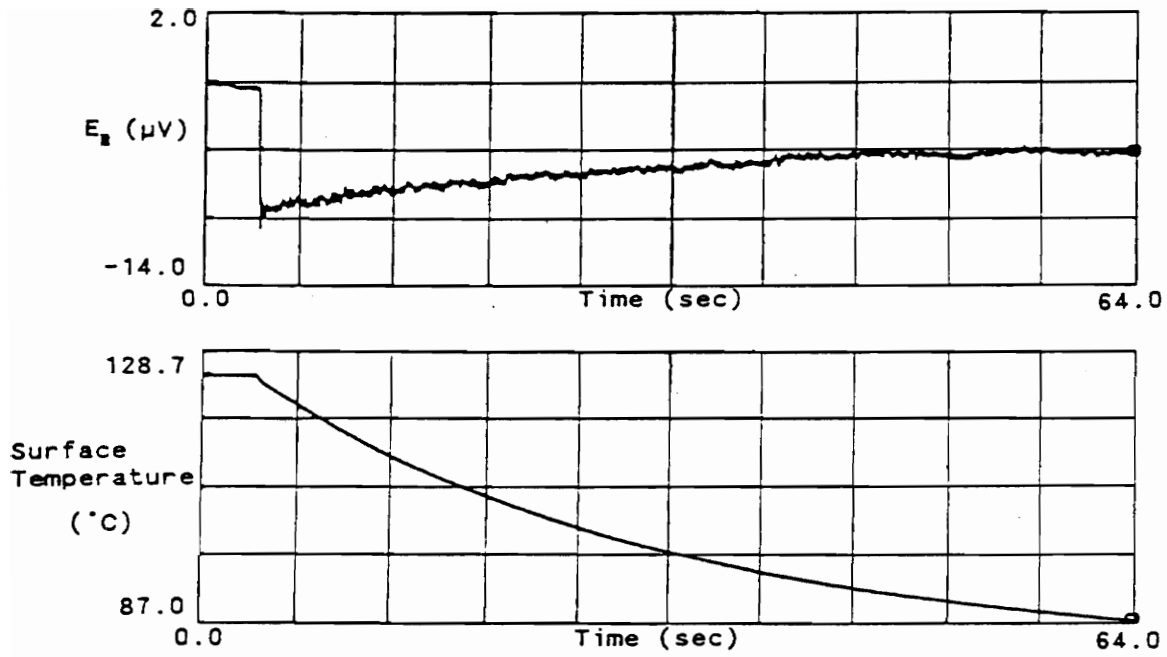

Fig. 41. Convection Curve for Heat Flux Microsensor

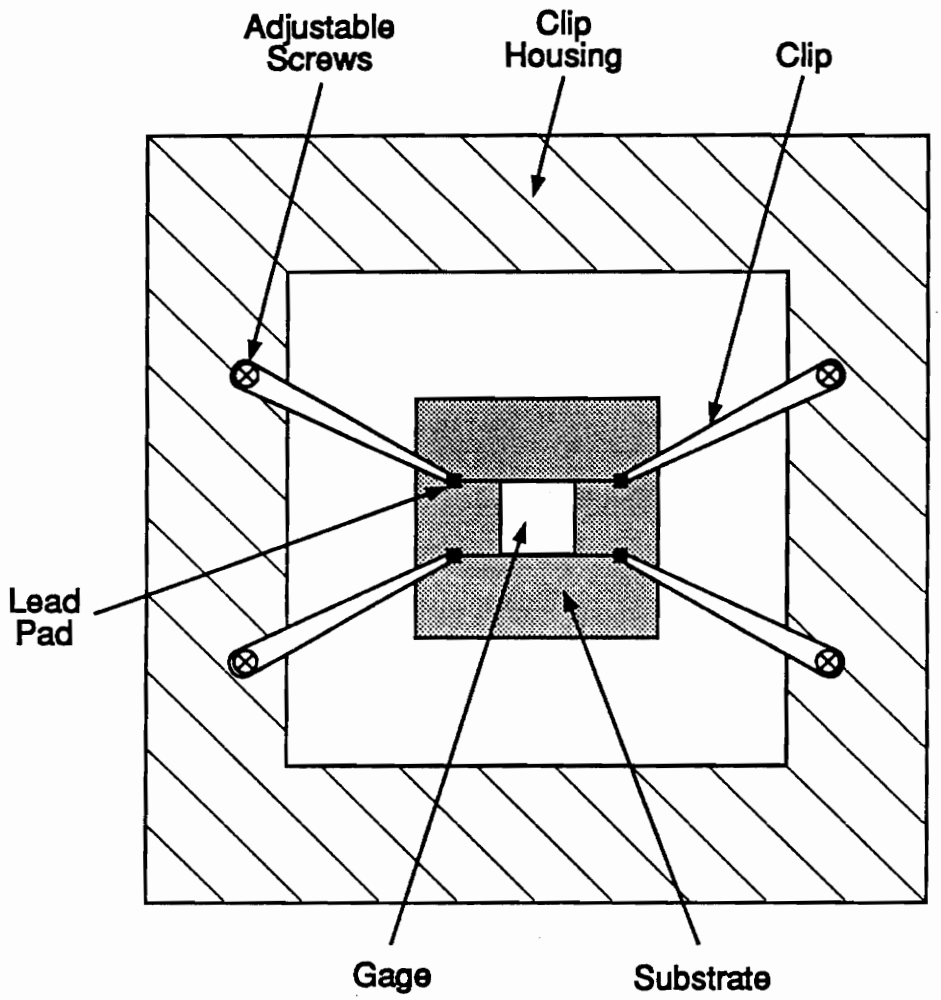

Fig. 42. Clip Design for Gage Operation

pins in the substrate on which the heat flux gage is sputtered. This improvement creates more surface area for contact between the pin and the sputtered pad. Furthermore, each pin is held in place by a pushnut which prevents movement of the pin.

A.2 Results

From these transient measurements, local heat transfer coefficients were calculated with the Heat Flux Microsensor. These results are comparable to published thermocouple values of 215 $W/(m^2 \cdot K)$ for the same conditions [25]. Since the coefficient can be calculated from either plot, results from the Heat Flux Microsensor can be easily checked against the thermocouple results of the change in stored thermal energy of the plate to validate data. From the results shown in Table 3, the calibration factor was off by a factor of approximately 2.5. Improved calibration tests were performed for the microsensor used in the current work, and the results were used in the presentation of this research.

Table 3. Local Heat Transfer Coefficients of Jet Impingement Experiment

Heat Transfer Coefficients*	h_x microsensor	h_x thermocouple
Test #1	107.78	276.06
Test #2	108.49	281.50
Test #3	118.38	278.40
Average h**	111.55±7.58	278.65±9.43

* **Coefficients have units of $W/(m^2 \cdot K)$**

** **Results are ± a 95% confidence interval.**

Appendix B

Hot-Wire Calibration

The single wire anemometer used for comparison in the preceding experiments was calibrated by using SAS software of SAS Institute, Inc. Data were taken with a pitot tube and the anemometer simultaneously, and velocity and voltage were recorded. The following appendix includes the output files and a brief explanation of the criteria for choice of the best calibration model. Plots of raw data and best calibration fit are included in Figs. 42 and 43.

B.1 Criteria for Best Calibration Model

The standard model-building problem involves an uncertainty of what terms to include in the model. In this particular calibration, a polynomial was tested up to x^7 individually and the lower orders were also tested in combinations. After analyzing each model, comparisons were made to choose the best model.

The three main factors in deciding the best model choice were the root mean square value, the R-square value, and the CP factor. The root mean square is an estimation of the standard deviation of the error term. It is calculated as the square root of the mean square error. The smaller the root mean square value, the better the prediction. The R-square value is a measure between 0 and 1 that indicates the portion of the variance that is attributed to the fit of the model, rather than the residual error. It is calculated by dividing the sum of the squares of the model by the total sum of the squares. Obviously, a number close to 1 is preferred. The CP factor balances the effects of underfitting and overfitting [26]. It is calculated by dividing the sum of the squares of the error of the model by the mean square error minus the number of independent variables minus two times the number of parameters. A small CP factor is a good indication of the best-fitting regression model.

B.2 Results

By examination of these factors it was determined that the x^6 model was the best choice. A calibration curve for this model is included in the following SAS output and is labeled Fig. 43. For this model other information was included such as the F value and the T test value for the model itself, and the residual error values for each data point in the model. The F value is the ratio of variances. PROB>F is the probability that the F value was valid by chance. The T test value tells how significant each variable is to the

fit of the model. PROB > T similarly validates the T test.

The calibration equation for the hot-wire voltage is:

$$V=0.3446+0.2132v^{6}$$

MODEL SELECTION

10:30 Thursday, April 4, 1991

N = 20 Regression Models for Dependent Variable: Y

Number in Model	R-square	C(p)	MSE	Variables in Model
1	0.99715168	33.13931	0.210232	X6
1	0.99631338	47.60162	0.272105	X5
1	0.99289809	106.52240	0.524185	X7
1	0.98825174	186.68122	0.867126	X4
1	0.98526386	238.22821	1.087658	X8
1	0.97066927	490.01445	2.164870	X3
1	0.94170346	989.73341	4.302805	X2
1	0.90083246	1695	7.319450	X
2	0.99802922	19.99997	0.154018	X X7
2	0.99798509	20.76128	0.157466	X X8
2	0.99794321	21.48378	0.160739	X2 X8
2	0.99792165	21.85569	0.162424	X2 X7
2	0.99786276	22.87168	0.167026	X3 X8
2	0.99781096	23.76529	0.171074	X3 X7
2	0.99776552	24.54935	0.174626	X X6
2	0.99775416	24.74521	0.175513	X4 X8
2	0.99770271	25.63299	0.179535	X4 X7
2	0.99770048	25.67136	0.179709	X2 X6
2	0.99764445	26.63799	0.184088	X3 X6
2	0.99762732	26.93347	0.185426	X5 X8
2	0.99760083	27.39050	0.187496	X5 X7
2	0.99759782	27.44239	0.187731	X4 X6
2	0.99756015	28.09238	0.190676	X5 X6
2	0.99750751	29.00046	0.194789	X6 X7
2	0.99749013	29.30029	0.196148	X6 X8
2	0.99742970	30.34295	0.200871	X4 X5
2	0.99734808	31.75100	0.207249	X7 X8
2	0.99733918	31.90450	0.207945	X3 X5
2	0.99723402	33.71873	0.216163	X2 X5
2	0.99711837	35.71391	0.225201	X X5
2	0.99687162	39.97094	0.244485	X3 X4
2	0.99647530	46.80828	0.275458	X2 X4
2	0.99600748	54.87911	0.312018	X X4
2	0.99538259	65.65962	0.360853	X2 X3
2	0.99435789	83.33779	0.440934	X X3
2	0.99211616	122.01221	0.616127	X X2
3	0.99875306	9.51226	0.103540	X X2 X3
3	0.99862488	11.72365	0.114183	X X2 X4
3	0.99853002	13.36010	0.122060	X X3 X4
3	0.99848123	14.20186	0.126111	X X2 X5
3	0.99844578	14.81342	0.129055	X2 X3 X4
3	0.99840271	15.55653	0.132631	X X3 X5
3	0.99832691	16.86427	0.138926	X2 X3 X5
3	0.99832449	16.90589	0.139126	X X2 X6
3	0.99832163	16.95520	0.139363	X X4 X5
3	0.99826796	17.88125	0.143820	X X3 X6
3	0.99824642	18.25282	0.145609	X2 X4 X5
3	0.99821232	18.84109	0.148440	X X4 X6
3	0.99820369	18.99002	0.149157	X2 X3 X6

MODEL SELECTION
10:30 Thursday, April 4, 1991

Number in Model	R-square	C(p)	MSE	Variables in Model
3	0.99816990	19.57291	0.151962	X3 X4 X5
3	0.99815890	19.76273	0.152876	X X5 X6
3	0.99815797	19.77875	0.152953	X X2 X7
3	0.99814449	20.01137	0.154073	X2 X4 X6
3	0.99812861	20.28529	0.155391	X X3 X7
3	0.99810259	20.73417	0.157552	X X4 X7
3	0.99808806	20.98488	0.158758	X2 X5 X6
3	0.99808052	21.11495	0.159384	X X5 X7
3	0.99807872	21.14595	0.159533	X2 X3 X7
3	0.99807728	21.17073	0.159653	X3 X4 X6
3	0.99806268	21.42273	0.160866	X X6 X7
3	0.99804386	21.74738	0.162428	X2 X4 X7
3	0.99803935	21.82514	0.162802	X X7 X8
3	0.99802108	22.14045	0.164320	X X6 X8
3	0.99801847	22.18544	0.164537	X3 X5 X6
3	0.99801338	22.27328	0.164959	X2 X5 X7
3	0.99800585	22.40308	0.165584	X X5 X8
3	0.99799445	22.59977	0.166531	X X4 X8
3	0.99798771	22.71611	0.167091	X2 X6 X7
3	0.99798758	22.71833	0.167101	X3 X4 X7
3	0.99798744	22.72070	0.167113	X X3 X8
3	0.99798509	22.76128	0.167308	X X2 X8
3	0.99795440	23.29074	0.169856	X2 X3 X8
3	0.99795219	23.32894	0.170040	X4 X5 X6
3	0.99795078	23.35321	0.170157	X2 X7 X8
3	0.99794878	23.38770	0.170323	X3 X5 X7
3	0.99794629	23.43061	0.170530	X2 X4 X8
3	0.99794495	23.45383	0.170641	X2 X6 X8
3	0.99794325	23.48314	0.170783	X2 X5 X8
3	0.99791543	23.96308	0.173092	X3 X6 X7
3	0.99790222	24.19098	0.174189	X3 X4 X8
3	0.99788868	24.42446	0.175313	X4 X5 X7
3	0.99788443	24.49795	0.175667	X3 X5 X8
3	0.99787226	24.70784	0.176677	X3 X6 X8
3	0.99786528	24.82822	0.177256	X3 X7 X8
3	0.99784805	25.12551	0.178687	X4 X6 X7
3	0.99783117	25.41664	0.180089	X4 X5 X8
3	0.99780524	25.86404	0.182242	X4 X6 X8
3	0.99778721	26.17518	0.183739	X5 X6 X7
3	0.99778552	26.20431	0.183880	X4 X7 X8
3	0.99774545	26.89552	0.187207	X5 X6 X8
3	0.99771341	27.44829	0.189867	X5 X7 X8
3	0.99765002	28.54191	0.195131	X6 X7 X8
4	0.99918044	4.13905	0.072589	X X2 X3 X4
4	0.99917214	4.28226	0.073324	X X2 X3 X5
4	0.99916729	4.36595	0.073754	X X2 X3 X7
4	0.99916627	4.38358	0.073844	X X2 X3 X8
4	0.99916491	4.40697	0.073964	X X2 X4 X5
4	0.99916286	4.44242	0.074146	X X2 X4 X7
4	0.99916215	4.45459	0.074209	X X2 X4 X8
4	0.99916192	4.45853	0.074229	X X2 X3 X6
4	0.99916157	4.46463	0.074260	X X2 X4 X6
4	0.99916143	4.46697	0.074272	X2 X3 X4 X5

MODEL SELECTION

10:30 Thursday, April 4, 1991

Number in Model	R-square	C(p)	MSE	Variables in Model
4	0.99916108	4.47314	0.074304	X X2 X5 X7
4	0.99916103	4.47392	0.074308	X X3 X4 X5
4	0.99916098	4.47488	0.074313	X X2 X5 X6
4	0.99916075	4.47868	0.074333	X X3 X4 X6
4	0.99915999	4.49188	0.074400	X X3 X4 X7
4	0.99915975	4.49607	0.074422	X X3 X5 X6
4	0.99915974	4.49621	0.074423	X X2 X5 X8
4	0.99915942	4.50177	0.074451	X2 X3 X4 X6
4	0.99915921	4.50538	0.074470	X X3 X4 X8
4	0.99915898	4.50922	0.074489	X X2 X6 X7
4	0.99915876	4.51309	0.074509	X2 X3 X4 X7
4	0.99915855	4.51663	0.074527	X X3 X5 X7
4	0.99915813	4.52391	0.074565	X X4 X5 X6
4	0.99915792	4.52761	0.074584	X2 X3 X5 X6
4	0.99915756	4.53378	0.074615	X X2 X6 X8
4	0.99915736	4.53732	0.074634	X2 X3 X4 X8
4	0.99915728	4.53866	0.074640	X X3 X5 X8
4	0.99915676	4.54755	0.074686	X X3 X6 X7
4	0.99915645	4.55296	0.074714	X X4 X5 X7
4	0.99915642	4.55340	0.074716	X2 X3 X5 X7
4	0.99915572	4.56559	0.074779	X2 X4 X5 X6
4	0.99915535	4.57200	0.074812	X X2 X7 X8
4	0.99915476	4.58214	0.074864	X X3 X6 X8
4	0.99915456	4.58557	0.074881	X X4 X5 X8
4	0.99915446	4.58731	0.074890	X2 X3 X5 X8
4	0.99915400	4.59525	0.074931	X X4 X6 X7
4	0.99915376	4.59937	0.074952	X2 X3 X6 X7
4	0.99915346	4.60458	0.074979	X2 X4 X5 X7
4	0.99915270	4.61771	0.075046	X3 X4 X5 X6
4	0.99915160	4.63656	0.075143	X X3 X7 X8
4	0.99915132	4.64146	0.075168	X X4 X6 X8
4	0.99915107	4.64584	0.075191	X2 X3 X6 X8
4	0.99915083	4.64997	0.075212	X2 X4 X5 X8
4	0.99915064	4.65314	0.075228	X X5 X6 X7
4	0.99915020	4.66079	0.075267	X2 X4 X6 X7
4	0.99914973	4.66893	0.075309	X3 X4 X5 X7
4	0.99914744	4.70837	0.075512	X X4 X7 X8
4	0.99914719	4.71264	0.075534	X X5 X6 X8
4	0.99914716	4.71323	0.075537	X2 X3 X7 X8
4	0.99914671	4.72096	0.075576	X2 X4 X6 X8
4	0.99914626	4.72870	0.075616	X3 X4 X5 X8
4	0.99914593	4.73442	0.075645	X2 X5 X6 X7
4	0.99914555	4.74096	0.075679	X3 X4 X6 X7
4	0.99914248	4.79393	0.075951	X X5 X7 X8
4	0.99914190	4.80402	0.076003	X2 X4 X7 X8
4	0.99914153	4.81027	0.076035	X2 X5 X6 X8
4	0.99914111	4.81753	0.076072	X3 X4 X6 X8
4	0.99914021	4.83310	0.076152	X3 X5 X6 X7
4	0.99913674	4.89298	0.076460	X X6 X7 X8
4	0.99913569	4.91109	0.076553	X2 X5 X7 X8
4	0.99913521	4.91937	0.076595	X3 X4 X7 X8
4	0.99913470	4.92817	0.076640	X3 X5 X6 X8
4	0.99913338	4.95093	0.076757	X4 X5 X6 X7
4	0.99912856	5.03411	0.077184	X2 X6 X7 X8

MODEL SELECTION

10:30 Thursday, April 4, 1991

Number in Model	R-square	C(p)	MSE	Variables in Model
4	0.99912753	5.05183	0.077275	X3 X5 X7 X8
4	0.99912658	5.06828	0.077360	X4 X5 X6 X8
4	0.99911876	5.20313	0.078052	X3 X6 X7 X8
4	0.99911788	5.21829	0.078130	X4 X5 X7 X8
4	0.99910721	5.40250	0.079075	X4 X6 X7 X8
4	0.99909379	5.63397	0.080264	X5 X6 X7 X8
5	0.99917099	6.30207	0.078671	X X2 X3 X7 X8
5	0.99916937	6.33003	0.078824	X X2 X3 X5 X8
5	0.99916754	6.36164	0.078998	X X2 X4 X5 X7
5	0.99916347	6.43177	0.079384	X X2 X4 X7 X8
5	0.99916324	6.43576	0.079406	X X2 X4 X5 X8
5	0.99916310	6.43815	0.079419	X2 X3 X4 X5 X7
5	0.99916239	6.45044	0.079487	X2 X3 X4 X5 X8
5	0.99916201	6.45696	0.079523	X X2 X3 X6 X8
5	0.99916196	6.45797	0.079528	X X2 X3 X6 X7
5	0.99916195	6.45805	0.079529	X X2 X3 X4 X6
5	0.99916193	6.45848	0.079531	X X2 X3 X5 X6
5	0.99916173	6.46190	0.079550	X X2 X4 X5 X6
5	0.99916160	6.46417	0.079562	X X2 X4 X6 X7
5	0.99916157	6.46460	0.079565	X X2 X4 X6 X8
5	0.99916135	6.46842	0.079586	X X3 X4 X5 X6
5	0.99916132	6.46887	0.079588	X X2 X5 X7 X8
5	0.99916125	6.47020	0.079595	X X2 X5 X6 X7
5	0.99916113	6.47213	0.079606	X X2 X5 X6 X8
5	0.99916107	6.47316	0.079612	X X3 X4 X5 X7
5	0.99916104	6.47371	0.079615	X X3 X4 X6 X7
5	0.99916104	6.47378	0.079615	X X3 X4 X5 X8
5	0.99916093	6.47571	0.079626	X X3 X4 X6 X8
5	0.99916079	6.47802	0.079638	X2 X3 X4 X5 X6
5	0.99916059	6.48149	0.079657	X X3 X5 X6 X7
5	0.99916048	6.48344	0.079668	X2 X3 X4 X7 X8
5	0.99916047	6.48358	0.079669	X X3 X4 X7 X8
5	0.99916038	6.48511	0.079677	X X3 X5 X6 X8
5	0.99916030	6.48656	0.079685	X X2 X6 X7 X8
5	0.99916030	6.48657	0.079685	X2 X3 X4 X6 X7
5	0.99916008	6.49027	0.079706	X2 X3 X4 X6 X8
5	0.99915993	6.49298	0.079721	X X4 X5 X6 X7
5	0.99915983	6.49467	0.079730	X X3 X5 X7 X8
5	0.99915974	6.49624	0.079739	X2 X3 X5 X6 X7
5	0.99915961	6.49837	0.079750	X X4 X5 X6 X8
5	0.99915942	6.50167	0.079768	X2 X3 X5 X6 X8
5	0.99915932	6.50347	0.079778	X X3 X6 X7 X8
5	0.99915917	6.50604	0.079792	X2 X3 X5 X7 X8
5	0.99915898	6.50930	0.079810	X X4 X5 X7 X8
5	0.99915895	6.50978	0.079813	X2 X4 X5 X6 X7
5	0.99915853	6.51712	0.079853	X2 X4 X5 X6 X8
5	0.99915831	6.52092	0.079874	X X4 X6 X7 X8
5	0.99915811	6.52429	0.079893	X2 X3 X6 X7 X8
5	0.99915794	6.52729	0.079909	X3 X4 X5 X6 X7
5	0.99915784	6.52889	0.079918	X2 X4 X5 X7 X8
5	0.99915739	6.53674	0.079961	X3 X4 X5 X6 X8
5	0.99915727	6.53877	0.079973	X X5 X6 X7 X8
5	0.99915695	6.54427	0.080003	X2 X4 X6 X7 X8

MODEL SELECTION

10:30 Thursday, April 4, 1991

Number in Model	R-square	C(p)	MSE	Variables in Model
5	0.99915666	6.54929	0.080030	X3 X4 X5 X7 X8
5	0.99915576	6.56481	0.080116	X2 X5 X6 X7 X8
5	0.99915553	6.56885	0.080138	X3 X4 X6 X7 X8
5	0.99915417	6.59230	0.080267	X3 X5 X6 X7 X8
5	0.99915250	6.62110	0.080425	X4 X5 X6 X7 X8
6	0.99924705	6.98994	0.076949	X X2 X4 X6 X7 X8
6	0.99924647	7.00000	0.077009	X X2 X3 X6 X7 X8
6	0.99924498	7.02559	0.077161	X X2 X3 X5 X6 X8

MODEL SELECTION
10:52 Thursday, April 4, 1991

Model: MODEL1
Dependent Variable: Y

Analysis of Variance

Source	DF	Sum of Squares	Mean Square	F Value	Prob>F
Model	1	1196.81155	1196.81155	163.512	0.0001
Error	18	131.74914	7.31940		
C Total	19	1328.56070			

Root MSE	2.70544	R-square	0.9008
Dep Mean	16.08550	Adj R-sq	0.8953
C.V.	16.81911		

Parameter Estimates

Variable	DF	Parameter Estimate	Standard Error	T for H0: Parameter=0	Prob > |T|
INTERCEP	1	-27.312729	3.44737673	-7.923	0.0001
X	1	22.273206	1.74183695	12.787	0.0001

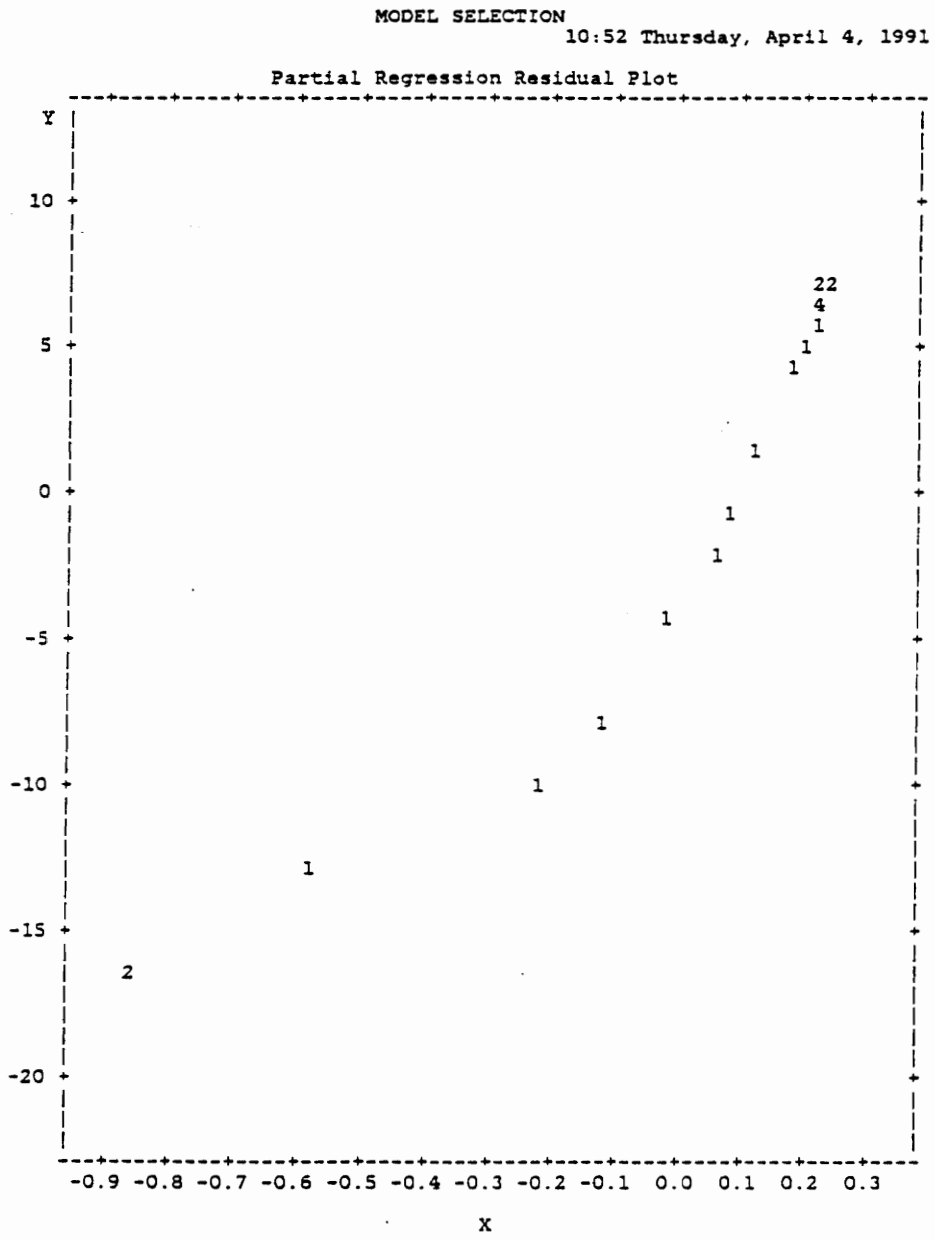

Fig. 43. Unlinearized Hot-wire Data

MODEL SELECTION
10:52 Thursday, April 4, 1991

Model: MODEL1
Dependent Variable: Y

Analysis of Variance

Source	DF	Sum of Squares	Mean Square	F Value	Prob>F
Model	1	1324.77653	1324.77653	6301.512	0.0001
Error	18	3.78417	0.21023		
C Total	19	1328.56070			

Root MSE	0.45851	R-square	0.9972
Dep Mean	16.08550	Adj R-sq	0.9970
C.V.	2.85046		

Parameter Estimates

Variable	DF	Parameter Estimate	Standard Error	T for H0: Parameter=0	Prob > |T|
INTERCEP	1	0.344639	0.22322961	1.544	0.1400
X6	1	0.213227	0.00268608	79.382	0.0001

Variable	DF	Variance Inflation
INTERCEP	1	0.00000000
X6	1	1.00000000

MODEL SELECTION

10:52 Thursday, April 4, 1991

Obs	Dep Var Y	Predict Value	Std Err Predict	Residual	Std Err Residual	Student Residual
1	0	0.7102	0.219	-0.7102	0.403	-1.763
2	23.2200	23.5479	0.139	-0.3279	0.437	-0.751
3	20.2700	20.0891	0.114	0.1809	0.444	0.407
4	17.5500	17.1197	0.103	0.4303	0.447	0.963
5	15.4800	15.1783	0.103	0.3017	0.447	0.675
6	13.7200	13.9911	0.106	-0.2711	0.446	-0.608
7	11.7000	11.3647	0.119	0.3353	0.443	0.757
8	8.2700	8.1710	0.143	0.0990	0.436	0.227
9	5.8500	5.9626	0.164	-0.1126	0.428	-0.263
10	2.9300	1.7606	0.208	1.1694	0.409	2.860
11	21.3000	21.2296	0.121	0.0704	0.442	0.159
12	21.6900	21.9398	0.126	-0.2498	0.441	-0.567
13	22.2800	22.4856	0.130	-0.2056	0.440	-0.468
14	22.6600	22.9804	0.134	-0.3204	0.438	-0.731
15	22.8500	23.1055	0.135	-0.2555	0.438	-0.583
16	22.9400	23.1683	0.136	-0.2283	0.438	-0.521
17	0	0.7082	0.219	-0.7082	0.403	-1.758
18	22.8500	22.9804	0.134	-0.1304	0.438	-0.297
19	23.0300	22.6085	0.131	0.4215	0.439	0.960
20	23.1200	22.6085	0.131	0.5115	0.439	1.165

Obs	-2-1-0 1 2	Cook's D	Rstudent	Hat Diag H	Cov Ratio	Dffits
1	***	0.460	-1.8841	0.2284	0.9944	-1.0252
2	*	0.029	-0.7412	0.0920	1.1587	-0.2360
3		0.005	0.3977	0.0621	1.1734	0.1023
4	*	0.025	0.9613	0.0508	1.0625	0.2224
5	*	0.012	0.6647	0.0506	1.1218	0.1535
6	*	0.010	-0.5968	0.0533	1.1361	-0.1416
7	*	0.021	0.7476	0.0668	1.1261	0.2001
8		0.003	0.2211	0.0973	1.2348	0.0726
9		0.005	-0.2559	0.1274	1.2749	-0.0978
10	*****	1.054	3.7632	0.2049	0.4196	1.9103
11		0.001	0.1549	0.0700	1.2021	0.0425
12	*	0.013	-0.5558	0.0759	1.1702	-0.1593
13		0.010	-0.4574	0.0809	1.1903	-0.1357
14	*	0.025	-0.7210	0.0859	1.1547	-0.2210
15	*	0.016	-0.5722	0.0872	1.1822	-0.1769
16	*	0.013	-0.5104	0.0879	1.1923	-0.1584
17	***	0.458	-1.8778	0.2285	0.9968	-1.0219
18		0.004	-0.2897	0.0859	1.2144	-0.0888
19	*	0.041	0.9574	0.0821	1.0996	0.2864
20	**	0.061	1.1769	0.0821	1.0443	0.3520

Obs	INTERCEP Dfbetas	X6 Dfbetas
1	-1.0252	0.9061
2	0.0618	-0.1595
3	0.0020	0.0452
4	0.0764	0.0280
5	0.0852	-0.0170
6	-0.0943	0.0353

Obs	INTERCEP Dfbetas	X6 Dfbetas
7	0.1686	-0.1004
8	0.0689	-0.0506
9	-0.0958	0.0762
10	1.9089	-1.6610
11	-0.0037	0.0227
12	0.0232	-0.0930
13	0.0255	-0.0839
14	0.0494	-0.1429
15	0.0411	-0.1155
16	0.0375	-0.1040
17	-1.0219	0.9032
18	0.0199	-0.0574
19	-0.0565	0.1791
20	-0.0694	0.2201

Sum of Residuals	0
Sum of Squared Residuals	3.7842
Predicted Resid SS (Press)	5.5012

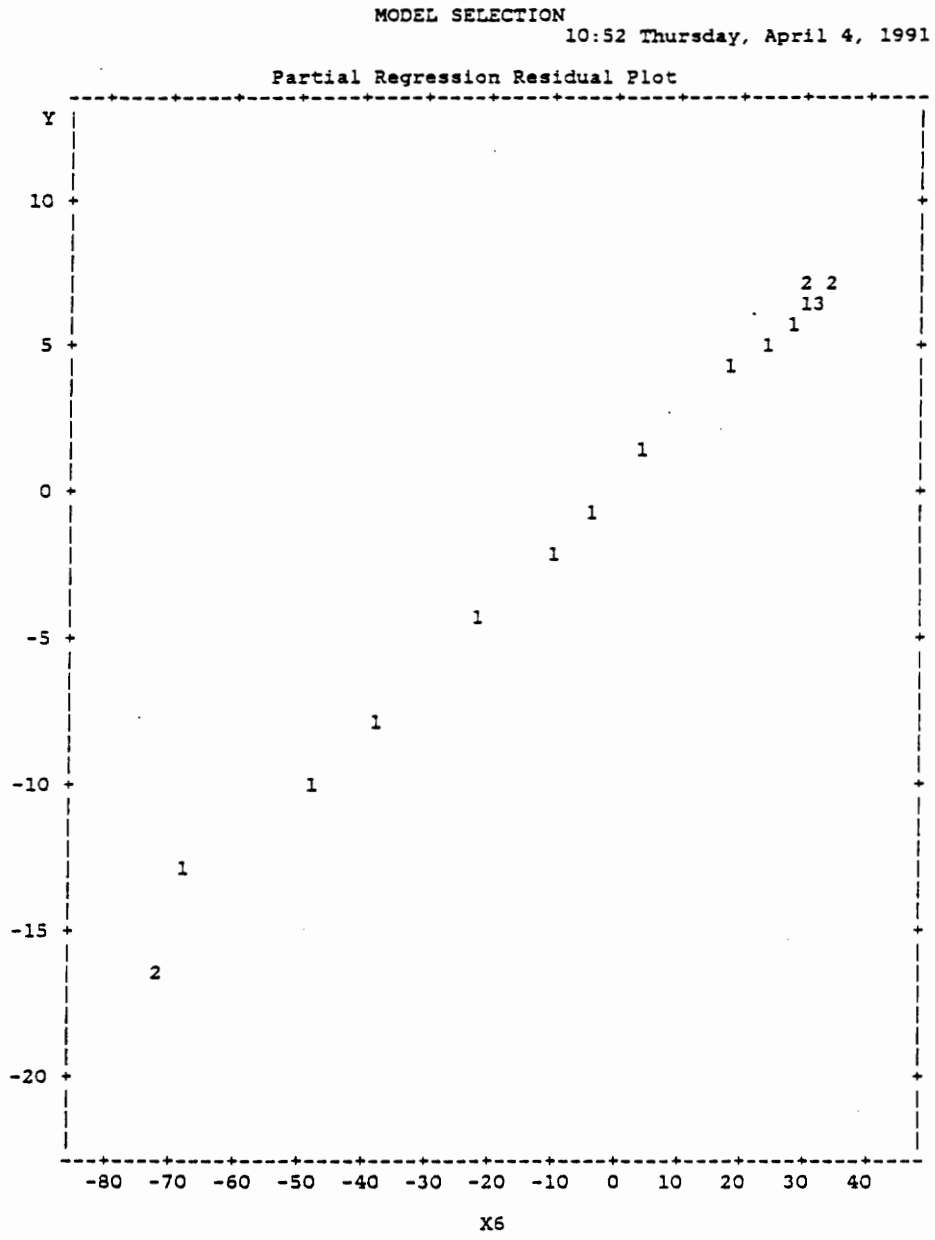

Fig. 44. Linearized Hot-wire Calibration Curve

Appendix C

Temperature Sensor Calibration

The RTS temperature sensor on the Heat Flux Microsensor was calibrated with a standard type-K thermocouple. First, the circuit was zeroed and the room temperature RTS resistance was measured. The RTS and the thermocouple were then placed in close thermal contact with each other in a temperature-controlled oven with low thermal gradients. Output measurements were taken for a series of steady-state temperatures up to 200°C. The results of this calibration, shown in Fig. 44, indicate that there is a linear relationship between voltage and temperature.

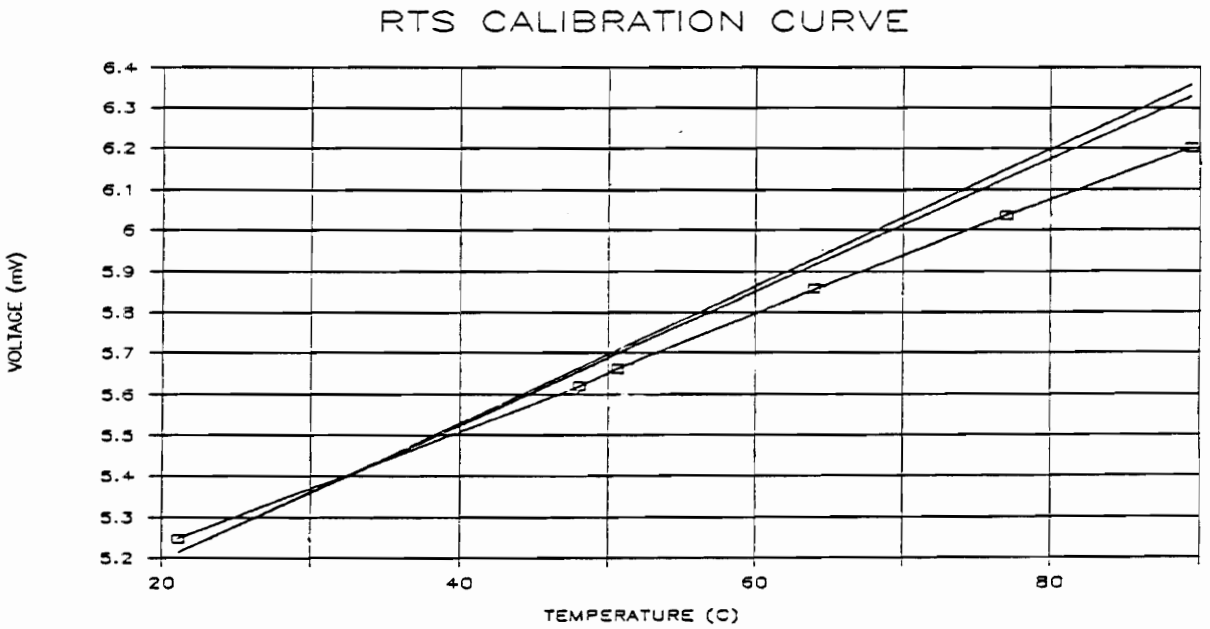

Fig. 45. Calibration Curve for RTS Temperature Sensor

Appendix D

Accelerometer Data

An ICP 302A accelerometer was used in this experiment to determine which frequencies in the response were due to vibrations of the apparatus and the wind tunnel rather than due to the vortex system itself. Comparisons were made to the Heat Flux Microsensor and the hot-wire anemometer with and without the airfoil shaped body in the flow path. The accelerometer output was recorded by the signal analyzer.

The results of these tests were significant. The anemometer did not seem to be affected by any apparatus or tunnel vibration. Coherence for both of these cases was less than 0.1. On the other hand, tunnel vibrations greatly contributed to the response seen by the Heat Flux Microsensor. Both the motor speed of 29 Hz and the shaft speed of 17 Hz are present in the power spectrum tests. The shaft speed had the higher coherence of almost 0.3, probably due to a fan imbalance. The following plots confirmed these results.

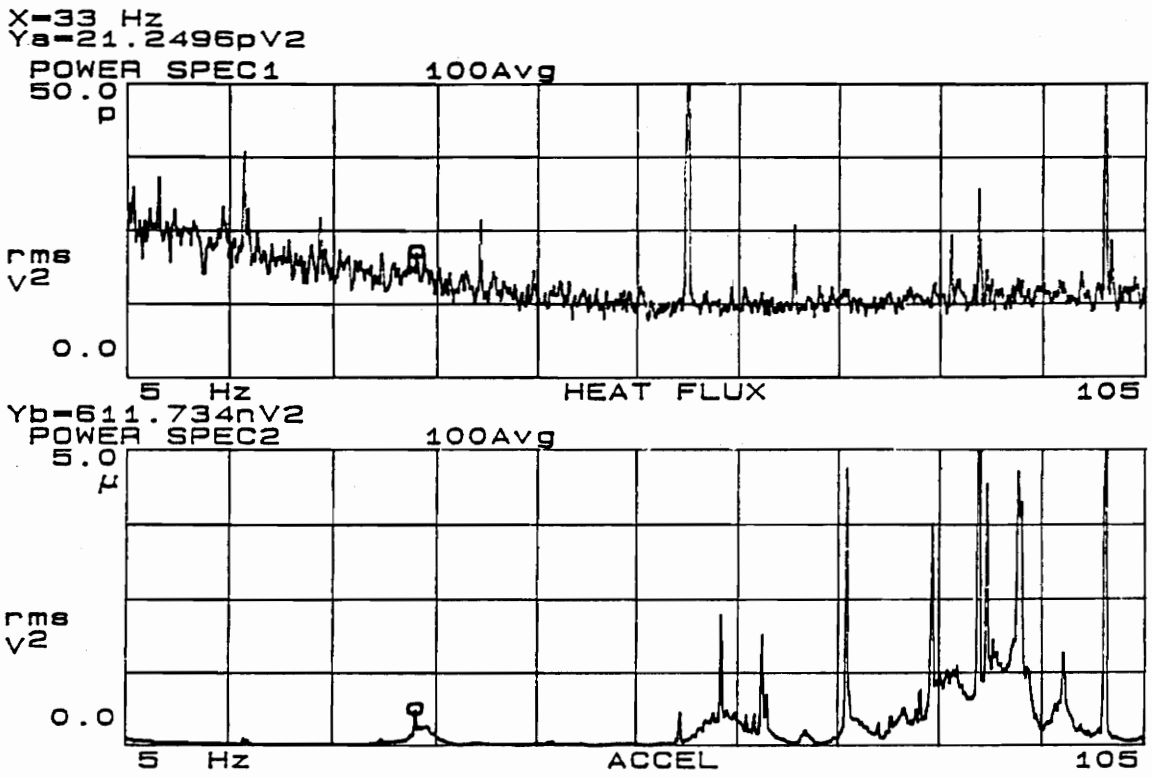

Fig. 46. Power Spectra of Heat Flux Gage and Accelerometer with Airfoil

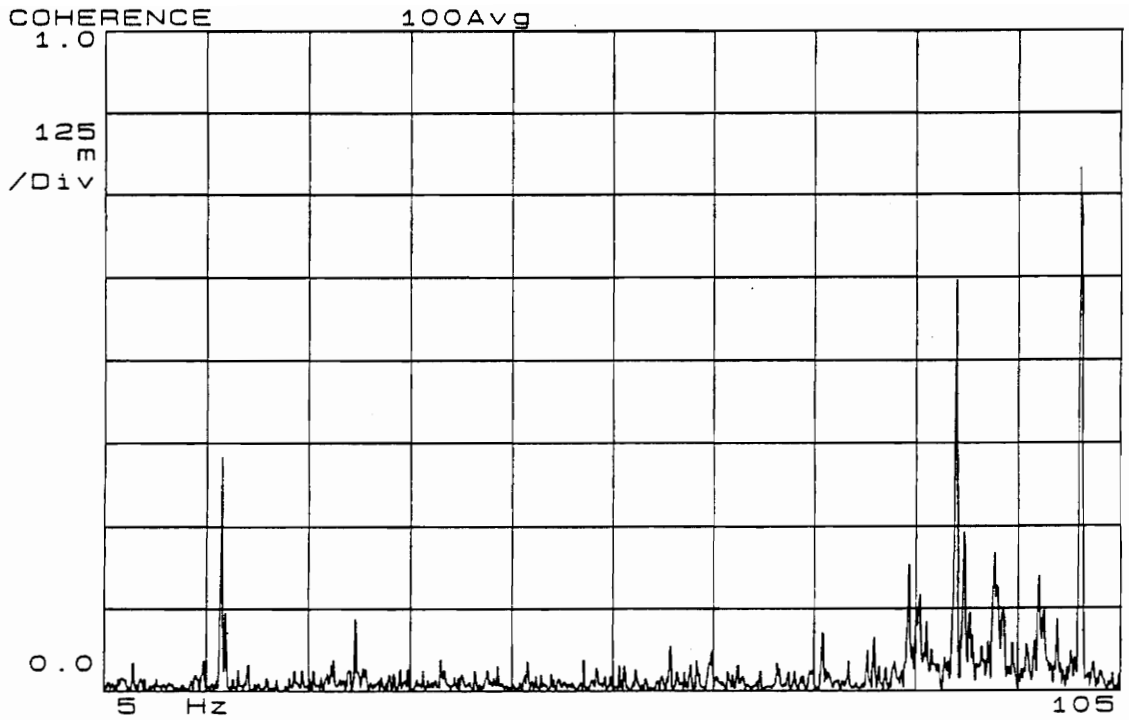

Fig. 47. Coherence of Heat Flux Gage and Accelerometer with Airfoil

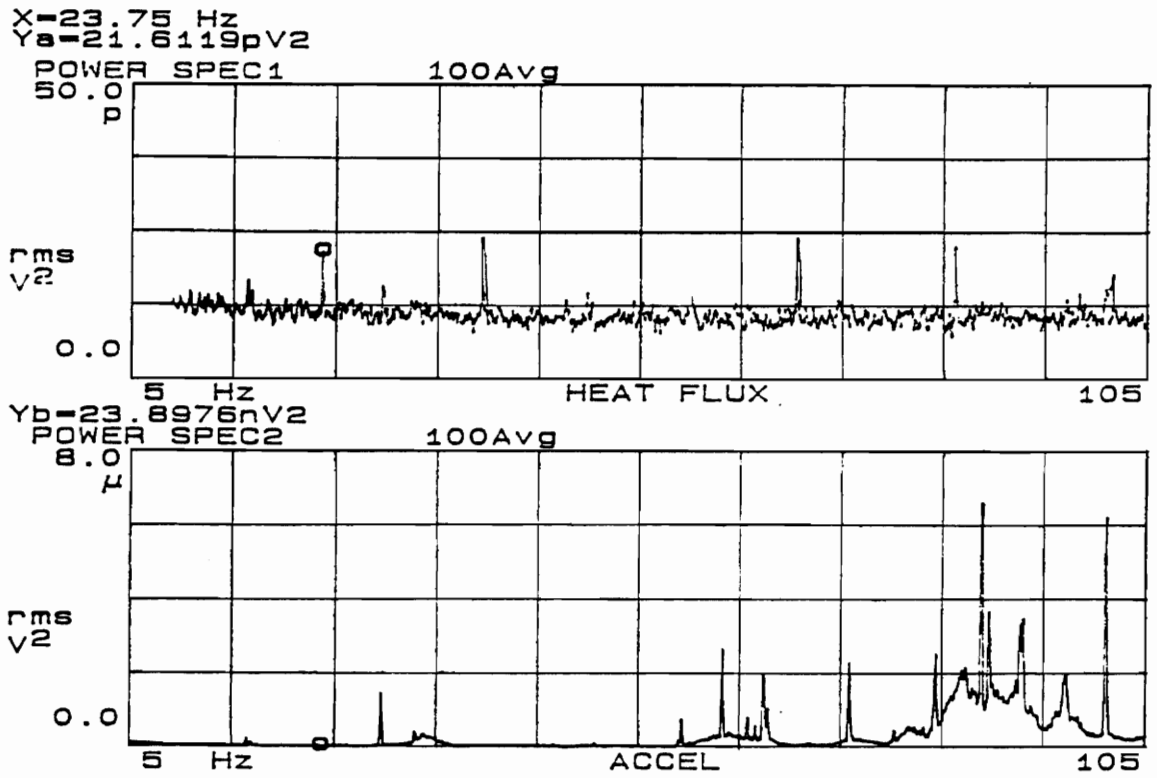

Fig. 48. Power Spectra of Heat Flux Gage and Accelerometer without Airfoil

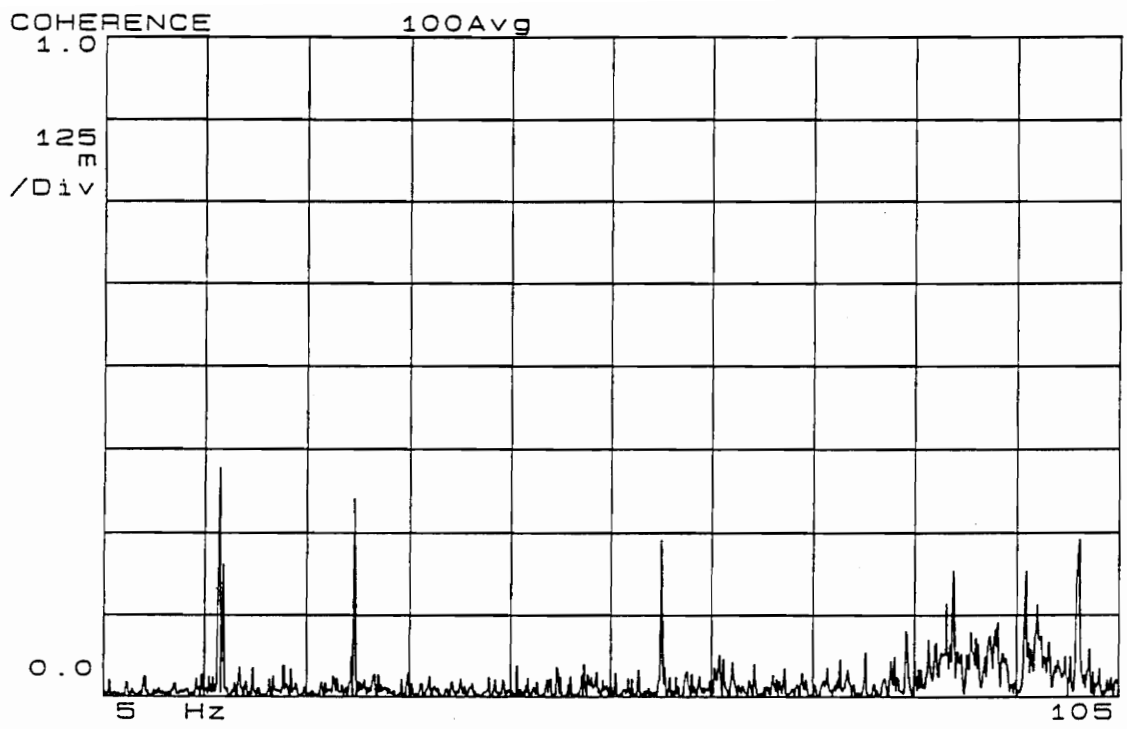

Fig. 49. Coherence of Heat Flux Gage and Accelerometer without Airfoil

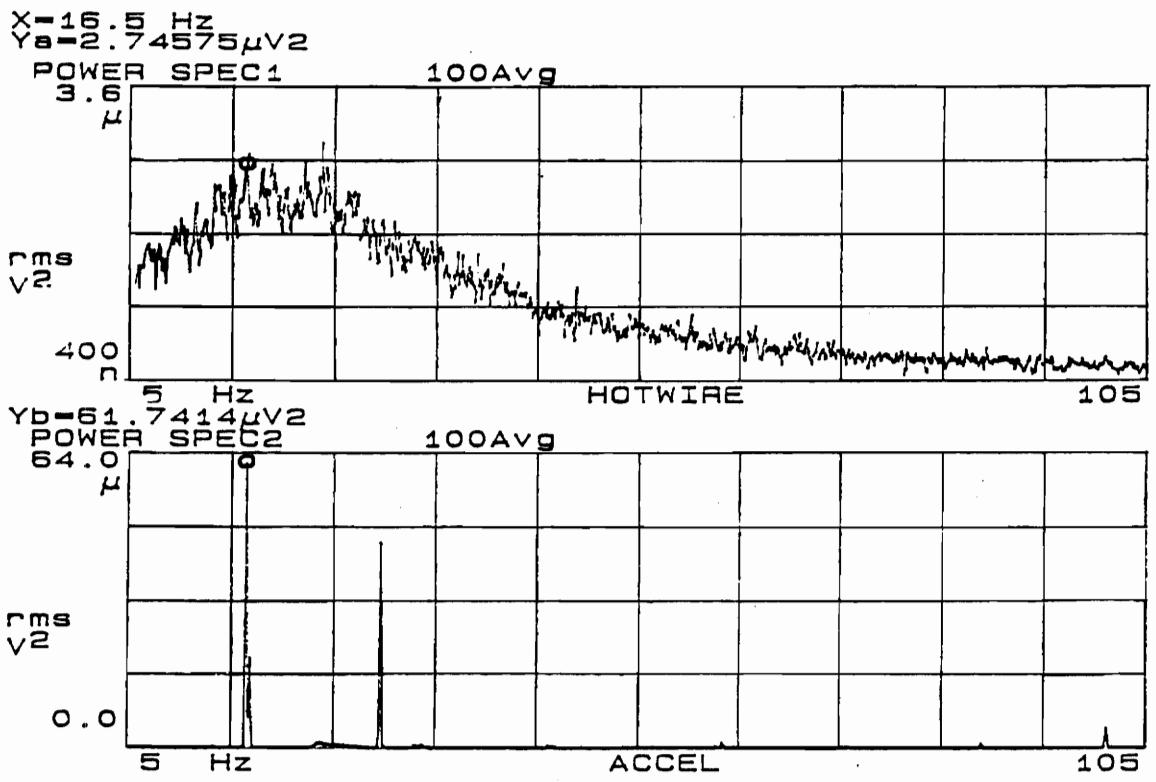

Fig. 50. Power Spectra of Anemometer and Accelerometer with Airfoil

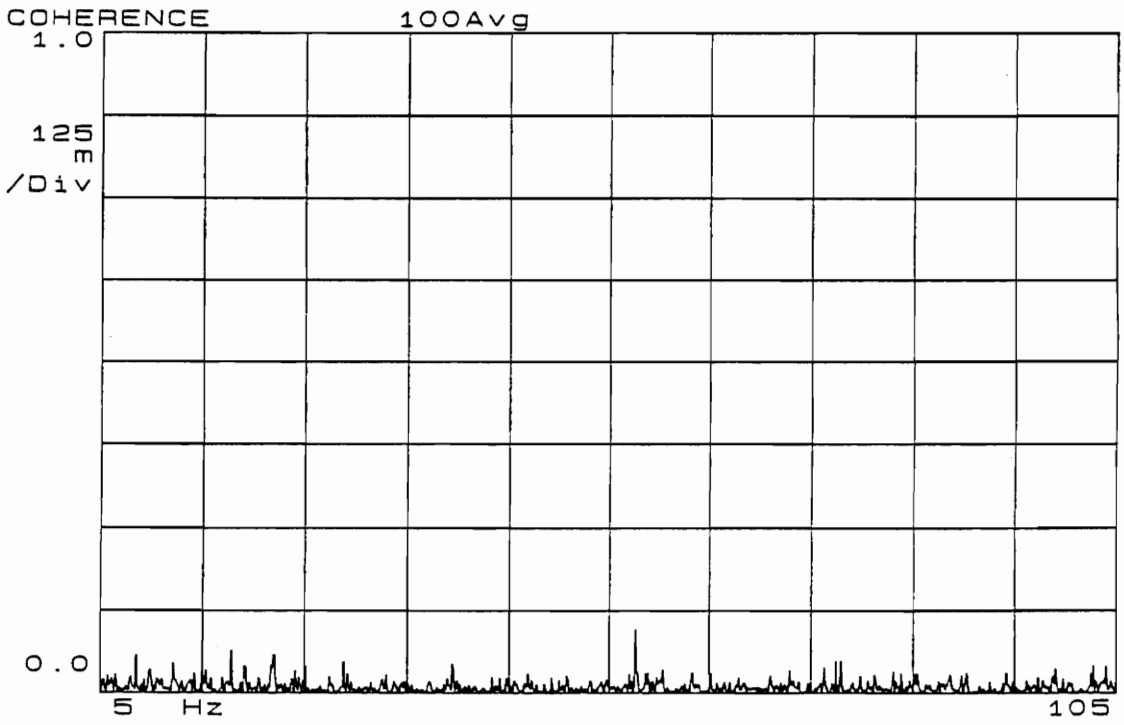

Fig. 51. Coherence of Anemometer and Accelerometer with Airfoil

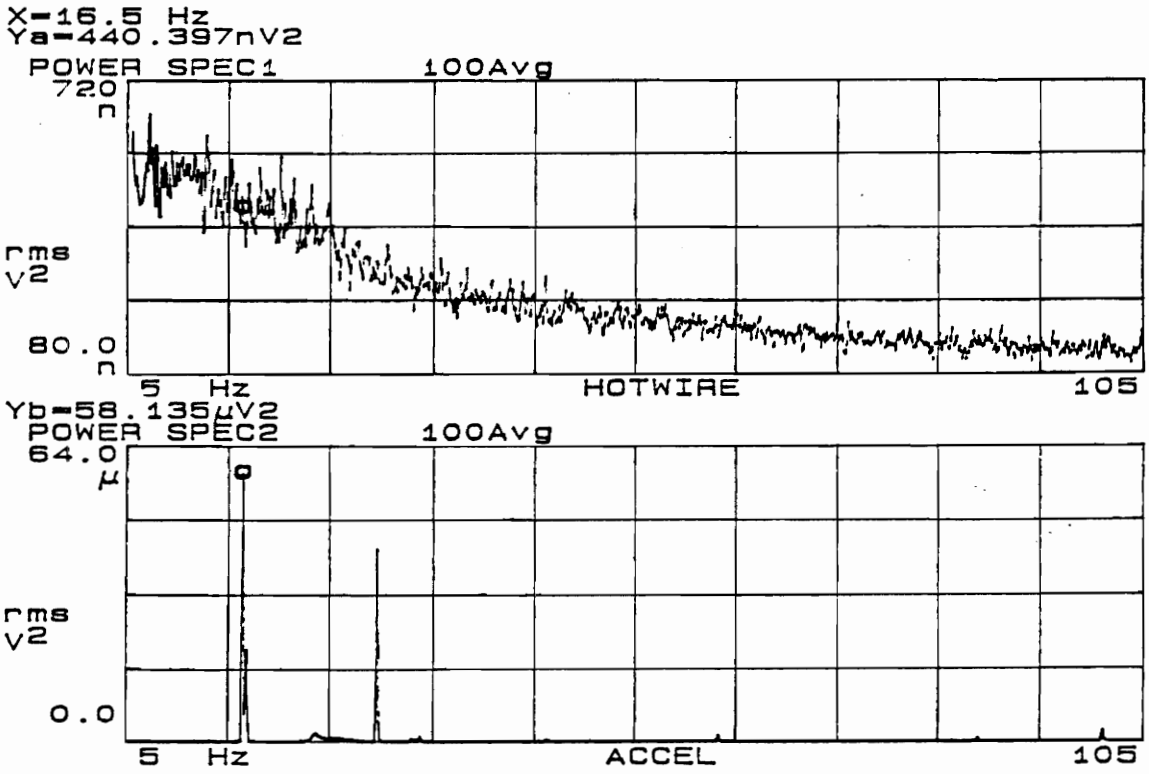

Fig. 52. Power Spectra of Anemometer and Accelerometer without Airfoil

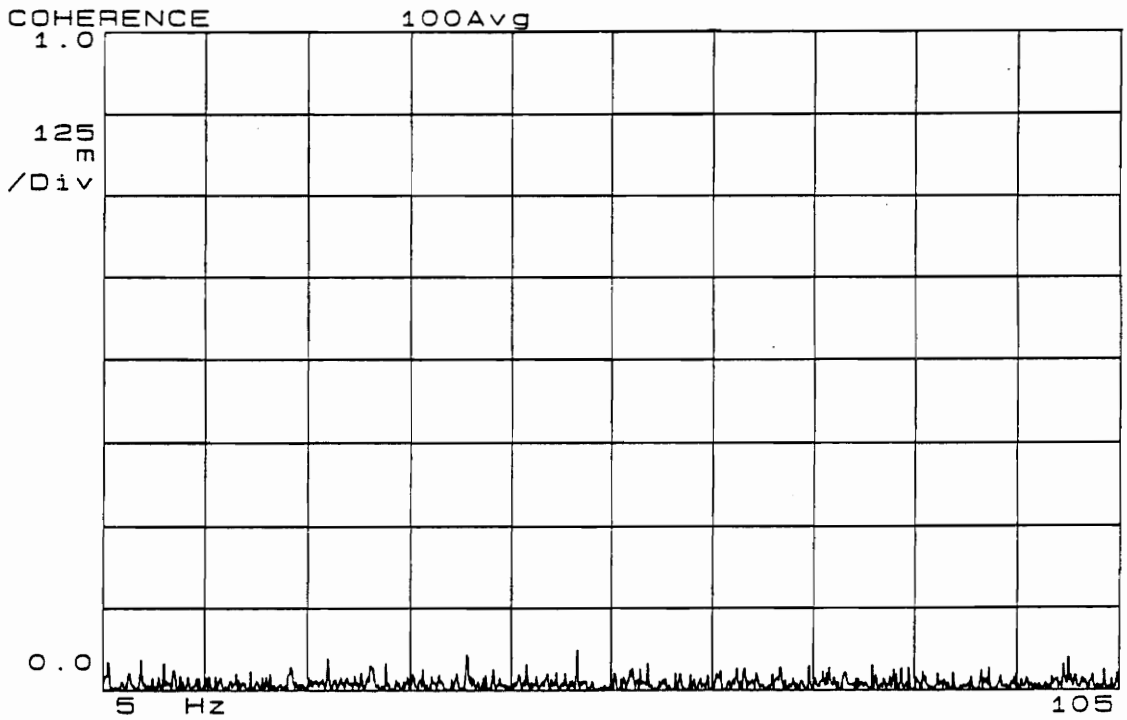

Fig. 53. Coherence of Anemometer and Accelerometer without Airfoil

Appendix E

Data Processing Codes

The following Matlab code was used to process data taken from the HP signal analyzer. Matlab calculated the values for Tables 1 and 2, excluding the Stanton number. The turbulence level heat flux plots in Figs. 26, 30, 34, and 38 were also created in Matlab.

```
clg
clear c1
eval(['load ',namet])
ubar = mean(c1)
ubarabs = abs(ubar)
qbar = ubarabs*(1358.696)*1e3
deltaT = input('What is delta T ?')
hbar = qbar/deltaT
Q_f = abs((std(c1)*sqrt(2)))*1358.696*1e3
qdivq = Q_f/qbar
H_fl = Q_f/deltaT
uprimeabs = abs(c1-ubar);
usquare = sum(uprimeabs.*uprimeabs)
usquave = usquare/(length(c1)-1)
squave = sqrt(usquave)
Tu = squave/ubarabs;
Tut(i+2) = std(c1)/ubarabs;

clear c1
eval(['load ',namef])
under = sum(c1);
Tup(i+2) = sqrt(under)/ubarabs;


clg
clear c2
eval(['load ',namet])
ubar = mean(c2);
vbar = .344639+.213227*(ubar)^6
clin = .344639+.213227*(c2).^6;
vdivv = 2*std(clin)*sqrt(2)/vbar
uprime = clin-vbar;
usquare = sum(uprime.*uprime)
usquave = usquare/(length(c2)-1)
squave = sqrt(usquave)
Tu(i+1) = squave/vbar;
Tut(i+1) = std(clin)/vbar;

clear c2
clear clin

%eval(['load ',namef])
%under = sum(c2);
%Tup(i+1) = sqrt(under)/ubar;
```

```
temp
diary stace4
for i = 0:2:24,
       i
       2*i+1
       namet = fils(2*i+2,:)
       namef = fils(2*i+1,:)
       chan1
       i
       2*i+3
       namet = fils(2*i+4,:)
       namef = fils(2*i+3,:)
       chan2
end
Tut
Tup
```

```
i =     0
ans =     1
namet =p19f226
namef =p19f225
ubar =   -0.0064
ubarabs =    0.0064
qbar =  8.6951e+003
 What is delta T ?
deltaT =    45
hbar =  193.2245
Q_f =  3.7680e+003
qdivq =    0.4334
H_fl =   83.7341
usquare =    0.0079
usquave =  3.8455e-006
squave =    0.0020

i =     0
ans =     3
namet =p19h226
namef =p19h225
vbar =    3.8752
vdivv =    0.4946
usquare =  945.8959
usquave =    0.4621
squave =    0.6798

i =     2
ans =     5
namet =p1hf226
namef =p1ft225
ubar =   -0.0063
ubarabs =    0.0063
qbar =  8.5685e+003
 What is delta T ?
deltaT =    40
hbar =  214.2131
Q_f =  3.6575e+003
qdivq =    0.4269
H_fl =   91.4386
usquare =    0.0074
usquave =  3.6233e-006
squave =    0.0019

i =     2
ans =     7
namet =p1hh226
namef =p1ht225
vbar =   11.7899
vdivv =    0.4389
usquare =  6.8798e+003
usquave =    3.3609
squave =    1.8333

i =     4
ans =     9
namet =hp2f34
namef =hp2p34
ubar =   -0.0098
ubarabs =    0.0098
qbar =  1.3255e+004
 What is delta T ?
deltaT =    56
hbar =  236.6946
Q_f =  2.6703e+003
qdivq =    0.2015
H_fl =   47.6846
usquare =    0.0040
usquave =  1.9313e-006
squave =    0.0014

i =     4
ans =    11
namet =hp2h34
namef =hp2s34
vbar =    3.5795
vdivv =    0.4074
usquare =  546.2595
usquave =    0.2669
squave =    0.5166

i =     6
ans =    13
namet =fp2h34
namef =pp2h34
ubar =   -0.0091
ubarabs =    0.0091
qbar =  1.2423e+004
 What is delta T ?
deltaT =    55
hbar =  225.8717
Q_f =  3.2712e+003
qdivq =    0.2633
H_fl =   59.4773
usquare =    0.0059
usquave =  2.8984e-006
squave =    0.0017

i =     6
ans =    15
namet =hhp2h34
namef =sp2h34
vbar =   12.8469
vdivv =    0.3684
usquare =  5.7507e+003
usquave =    2.8093
squave =    1.6761

i =     8
ans =    17
namet =p3h9f37
namef =p3h9p37
ubar =   -0.0067
```

```
ubarabs =     0.0067
qbar =  9.1335e+003
 What is delta T ?
deltaT =     56
hbar =  163.0980
Q_f =  3.0819e+003
qdivq =     0.3374
H_fl =   55.0336
usquare =     0.0053
usquave =  2.5725e-006
squave =     0.0016

i =      8
ans =     19
namet =p3h9t37
namef =p3h9s37
vbar =     5.5667
vdivv =     0.6200
usquare =  3.0787e+003
usquave =     1.5040
squave =     1.2264

i =     10
ans =     21
namet =p3hf37
namef =p3hp37
ubar =    -0.0073
ubarabs =     0.0073
qbar =  9.9278e+003
 What is delta T ?
deltaT =     54
hbar =  183.8472
Q_f =  2.9604e+003
qdivq =     0.2982
H_fl =   54.8227
usquare =     0.0049
usquave =  2.3737e-006
squave =     0.0015

i =     10
ans =     23
namet =p3ht37
namef =p3hs37
vbar =     7.8049
vdivv =     0.6223
usquare =  6.0989e+003
usquave =     2.9794
squave =     1.7261

i =     12
ans =     25
namet =p3hf37
namef =rp3hp37
ubar =    -0.0073
ubarabs =     0.0073
qbar =  9.9278e+003
 What is delta T ?
deltaT =     56
hbar =  177.2813
Q_f =  2.9604e+003
qdivq =     0.2982
H_fl =   52.8648
usquare =     0.0049
usquave =  2.3737e-006
squave =     0.0015

i =     12
ans =     27
namet =p3ht37
namef =rp3hs37
vbar =     7.8049
vdivv =     0.6223
usquare =  6.0989e+003
usquave =     2.9794
squave =     1.7261

i =     14
ans =     29
namet =f2d0321
namef =p2d0321
ubar =    -0.0033
ubarabs =     0.0033
qbar =  4.4622e+003
 What is delta T ?
deltaT =     55
hbar =   81.1305
Q_f =  1.8510e+003
qdivq =     0.4148
H_fl =   33.6542
usquare =     0.0019
usquave =  9.2796e-007
squave =  9.6331e-004

i =     14
ans =     31
namet =t2d0321
namef =s2d0321
vbar =   20.1700
vdivv =     0.2388
usquare =  5.9419e+003
usquave =     2.9027
squave =     1.7037

i =     16
ans =     33
namet =f2d9321
namef =p2d9321
ubar =    -0.0029
ubarabs =     0.0029
qbar =  3.8858e+003
 What is delta T ?
deltaT =     55
hbar =   70.6507
Q_f =  1.5437e+003
```

```
qdivq =     0.3973
H_fl =    28.0669
usquare =     0.0013
usquave =   6.4542e-007
squave =   8.0338e-004

i =     16
ans =     35
namet =t2d9321
namef =s2d9321
vbar =     4.4075
vdivv =     0.1940
usquare =   187.1678
usquave =     0.0914
squave =     0.3024

i =     18
ans =     37
namet =fh6w048
namef =ph6w948
ubar =    -0.0022
ubarabs =     0.0022
qbar =   2.9738e+003
 What is delta T ?
deltaT =     55
hbar =    54.0695
Q_f =   1.4388e+003
qdivq =     0.4838
H_fl =    26.1596
usquare =     0.0011
usquave =   5.6068e-007
squave =   7.4878e-004

i =     18
ans =     39
namet =th6w048
namef =sh6w948
vbar =     5.1477
vdivv =     0.0100
usquare =     0.6732
usquave =   3.2888e-004
squave =     0.0181

i =     20
ans =     41
namet =fh6w48
namef =ph6w048
ubar =    -0.0021
ubarabs =     0.0021
qbar =   2.8107e+003
 What is delta T ?
deltaT =     55
hbar =    51.1035
Q_f =   1.3852e+003
qdivq =     0.4928
H_fl =    25.1852
usquare =     0.0011
usquave =   5.1969e-007
squave =   7.2089e-004

i =     20
ans =     43
namet =th6w48
namef =sh6w048
vbar =    28.1146
vdivv =     0.0094
usquare =    18.0392
usquave =     0.0088
squave =     0.0939

i =     22
ans =     45
namet =fhw048
namef =rphw048
ubar =    -0.0030
ubarabs =     0.0030
qbar =   4.0635e+003
 What is delta T ?
deltaT =     55
hbar =    73.8825
Q_f =   1.5182e+003
qdivq =     0.3736
H_fl =    27.6028
usquare =     0.0013
usquave =   6.2425e-007
squave =   7.9009e-004

i =     22
ans =     47
namet =thw048
namef =rshw048
vbar =    21.5530
vdivv =     0.2405
usquare =   6.8860e+003
usquave =     3.3640
squave =     1.8341

i =     24
ans =     49
namet =fhw948
namef =phw948
ubar =    -0.0023
ubarabs =     0.0023
qbar =   3.1266e+003
 What is delta T ?
deltaT =     55
hbar =    56.8479
Q_f =   1.5031e+003
qdivq =     0.4807
H_fl =    27.3284
usquare =     0.0013
usquave =   6.1190e-007
squave =   7.8224e-004
```

```
i =    24
ans =    51
namet =thw948
namef =shw948
vbar =    4.5357
vdivv =    0.1894
usquare =  189.0447
usquave =    0.0924
squave =    0.3039

Tut =  Columns 1 through 7
     0.1749    0.3064    0.1552    0.3018    0.1440    0.1425    0.1303
Columns 8 through 14
    0.1862    0.2192    0.2386    0.2200    0.2109    0.2200    0.2109
Columns 15 through 21
     0.0844    0.2933    0.0686    0.2809    0.0035    0.3421    0.0033
Columns 22 through 26
    0.3485    0.0850    0.2642    0.0670    0.3399
Tup =
Columns 1 through 7
          0       0.2220          0    0.2379          0    0.1498          0
Columns 8 through 14
          0.1659       0    0.0972          0    0.0925          0    0.1003
Columns 15 through 21
          0    0.1613          0    0.1809          0    0.1853          0
Columns 22 through 26
          0.2114          0    0.1452          0    0.1911
fl diary off
```

Vita

Stacey Elaine Swisher was born in Columbus, Ohio on November 12, 1966. She moved to Cookeville, Tennessee in 1973 when her father began teaching at Tennessee Technological University. After graduating from high school in 1985, she began her undergraduate studies at Tennessee Tech. She received her Bachelor of Science in Mechanical Engineering in August, 1989. Upon graduation, she immediately began an advanced degree at Virginia Tech. In May, 1991 she received her Master of Science in Mechanical Engineering from Virginia Tech. The author will upon completion of this momentous document be working for Kodak, Tennessee Eastman Chemical Company, in Kingsport, Tennessee as a mechanical engineer.